MASTER THESIS
MECHANICAL ENGINEERING

TOWARDS A PARAMETRIC OPTIMIZATION TOOL FOR HYDROFOIL DESIGN

June 8, 2022

S.L. (Sean) Jansen
S1355554

Faculty of Engineering Technology
Department of Production Technology

Examination committee

Dr. Ir. T.C. Bor	ET, Production Technology	Chair
Dr. I. Baran	ET, Production Technology	UT Supervisor
Dr. Ir. J.P. Schilder	ET, Applied Mechanics & Data Analysis	External member UT
F. Garcia Magalhaes	Damen Shipyards, Structures & Production	Supervisor Damen

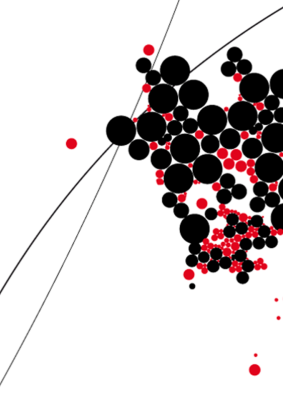

UNIVERSITY OF TWENTE.

DAMEN

Summary

Hydrofoils show potential in improving comfort and efficiency of fast passenger ships. With advances in materials science, fiber reinforced polymer (FRP) structures are considered as a potential new structural material for this specific application, capable of dealing with high loads and corrosive maritime environments. As Damen Shipyards was lacking insight and experience in hydrofoil design, investigation into a proper design procedure from a structural point of view was necessary.

The aim of this project was to provide a clear analytical procedure to come to a structurally safe hydrofoil design, both for traditional isotropic materials as well as for FRP laminates. The knowledge had to be applied in a fast optimization tool to create preliminary structural designs at low cost.
First, the static loads on the structure are identified. The stresses resulting from these loads are evaluated for both isotropic materials as well as for FRPs using Classical Laminate Theory (CLT). Second, using the analytical expressions, a MATLAB based optimization tool is created, iteratively finding a structure with the lowest possible volume. Optimization is done by minimizing the foil volume, to limit the adverse effects of added drag. Failure criteria are use as the constraining factor in the design. Third, the results from the optimization tool are verified using Finite Element (FE) simulation models. Several types of foil profiles, lay-ups and configurations are simulated to gauge the accuracy of the analytical tool. After validation, the tool is applied to the design of a 45 ton monohull and 175 ton catamaran ship in a case study to demonstrate the tool for two very different weight classes.

In validation, the tool performed well for both isotropic and laminated structures. Results were determined to be conservative, with deflections in FE simulations mostly lower than predicted for isotropic and quasi-isotropic designs. On average, FE deflections for these structures exceeded analytical results by 10% at most. Higher error was seen in structures with increased directional reinforcement or large unsupported areas. The error was minimized after inclusion of shear webbing, vastly reducing warping. From validation, the conclusion was drawn that reinforcement in both principal directions as well as for shear was critical for accurate deflection results. Stress results proved difficult to compare, as the error was significantly larger. Inclusion of spars to increase the deflection accuracy lead to stress concentrations, decreasing the stress accuracy and further complicating stress comparison.
Results from the optimization tool proved useful for creating a preliminary design quickly. For the monohull vessel, maximum foil skin thicknesses of 16.2mm (steel) and 25.2mm (Carbon FRP) were found for the front foil. 3D Structure displacement was found to be 9.9% and 8.76% more than the 2D estimation for steel and FRP, respectively. Similar results were found for the rear foils. Internal structures were concluded to be vital to maintain the constant geometrical shape, both at the root of the foils as well as for large unsupported areas. This was seen in the design for the catamaran rear foil, where local deformation was found to be 91.4% above the expected average value while sections without local deformation were 5.7% above the expected average displacement.
Recommended future work based on the conclusions of this project include the further development of a more capable optimization algorithm, further improvements of the numerical model by using realistic pressure distributions and additional validation by means of physical/experimental testing.

Preface

This thesis marks the end of a journey almost a decade in the making. With a three year hiatus and a switch from industrial design to mechanical engineering, it has been quite a ride. The subject of hydrofoils brought together so many of the subjects I encountered over the past years that it was the perfect conclusion to my academic endeavour.
I would like to thank all the support given to me from within Damen Shipyards. In particular, my daily supervisor Frederico Garcia Magalhaes for letting no opportunity go to waste to increase my workload. Countless discussions on the whiteboard about both ships and aircraft served as an inspiration to make the tool significantly better, as well as being a fun distraction from coding.
I want to thank Juri Kuzjatkin for his input and ideas on making the tool a usable development application, the tours and of course the introduction of McWednesdays in the team.
For his support in making sure the thesis lived up to the academic expectations and for his help in sharpening my academic skills, I am grateful to my UT supervisor Dr. Ismet Baran. His feedback ensured I did not get lost in just the commercial and practical side of my research.

Finally, my thanks goes to my parents and friends, who listened patiently as I rambled about making boats fly. A big thanks to anyone else who, in one way or another, supported me during my studies and thesis.

Sean Jansen
Zeist, June 2022

1954 - 2022†

Nomenclature

Abbreviations

AR	Aspect Ratio
BV	Bureau Veritas
CFD	Computational Fluid Dynamics
CLT	Classical Laminate Theory
(C)FRP	(Carbon) Fiber Reinforced Polymer
FE	Finite Elements
FEA	Finite Elements Analysis
FEM	Finite Elements Method
GA	Genetic Algorithm
HSC	High Speed Craft
LE	Leading Edge
ML	Machine Learning
NACA	National Advisory Committee for Aeronautics
PSO	Particle Swarm Optimization
SF	Safety Factor
TE	Trailing Edge
TO	Topology Optimization
TR	Taper Ratio

Symbols

A_{min}	Minimum foil planform area
W	Displacement in [kg]
P_{cav}	Cavitation pressure limit
k_{TO}	Take-off performance factor
λ	Taper ratio
c_r	Foil root chord
c_t	Foil tip chord
b	Span of foil
A	Area
D_i	Lift-induced Drag
$C_{D,i}$	Induced drag coefficient
C_L	Lift Coefficient
C_M	Moment Coefficient
q_∞	Dynamic pressure
c	Chord length
I	Area moment of Inertia
σ	Stress
τ_V	Shear stress due to internal shear force
τ_T	Torsional shear stress
V	maximum internal shear force

y	Distance to neutral line of beam
M_T	Pitching moment torque
t_{min}	minimum wall thickness
ϕ	geometrical angle of twist
G	Shear modulus
I_T	St. Venant torsion constant
$\sigma_{1,2}$	Principal stresses
δ	Deflection
θ	Slope
E	Youngs Modulus
σ_{crit}	Critical buckling stress
P_{crit}	Critical buckling load
k	Effective length factor
L	Length
σ_{yield}	Yield strength material
λ_c	Column slenderness ratio
e	Distance of eccentric load to neutral line column
c	Distance edge of column to neutral line
β	Tabulated plate deformation constant
α_p	Tabulated plate deformation constant
q	Uniform pressure load
$[R]$	Reuter Matrix
$[T]$	Transformation Matrix
$[C]$	Stiffness matrix
$\{\epsilon\}$	Laminate strain vector in material coordinates
$\{\sigma\}$	Laminate stress vector in material coordinates
$\{\epsilon^*\}$	Laminate strain vector in layer coordinates
$\{\sigma^*\}$	Laminate stress vector in layer coordinates
κ	Laminate curvature
$\widehat{EI}_{yy/zz}$	Composite replacement bending stiffness
$\widehat{EA}$	Composite replacement tensile stiffness
$\widehat{GI_T}$	Composite replacement torsional stiffness
α	Local slope of curved composite plate
η	Coordinate along curve of composite plate
E_x	Equivalent laminate modulus
$N_{x,y,xy}$	Extensional/shear loads on laminate
$M_{x,y,xy}$	Moments on laminate
$S_{T/C}$	Tensile/Compressive strength ply
V_f	Volume foil
t_f	Foil profile thickness

Contents

1 Introduction

1.1 Damen Shipyards

Damen Shipyards is a large shipbuilding conglomerate based in the Netherlands, with shipyards all over the world. While they have a wide range of ships in their portfolio, ranging from naval vessels to luxury superyachts, Damen is always looking to improve the performance and capabilities of their vessels. Recently, hydrofoils have received renewed attention in the shipbuilding world. The hydrofoil technology, where a lifting element is mounted under the hull to either support it or lift it completely out of the water (Figure 1.1a), is used to reduce drag for high speed craft, increasing top speed and efficiency. Besides that, passenger comfort at high speeds is improved as the hull does not slam into the waves but rather rides above them. These clear advantages have peaked the interest of Damen to explore the possibilities of adding hydrofoiling ships to their portfolio.

(a) Boeing 929 Jetfoil, a hydrofoil ferry from 1976 [1]

(b) Damen FCS-7011, a high speed crew transfer vessel [2]

Figure 1.1: High speed craft

1.2 Problem statement

Within the Damen Workboat division, a class of high speed craft (HSC) is included. For these vessels, Damen is always looking to improve performance while retaining excellent seakeeping characteristics. An example of a HSC crew transfer vessel, used to transport crews to offshore rigs, is given in Figure 1.1b. Simultaneously, comfort is of high importance for these high speed vessels, as they are often used to transport crews that need to arrive at their destination rested and ready to work. The main drawbacks of sailing at high speeds are high fuel costs and that at rougher seastates, the comfort is greatly diminished due to the slamming of the ship on the waves.
In the past decade, there has been a revival of interest in hydrofoil technology [3]. Hydrofoils can reduce hull drag and fuel costs, increase operation speed and increase comfort [4] by adding lifting surfaces to the underside of the hull. The technology itself is not new, with hydrofoil ferries in operation today in mostly south-east Asia. However, existing solutions date back from to 1970s and are quite inefficient by today's standard. Material science has progressed significantly in the meantime and advanced Fiber Reinforced Polymer (FRP) materials allow for new lightweight designs. This can be seen in modern hydrofoil applications, such as the AC75 foiling yacht [5] first launched in 2012, where the entire foil and swing arm is made of Carbon FRP.

Existing hydrofoils have been created exclusively using metal. With high weight, low specific strength and poor corrosion resistance, metal hydrofoils have proven to be inefficient and costly due to intensive maintenance requirements. This is partially the cause for hydrofoils not being economically viable for all but a few applications. FRPs are identified as a potential suitable alternative to metal, as they are a highly corrosion-resistant and low-density group of materials that can be optimized for specific load cases. A framework to compare the performance of the two material groups directly under the same conditions is lacking, requiring minimization of the structural dimensions for both materials as a first step towards optimization.
Additionally, Damen Shipyards has never fully developed any hydrofoil ship and lacks a clear procedure needed to design a hydrofoil system for any ship in their portfolio. Directly designing and optimizing using Finite Element Method (FEM) is computationally very intensive and slow. A gap is identified in the capabilities and knowledge at Damen Shipyards which could potentially be closed by a fast, analytical and parametric design tool allowing for exploratory designs.

1.3 Research goals

In order to come to a comprehensive design procedure and a feasible hydrofoil concept, a main research question is presented:

'How can an optimization design tool be used to guide the development of a Fiber Reinforced Polymer hydrofoil?'

To find an answer to this question, three subquestions are formulated to guide the research.

1. How can a fast preliminary hydrofoil design tool based on analytical expressions be developed?
   (a) What is the current state of the art for hydrofoils?
   (b) What are the main loads on a hydrofoil?
   (c) How can the loads be translated to stresses in a laminate structure?
2. Can the analytical results from the optimization tool be verified?
3. Can the applicability of the tool be demonstrated in a case study?

1.3.1 Challenges

For the design and optimization of an advanced FRP hydrofoil, there are several challenges. Despite the fact that the use of hydrofoils is by no means new or innovative, the application of advanced FRP materials to create a hydrofoil for a (relatively) high displacement vessel is new. So far, composite hydrofoils are only applied to fairly low displacement vessels, ranging from surfboards to small scale electric ferries [6]. Inherently, this step towards higher displacements leads to some challenges for the research project.

Material and structural strength

Traditionally, FRPs perform well in weight-saving applications. Often, the material thickness can be kept low while still retaining high strength or stiffness. For low thickness structures (plates) through-thickness effects are considered to be negligible. For the application to hydrofoils capable of carrying up to several hundred tons of weight, the thickness of the composite laminates may become high enough that the through-thickness effects can no longer be ignored. This will have significant implications for both the accuracy of the initial analytical design as well as any Finite

Element (FE) simulations done after. The increased thickness necessitates a thorough analysis using FE to determine the through-thickness stresses, to be able to predict certain failure modes such as delamination. At the same time, the current limitations on modelling thick composites using FE should be acknowledged [7]. Where possible, verification of analytical and numerical results by means of physical testing is preferred. Both in-depth FE and physical testing is beyond the scope of the research.
Furthermore, increased thickness will lead to possible difficulties in composite production and adverse effects on the structural strength of parts. Some production methods may not be viable for very thick laminates. The end-user of the design tool should keep the production limitations in mind, possibly implementing hard limits dictated by production capabilities, when using the tool.

Hydro-structural interaction

Composite materials are quite flexible when compared to steel components. As such, deflections may be greater than in metal counterparts. Deflections may change the hydrodynamic properties of the foil (variations in lift and drag under different loading situations). Elasticity of the structure is not necessarily a negative property, as a changing geometry may lead to improved hydrodynamic performance.

Optimization

Hydrofoil design is a complex back-and-forth between structural design, hydrodynamic performance, weight, production and costs. Often an iterative process, it is beneficial to have a clear understanding of each step in the process. To reduce the time for each iterative step, the structural design procedure can be optimized. It is quite important to consider what parameters should be adjusted iteratively to come to the 'best' design, but true optimization is beyond the scope of this thesis. As other industries have similar geometries that need to be optimized, inspiration can be taken by considering the state of the art for similar applications.

1.4 Outline

This thesis is structured in four main sections, schematically shown in Figure 1.2 with the corresponding chapters. A literature study is carried out to create a basic understanding of hydrofoil technology as well as insight into the state of the art of optimization for FRP foil structures. An analytical framework is created and applied in an iterative optimization tool using MATLAB 2019b. FE simulations are used to validate the results. This is done by comparison of deflection and stress values predicted by the tool and results from FE. The tool is applied to in a case study to qualitatively assess the performance of the 2D-based tool in designing a 3D-structure. Finally, the results of the validation and case study are discussed. The final section of this report consists of conclusions and recommendations for future improvements.

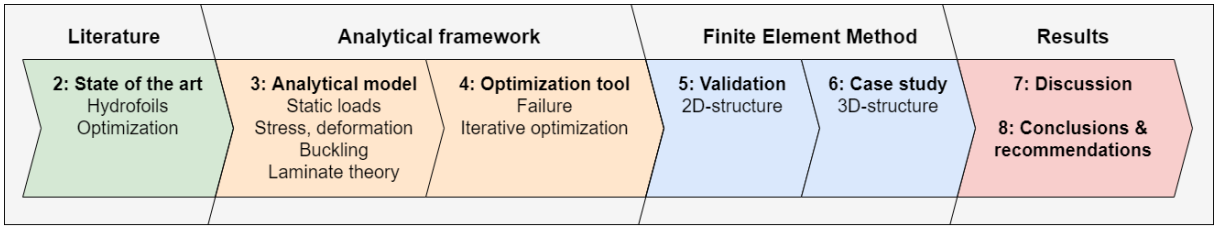

Figure 1.2: Outline of thesis.

2 | State of the art

The history and state of the art for hydrofoil technology are discussed in this chapter, highlighting the different types and their respective (dis)advantages. As the properties of FRP can be optimized for their specific use case, different optimization routines used in industry are presented.

2.1 Historical background

Hydrofoils have been added to ships for quite some time. The earliest experiments of adding foils to boats was already in 1861 [8] when Thomas Moy used a boat to more efficiently test the performance of airfoils in a time before wind tunnels.
Through the early 20^{th} century, several experimental hydrofoiling craft were designed and built, leading to new insights in more efficient application of the principle. While the first hydrofoils were fully submerged, the surface-piercing type (section 2.2.1) were introduced in 1907. With this new type of foils, the HD-4 was developed in the United States. This particular craft took the world speed record on water with 70.86 mph in 1919 and held it down for 10 years, showing the potential for high speed craft.
From 1927 onward, several commercial applications were devised, creating fast passenger craft. However, due to the Second World War, most designs were aimed at creating high speed naval vessels. This brought forward a leap in the capability of the ships, with 80 ton vessels with 20 ton cargo capability being built for the German navy.

(a) PT-10 Supramar, early hydrofoil ferry, 1953 [8]

(b) FoilCat 35M, foiling catamaran ferry, 1995, in operation today [9]

Figure 2.1: Historical and modern hydrofoil ferries

With the technology slowly maturing after the war, several hundred fast hydrofoil ferries have been built in the former Soviet Union. With their higher speed, comfort and fuel efficiency, hydrofoil boats had become very popular during the second half of the 20^{th} century (Figure 2.1a). However, in more recent years, the hydrofoil boat has fallen out of favor due to higher maintenance cost and limited routes that make sense economically [10, 11]. Today, only a handful of routes still employ hydrofoil ferries, mostly located in Southeast Asia, operating on open sea between Hong Kong and Macau (Figure 2.1b).

2.2 Hydrofoil configurations

Different configurations for hydrofoils exist. As their structure and applications differ, several types are discussed below.

2.2.1 Foil types

Generally speaking, there are two main types of hydrofoils: surface piercing and fully submerged foils (Figures 2.2a and 2.2b, respectively).
As the name implies, fully submerged hydrofoils are completely below the water surface during operation, including during the foilborne operation. The lifting surfaces of surface-piercing foils are always partly out of the water, which means that the total lifting area changes with the speed (and thus the wetted area) of the ship. In general, surface-piercing foils are used on vessels with a water displacement (measure for ship weight) up to 150 tons, while submerged foils can be used on higher displacement ships, with some ships exceeding 300 ton displacements [12]. Both these systems have several advantages and disadvantages.

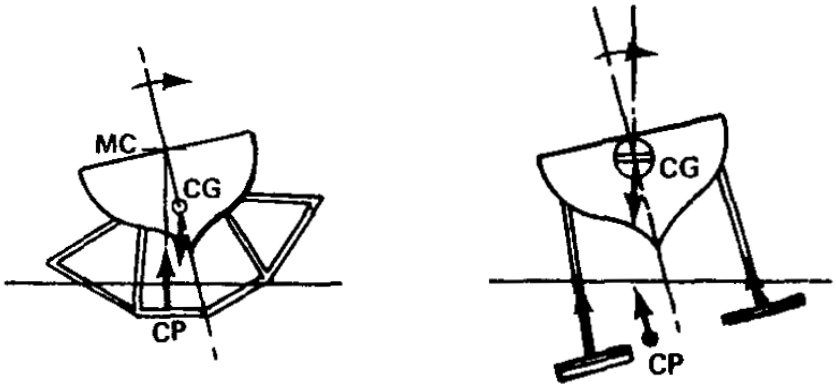

(a) Schematic of surface piercing hydrofoil (b) Schematic of a fully submerged hydrofoil

Figure 2.2: Schematic of two main foil types [13]

Fully submerged foils

Having completely submerged hydrofoils brings along some significant advantages. Although both surface-piercing and fully submerged foils are renowned for their seakeeping abilities even in significant waves [14], fully submerged foils are generally more comfortable for passengers. As long as the foil stays at least one chord length [10] below that water surface, the lift is constant and waves have no effect on the foils. Contrary to surface-piercing foils, the ships are less hindered by waves; given that the wave height is less than the ride height, fully submerged foil ships can ride just above the waves without slowing down. This makes it a relatively level platform, which significantly improves passenger comfort (Figure 2.3a).

As the system is inherently unstable (lift remains constant even when entering a rolling turn due to disturbances, no self-correcting motions will set in), it will always need a form of active control. Usually, control of the foils is achieved by using flaps or fully moving foils. While it complicates foil construction and increases maintenance costs, it also allows the ship to be controlled in a similar manner as an aircraft.

While foilborne, it is possible to roll during a turn. This bank angle (or heel angle) allows for a coordinated turn. Not only does this decrease the necessary turn radius, it also prevents objects in the vessel to shift due to centrifugal forces felt in a flat turn. This means turns can also be taken at a higher speed during foilborne operation.

These advantages come at a cost as there are some significant disadvantages associated with fully submerged hydrofoils.
Dependent on the application of the vessel, the depth of the hydrofoil system may lead to difficulties. As mentioned earlier, for constant lift a minimum depth greater than the length of the chord of the foil has to be maintained.
The larger a vessel, the higher the displacement. Higher displacement leads to higher lift necessary to reach foilborne operation. Higher lift can be achieved by either sailing faster or by increasing the size of the hydrofoil. This means that when ships become larger, not only do the struts need to be longer to accomodate the deeper hull, they also increase in length due to the increased chord length of the hydrofoils. This has two implications: firstly, this leads to a practical limit for the maximum displacement vessel that can practically use hydrofoils. As the foils become larger, at some point they will exceed the beamwidth of the ship, making routine operations such as docking difficult. Secondly, the size and depth of the foils limits the usability to deeper waters. This can be circumvented by designing retractable hydrofoils, but this very much increases the complexity of the design and the cost of maintenance. As such, fully submerged foils for high displacements vessels are realistically only viable for deep water operations.

Surface-piercing foils

Surface-piercing foils are hydrofoils where a portion of the lifting surface is always out of the water. They are often arranged in a 'V'-setup. As the craft accelerates and starts to rise out of the water, a smaller part of the foil will be in the water, reducing the total lifting capacity. As a result, the ride height automatically balances itself based on the speed of the ship.
Piercing foils have some unique characteristics that make them the preferred choice in certain situations.

One of the most advantageous aspects of surface-piercing foils is the fact that they are inherently stable. Not only do they maintain a stable distance to the water surface, they also tend to be self-rightening.
Rocking and listing of the vessel due to disturbances is automatically corrected. With one half of the hydrofoil being pushed down in to the water while the other half is lifted more out of the water, there will be an asymmetric lift distribution over the hydrofoil. As lift on the lower side increases, it will return the ship to the upright equilibrium position where the lift is symmetric again.
The stable configuration does not require the complex active control necessary for the submerged hydrofoils. This greatly simplifies the construction and lowers the maintenance costs associated with the control surfaces on submerged foils.
However, this simplicity comes at a cost. Relatively, the surface piercing foils are larger, as a significant part is outside the water. This means that often the hydrofoils are wider than the beamwidth of the ship itself, complicating docking as the ship cannot approach the dock closely.
Stability and high maneuverability are mutually exclusive. The high stability inherently means piercing foils are less maneuverable than the submerged, unstable foil configuration.

Despite being (laterally) stable, seakeeping characteristics of surface piercing foils are significantly worse than of submerged foils. As the distance to the water surface is always more or less the same, the piercing vessels tend to contour the waves (Figure 2.3b), following the heaving motions of the waves. Compared to the platforming motion of submerged foils, this leads to lower passenger comfort at rough sea states, with more pitching motion. Due to this fact, hull slamming in rough sea states

occurs more often than with submerged foils.

(a) Platforming, a level ride above the waves (b) Contouring motion, following the shape of the wave

Figure 2.3: Difference between platforming and contouring [10]

The fact that the foils pierce the surface bring an additional drawback on the efficiency of the foils. A phenomenon called *ventilation* occurs at the interface of water and air. The lifting device sucks air down along the surface, greatly diminishing the lift of the foil. As the density of water is about 800 times higher than that of air, the velocity of the air would need to be many times higher in order to keep generating the same amount of lift. If ventilation occurs on a significant portion of the hydrofoil, it will not be able to provide the lift necessary to maintain foilborne operation and it will crash down on the water.
Since the submerged foils have no interface with air, ventilation does not occur there (with the exception of ventilation creeping down a strut during uncoordinated turns).

General disadvantages of hydrofoils

Regardless of the configuration of the foils, some disadvantages are always present.
A major limitation on the maximum speed of the vessel is imposed by the addition of hydrofoils. In general, the reduction of drag through minimization of water displacement leads to substantial increases in top speed for large vessels. However, at speeds over 50 knots, cavitation starts to occur over the low pressure side of the hydrofoil [10]. In high speed fluids, cavitation occurs as the static pressure in the flow drops below the liquid vapour pressure. As a result, vapor pockets or cavities form in the fluid. As soon as the surrounding pressure is higher, these cavities compress and implode, causing shockwaves.
The shockwaves caused by cavitation cause damage to the surface of the foils, which can lead to structural failure (cyclic loads, vibration and fatigue) as well as deterioration of lifting performance as the surface becomes rough from cavitation pitting.
The detrimental effects of cavitation on the foil can be circumvented by using supercavitating foils. By creating a cloud of cavities around the foil, cavities will not form on the surface itself. However, the lifting performance of supercavitating foils is notoriously poor when compared to subcavitating foils, requiring significantly more power. Effectively, this puts an upper limit of about 50 knots on the efficient maximum speed for a hydrofoiling vessel [13].

2.2.2 Foil configuration

When designing a hydrofoil ship, the lay-out of the foils is an important consideration. The number of foils added to the hull as well as their location determine the individual loading of the struts, but also the vehicle dynamics and comfort of the passengers. Through the years, several standard lay-outs have emerged, shown in Figure 2.4. Only configurations capable of fully lifting a vessel are considered (no monofoils or assisting foils).

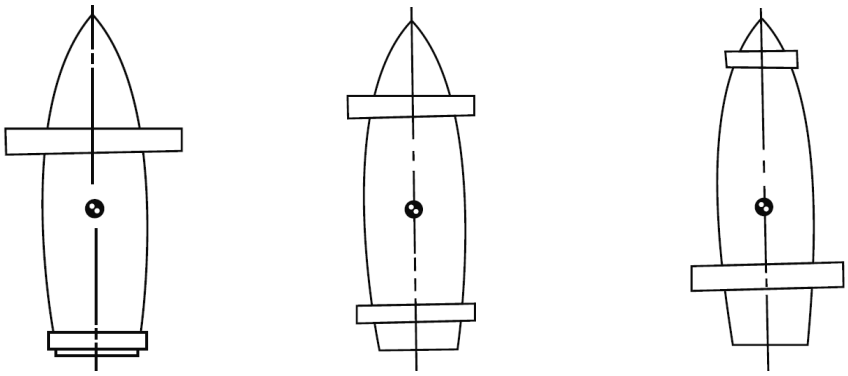

(a) Schematic of a conventional configuration

(b) Schematic of a tandem configuration

(c) Schematic of a canard configuration

Figure 2.4: Schematic of three basic configurations [8]

Conventional

Also known as the aircraft configuration, the conventional lay-out has a large connected hydrofoil in front of the centre of gravity of the ship, and a smaller foil towards the stern. The weight distribution is at least 65% on the forward hydrofoil.

Canard

The canard configuration is the opposite of the conventional lay-out. With at least 65% of the weight resting on the rear hydrofoil, it is the preferred lay-out to increase passenger comfort, as waves have less effect on the stern foil in this configuration, where passengers are mostly located [8, 10].

Tandem

The tandem configuration puts the center of gravity of the ship at equal distance to front and rear hydrofoils, making each carry half the weight of the ship.

Split

The load carrying hydrofoils and struts themselves can also be created in many different shapes. Most often, the larger foil is a single, connected U-shape (two struts and a foil in between, Figure 2.5b). However, it can also be that the main foil is separated into two parts (Figure 2.5a). This is sometimes done to allow for independent lowering of the foils into the water.

(a) Split front hydrofoils: two separate foils (retracted) [15]

(b) Non-split rear U-foil [16]

Figure 2.5: Split and non-split foils

2.2.3 Hydrofoil materials

Most hydrofoils from the "golden age" of fast ferries (mid 20^{th} century) are made of steel [17]. Inexpensive, readily available and relatively easy to work with, steel is a versatile material for shipbuilding. Paired with the fact that most hulls at the time where built out of steel, it was the logical material of choice for hydrofoil design. It was only in the 1950s that fibre reinforced plastic technology was introduced for maritime applications, originally mainly for hull construction using glass fiber [18]. FRP technology was still in its infancy, with the first 100 ton FRP hull ship being built in 1964, when steel hydrofoil ships were already exceeding 200 ton displacements (Bras D'Or, [8]).

With advancements in materials and production processes, advanced composites have recently been implemented in hydrofoil design, albeit at a much smaller scale vessel than the hydrofoil ferries operating today (Figure 2.6).

For FPR structures, a 1500mm long hydrofoil with a maximum local thickness of 100mm is among the largest experimental foils available [7], not yet close to the size of existing steel hydrofoils for fast ferries. FRP foils for high loading conditions can likely be compared better with the blades of a wind turbine, for both thickness and production processes to create them.

Figure 2.6: Carbon fiber composite swing-arm and hydrofoil on an AC75 racing yacht, 7.6 ton displacement [19]

2.3 Optimization of FRP foil structures

Although FRPs are not generally applied to hydrofoils yet at an industrial scale, inspiration for the design of wing profiles using FRP can be found in other industries. Similar transitions from metal to FRP structures have taken place both in aerospace and sustainable wind energy industries. For both, the core principle is the generation of lift by means of an aerodynamic profile. Extensive research has been done on the optimization of the fiber reinforcement directions in the laminates to deal with the lift and drag loads. This ection deals with some of the

Foil shape optimization using numerical simulations

With advances in computational power, simulation software can be more effectively used in optimization problems. One example is the iterative optimization of hydrofoil shapes for lowest drag using Computational Fluid Dynamics (CFD). The drawback is that this is very computationally intensive and therefore relatively slow [20]. Beyond that, it is difficult to optimize for both optimal hydrodynamic performance and structural strength at the same time using one package.

Heuristic optimization methods

Heuristic optimizations is a means to more quickly find the (near) optimum solution, when not all aspects of an optimization problem are known. One method that has been used to optimize a laminate stacking sequence is Genetic Algorithm (GA) optimization. By fixing certain variables such as the individual ply thickness and only considering a discrete set of ply angles, fairly quickly (near) optimum designs can be found [21, 22]. This method is based on combining the properties of only the best performing solutions to iteratively create the next set of potential solutions [23] (only the strongest "genes" survive each optimization step). This method can be applied for optimization of multiple variables, minimizing for instance both deflection and weight at the same time. The method has been applied to find the optimal hydrofoil shape [23] for the best hydrodynamic performance, but not in combination with FRP structural optimization. GA optimization does not necessarily lead to an exact solution and can still be computationally intensive to carry out. In some cases, the data needed to feed the GA needs to come from 3D-models created for simulation purposes [24]. This means that additional software and knowledge is needed to carry out the optimization.
Hybrid solutions are also possible, where Particle Swarm Optimization (PSO) routines are combined with FE. This combination utilizes the strength of both approaches by applying a PSO algorithm to a parametric FE model to speed up the analysis [25].

Topology Optimization and Machine Learning

A practice already widely used in commercial engineering applications is Topology Optimization (TO). With this method, there is no need for an initial design. TO is capable of iteratively finding a structurally optimum design, based on mathematical algorithms that consider every point within the design space as a variable, assigning a density value of 1 or 0 to the point. Starting out with uniform density, it will adjust and re-evaluate whether or not the structural performance requirement is met [26]. By removing the elements in a FE mesh that contribute little to nothing to the performance, the structure is reduced organically. A major drawback to this is the very high computational cost caused by repeated FE calculations. The resulting structures may also difficult or even impossible to produce, as solutions often include complex ("organic") internal 3D-structures [27].
With the advancement in computational power and machine-learning (ML) knowledge over the past years, deep-learning networks have recently been investigated as a possible addition to TO, reducing the drawbacks of the computational costs [28]. ML may improve the efficiency of TO tremendously, but these networks require large datasets to be trained in the correct way. Deep-learning networks can also be trained to include the stacking sequence of a laminate as an optimization variable.

3 Analytical model

3.1 Introduction

The static loads on the hydrofoil and the struts are identified so that they can be used to determine the (maximum) stresses that occur in the structure. A distinction is made between isotropic and orthotropic materials to accurately compare their performance. Classical Laminate Theory (CLT) is applied to model the composite plates and the Tsai-Hill failure criterion is used to determine whether the local ply stresses exceed the material limit, for which safety factors based on Fiber Reinforced Polymer (FRP) ship appendage guidelines are calculated.

3.2 Design procedure overview

The analytical design and optimization of a hydrofoil is an iterative process. A global overview of the structural design procedure is given, which starts at the design requirements and specifications of a vessel and ends with a foil geometry that can handle the stresses for the identified static loading conditions (Figure A.1 found in appendix A.1). A simplified chart is found in Figure 3.1. The first step is to define the dimensions of the structure based on the vessel properties. For the application intended by Damen Shipyards, only fully submerged hydrofoils are considered. The higher level of comfort on rougher seas is a clear advantage over surface-piercing foils.

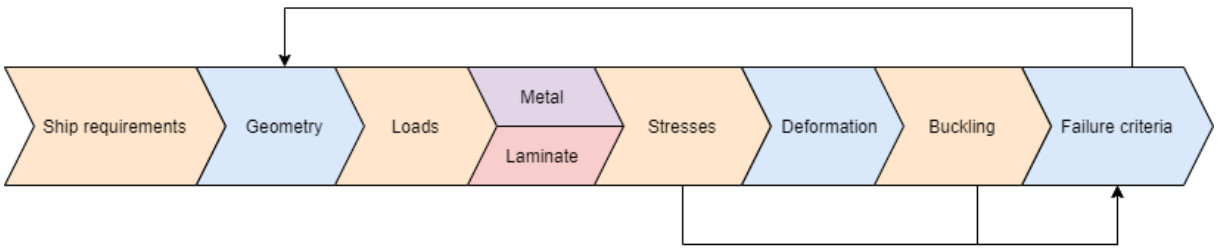

Figure 3.1: Simplified structure of analytical model

3.3 Hydrodynamic loads

The first step in the design of the hydrofoil analytically is the determination of the static loads on the structure.

3.3.1 Estimation of planform area using hydrodynamic loads

The main function of the foils is to generate lift. This lift is the main load acting on the structure, causing several stresses. The hydrofoils should be able to provide enough lift to allow the ship to rise out of the water. If the lift is larger than the weight of the ship, it will start to take off out of the water. It doesn't have to be able to take off violently or quickly, a lift load that is slightly larger (for instance, by 10%) than the displacement is considered sufficient as an initial estimate. The lift is multiplied by the take-off factor, k_{TO}.
This minimum lifting load is the critical starting point for determining the geometry of the foil. The

hydrofoil has an upper limit on the amount of lift that can be generated. A value of 85000 $\frac{N}{m^2}$ is used by Damen Shipyards as the cavitation pressure limit in ship propeller design and this value will be applied in the analytical tool as well. The (local) pressure from the lift can not exceed this value, as cavitation can lead to loss of lift as well as possible damage to the surface. The cavitation limit will be denoted by P_{cav}.
The minimum necessary area is then given by:

$$A_{min} = \frac{k_{TO}W}{P_{cav}} = \frac{k_{TO}W}{85000} \tag{3.1}$$

The geometric properties that can together create this minimum area are the chord length, the span, the taper ratio and the aspect ratio. The geometric properties of a foil are schematically shown in Figure 3.2. Taper ratio λ is the ratio between the chord at the root, c_r, and the chord at the tip, c_t.

$$\lambda = \frac{c_t}{c_r} \tag{3.2}$$

The aspect ratio describes the slenderness of a wing and is defined as [29]:

$$AR = \frac{b^2}{A} \tag{3.3}$$

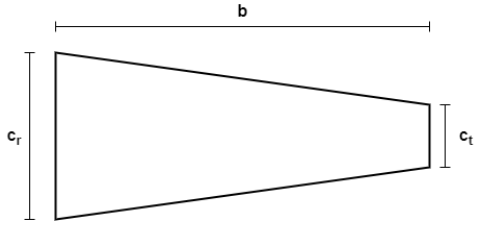

Figure 3.2: Foil geometric properties

The aspect ratio can be plotted as a straight line as it is a linear relation between chord and span. This means it will have one intersection with the curve defined by the combination of chord and span for a given taper ratio. This intersection gives the values that define the hydrofoil shape. An example of this is given in Figure 3.3, where the curved lines represent the combination of span and chord that together give the minimum area, for ten taper ratios. Choosing the correct aspect ratio is an optimization problem that balances between the hydrodynamic performance (higher aspect ratios lead to lower induced drag), and the structural stress (long, slender foils have a higher root bending moment and resulting stress). The aspect ratio is a part of the induced drag D_i of a finite wing as follows, demonstrating its importance [29]:

$$D_i = q_\infty C_{D,i} A \tag{3.4}$$

$$C_{D,i} = \frac{C_L^2}{\pi AR} \tag{3.5}$$

Where q_∞ is the dynamic pressure (consisting of $\frac{1}{2}\rho v^2$) and $C_{D,i}$ and C_L are the respective induced drag and lift coeffecients of a finite wing.
Within the scope of this assignment, the aspect ratio is chosen without optimization, but it can be adjusted as it is an input variable for the design tool. An example of a graph showing the selection of span, chord and taper ratio combinations is shown in Figure 3.3. The intersection point is the

smallest possible combination for span and chord that meets the requirements of the minimum area for the defined taper ratio.

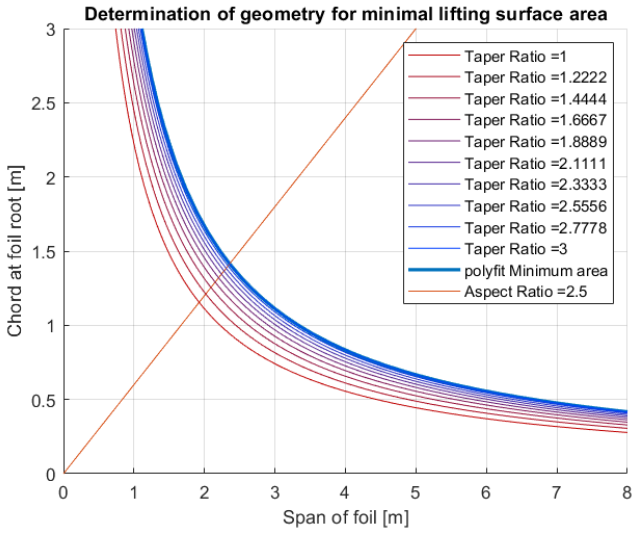

Figure 3.3: Determining geometry - combinations of span, chord and (inverse of) taper ratio to yield minimum area

For the analytical estimation of the load on the structure, the hydrofoil is assumed to be a 2D infinite wing. This means that there are no edge-effects such as vortices that have an influence on the lift distribution along the span of the foil [29]. For the analytical analysis, this approximated distribution is deemed sufficient, but the calculations can also be performed using pressure data found using computational fluid dynamics.
The lift generated by a foil depends on several variables: the width of the foil (the chord, c), the dynamic pressure of the fluid (q_∞) and the non-dimensional lift coefficient (C_L), which accounts for the angle at which the foil is positioned in the free stream fluid. The total lift of a foil section is then given by:

$$L = q_\infty C_L c \tag{3.6}$$

The lift generated by an entire wing is found by integration of the section lift along the span of the wing, resulting in the lift on the entire wing surface (A).

$$L_{wing} = q_\infty C_L A \tag{3.7}$$

Similarly, as the foils generate lift, they also experience drag. This drag is given by:

$$D = q_\infty C_D c \tag{3.8}$$

When considering a finite wing, the drag coefficient C_D is a combination of the profile coefficient c_d and the induced drag coefficient $C_{D,i}$ as given by equation 3.5. As the main focus of this work is on structural strength, an in-depth analysis of hydrodynamic performance is left out. The total drag is estimated by integrating the cross-sectional drag over the length of the foil, not taking into account the induced drag components present in finite wing analysis. This estimate is deemed useful enough since, as discussed later, the drag is not the critical load for the structural integrity.
The center of lift does not necessarily coincide with the hydrodynamic center. This means that the lift has an arm around this hydrodynamic center, leading to a pitching moment. The total pitching moment is given by:

$$M = q_\infty C_M c \tag{3.9}$$

As changing the geometrical properties of the hydrofoil for structural reasons will also influence the hydrodynamic performance (and thus the loads themselves), a proper estimation of the lift is important. As such, *XFOIL 6.99* [30] is used to get realistic coefficients for determination of the loads.

3.3.2 Geometric properties

The minimum area is distributed over the different foils by using the weight distribution factors between the front and rear. While the Bureau Veritas (BV) criteria for stability of surface piercing hydrofoils [31] only put requirements on the lateral stability of a vessel, the longitudinal distribution influences the seakeeping characteristics (and comfort) of the ship. As such, it is an important design parameter to be considered.

An overview of the steps necessary to reach the hydrofoil dimensions are given in the following schematic:

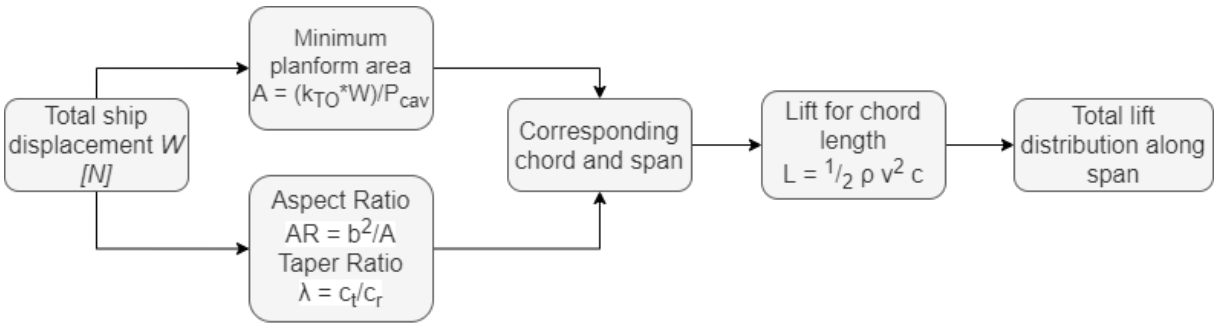

Figure 3.4: Determining geometry - schematic overview

3.4 Hydrofoil loads - Static analysis

This section presents the analytical expressions relevant for the stresses and deformations in the hydrofoil. First, a global overview of the foil loads is displayed in Figure 3.5.

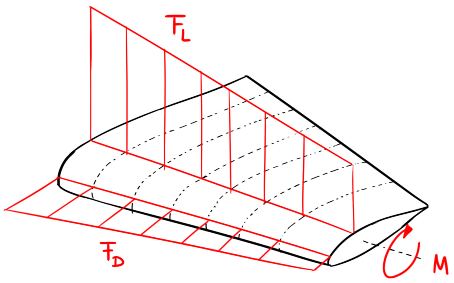

Figure 3.5: Drag, lift and resulting torsion on hydrofoil

3.4.1 Bending loads

Bending loads on the foil are the main loads on the hydrofoil, caused by both lift and drag. The relevant assumptions and expressions are presented in this section.

Bending caused by lift

The main function of the hydrofoil is generating enough lift to push the entire hull out of the water. The lift load will lead to several stresses, caused by bending, shear and torsion. The geometry of the foil changes due to the loads, causing deflection and twist.

Two distinct configurations are considered: a single strut and a double strut foil. The third configuration that might occur is the foil with three struts. This is simplified to the double strut situation but with half the foil length.
The hydrofoil supported by a single strut is approximated by a cantilever beam under a (non-uniform) distributed load. A foil supported by two struts is modelled as fixed-fixed beam under a (non-uniform) distributed load.
While in literature the cross-section of a foil is often approximated by a hollow rectangle [32] with a correction factor, a more accurate representation is given by dividing the arbitrary shape into small rectangles approximating the actual foil shape, Figure 3.6 (visualization, calculations are done on rectangular elements). For each element, the second moment of area can be easily calculated using the parallel axis theorem [33]. Summing the values for each small section gives the total moment of inertia of the foil cross-section. This procedure is done for several points along the span of the foil (in case of a tapered foil) to accurately model the local stresses and displacements.

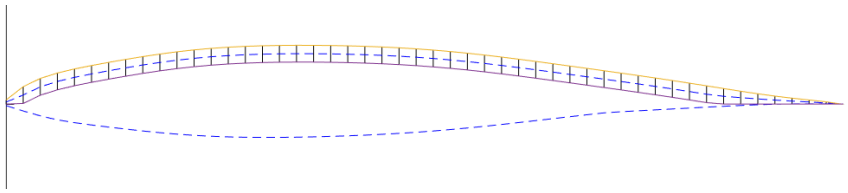

Figure 3.6: Dividing foil cross-section into equal squares to calculate inertia around neutral line

Calculation of the moment of inertia for a rectangular element at a parallel axis is done with [33]:

$$I = I_{CM} + Ad^2 = \frac{BH^3}{12} + BHd^2 \tag{3.10}$$

where d is the distance of the blue dashed line to the neutral line (geometrical middle) of the foil.
The method gives a result fairly close to the method of using a correction factor [32]. Although a bit more involved, using the foil cross-section allows for closer comparison between isotropic and laminate foils (section 3.9.4).
Using the found inertia, the maximum bending moment and axial bending stress can be found for each section.

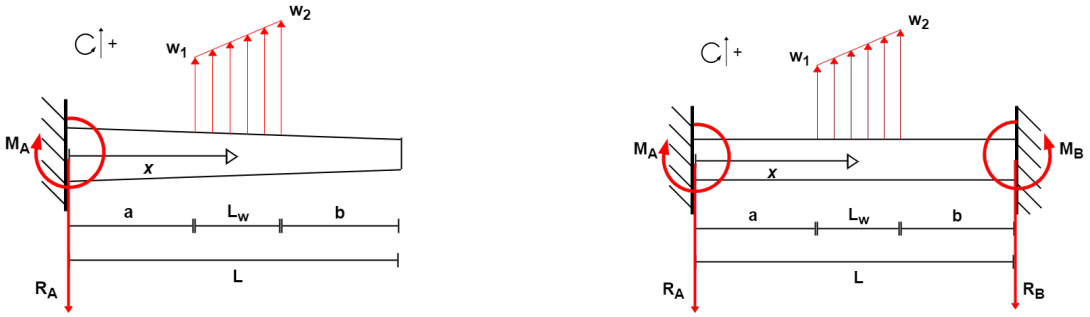

(a) Tapered cantilever with trapezoidal partial distributed load

(b) Clamped beam with trapezoidal partial distributed load

Figure 3.7: Simplification for analytical expressions

A cantilever beam is considered with a random pressure distribution (Figure 3.7a, shows a part of a distribution), which can be obtained from a CFD analysis of a foil or from basic hydrodynamic calculations based on foil theory as discussed in section 3.3.1. A number of points along the span is evaluated (coincident with the points for which the moment of inertia is calculated). The local pressure distribution is approximated by a trapezoidal distribution between two adjacent points. This is done between all points, which allows calculation of the bending moment, shear load, slope and deflection for each section. The total bending- and shear diagram can be obtained by summing the individual contributions of each local load, or by integrating the total pressure distribution to find the moment.
The analytical expressions for the bending moment, shear load, end slope and deflection are given in appendix A.2.1. The expressions given there are applicable to prismatic beams, which covers the struts and the U-foil clamped beam. The foils with a single strut are more complex, as they are non-prismatic if a tapered foil is chosen. A tapered beam can be simplified to a beam consisting of several shorter beams with varying cross-sections, shown in Figure 3.8. The method of superposition is used to determine the deflection and slope of the total beam [33].

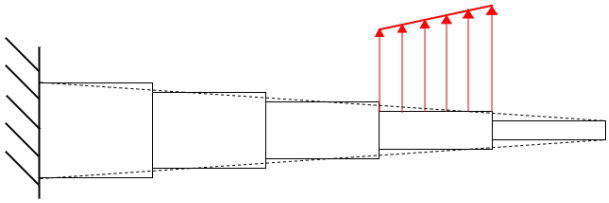

Figure 3.8: Simplification of tapered beam to beam consisting of multiple prismatic sections

An additional remark on the analytical expressions of the U-foil needs to be made. Simplifying it as a clamped beam (as seen in Figure 3.7b) assumes that the struts are infinitely stiff, unable to deflect or twist at the end where the U-foil is connected. This will lead to the highest moments in the U-foil occurring at the clamped end, but it will also vastly underestimate the total deflection of the foil. Another method is to consider the U-foil to be a simply supported beam. This assumes the struts do not deflect, but the slope of the end is completely unrestrained, as they cannot take up any moment. This leads to the highest moment occurring in the middle of the U-foil and zero internal moment towards the point where the foil is connected to the strut. This overestimates the deflection throughout the foil. In reality, the deflection and moment will be somewhere between these two simplifications. The struts are not infinitely stiff, but their rotation is also not completely unrestrained.
To account for this, both a fixed-fixed beam as well as a simply supported beam is considered. The worst case scenario for their internal moments is evaluated, to make sure the design will survive either

worst case. The deflection is estimated as an average between the two variants.

Resulting stress

The bending moment and shear load will lead to stress in the material. The stress can be evaluated at each discrete pressure point along the foil. The stress caused by the bending moment is expressed by:

$$\sigma = -\frac{My}{I} \tag{3.11}$$

The skin of the foil and strut is assumed to take up all the bending. The inertia of the shear web is thus not included in the calculation of the stress due to the bending moment.

Bending caused by drag

While not the largest forces on the hydrofoil, the drag resulting from pushing an object through a fluid can still be considerable. The total hydrodynamic drag is complex and depends on several factors, ranging from the shape and size of the object moving through a fluid to the texture of the surface and the amount of lift generated by the hydrofoil.
The total drag load is a composition of several types of hydrodynamic drag forces. An accurate drag distribution can be found using CFD, but an estimation based on 2D infinite wing theory (section 3.3.1) will serve as the input for the analytical design phase as this can quickly be determined.
The total drag is modelled as a distributed load acting on the beam. The same equations as for bending caused by lift (section 3.4.1) apply here, but the second moment of area I is now taken along the other axis to account for the different bending direction.

3.4.2 Shear

Hydrodynamic profiles experience a pitching moment as they produce lift. This will result in torsion of the foil, leading to shear stress. Due to the lift bending load, internal shear load will cause shear stress as well.

Stress due to internal shear

When considering the shear load, it is assumed that all of the shear stress is occurring in the torsion box of the foil, consisting of two spars and the outer skin connecting them.
The shear stress for each section can be found by [33]:

$$\tau_V = \frac{VQ}{It} \tag{3.12}$$

Where V is the maximum local shear load, I the area moment of inertia around the neutral axis, t the width of the cross-section at the point where the highest stress occurs. Q is defined as $\overline{y}$'A', with A' the area above/below the section where the maximum stress is measured and $\overline{y}'$ the distance to the centroid of that area.

Stress due to torsion

The lift distribution generated by a foil acts at the center of pressure [29]. This point does not necessarily coincide with the hydrodynamic center, which is the point around which a foil will pivot when exposed to an unbalanced force. As a result, the foil experiences a pitching moment around its hydrodynamic center, which changes with higher angle of attack (more lift), leading to torsional stress and twisting of the foil. For the analytical model, the total lift load can be modelled as a combination

of the lifting force and a torsional moment applied at the hydrodynamic center of the hydrofoil [29]. For an estimation of the stress caused by the pitching moment of the hydrofoil, the assumption is made that there is no warping due to the torsion, the cross-sectional properties remain constant. Similar to the transverse shear stress, the torsion box is assumed to take up all of the torsion shear stress. The local torsion shear stress in a cross-section is defined as [34]:

$$\tau_T = \frac{M_T}{2A \cdot t_{min}} \tag{3.13}$$

As the thickness of the enclosed section is not uniform, the stress should be evaluated in both walls. For thin-walled closed sections, the torsional shear stress along the thickness is uniform [34]. This means that the shear stress has to be evaluated separately for all occurring wall thicknesses.
To do so, first the area A is determined. This is the area enclosed by the median line of the thin walled section [35] (area inside dashed line Figure 3.9):

$$A = (a - t_1)(b - t_2) \tag{3.14}$$

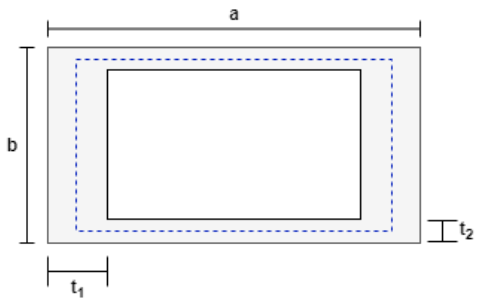

Figure 3.9: Cross-section of torsion box used for stress calculations

Evaluation for both wall thicknesses gives the following equations to be solved for the average stress in the chosen points:

$$\tau_{avg} = \begin{cases} \frac{M_T}{2t_1(a-t_1)(b-t_2)} \\ \frac{M_T}{2t_2(a-t_1)(b-t_2)} \end{cases} \tag{3.15}$$

Angle of twist

The applied torque will cause the hydrofoil to twist. Twisting may change its hydrodynamic properties. Being able to predict the twisting angle of the foil is of importance for both structural safety as well as controllability of the vessel. The total angle of twist can be calculated as follows:

$$\phi = \frac{M_T L}{G I_T} \tag{3.16}$$

With G the material shear modulus and I_T the St. Venant torsion constant.
For the free-end hydrofoil the maximum twist angle occurs at the end, for the U-foil the maximum twist angle is at the midpoint.
The torsion constant is geometry-dependent. For a hollow rectangular profile of non-uniform wall thickness, the constant is defined as [35]:

$$I_T = \frac{2t_1 t_2 (a - t_1)^2 (b - t_2)^2}{a t_1 + b t_2 - t_1^2 - t_2^2} \tag{3.17}$$

3.4.3 Combined loads and principal stress

It can be clearly seen that several loads are acting in different directions at the same time. A combination of bending and shear can possibly lead to higher stresses than estimated based on the individual loads. It is important to consider the principal stresses in the structure to see if the combined loads lead to higher stresses than they would individually.

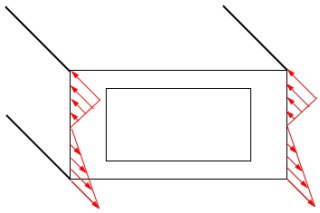

(a) Distribution of bending axial stress

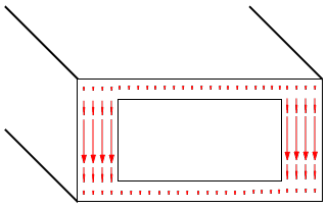

(b) Distribution of transverse shear stress

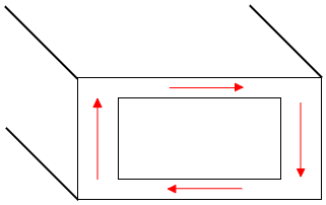

(c) Distribution of torsional shear stress

Figure 3.10: Individual contributions to the principal stresses

Principal stresses are calculated using the following equation [33]:

$$\sigma_{1,2} = \frac{\sigma_x + \sigma_y}{2} \pm \sqrt{(\frac{\sigma_x - \sigma_y}{2})^2 + \tau_{xy}^2} \tag{3.18}$$

The bending moment leads to normal stress over the cross-section (Figure 3.10a), while the internal transverse load causes shear stress (Figure 3.10b). The torque applied by the pitching moment of the airfoil causes torsional shear stress (Figure 3.10c), which is added to the transverse shear stress on one side and subtracted on the other.

In the bending of the hydrofoil, there is no σ_y. The axial component of the bending stress is σ_x. The shear stress τ_{xy} is composed of both the torsion and transverse components and will peak on one side of the torsion box, depending on the pitching moment of the chosen foil.
The principal stresses occur when a combination of the three stresses peaks. The value of the principal stress can be used to determine failure of isotropic structures by comparing it to the yield strength of the material. The method for determining failure of composite laminate structures follows in section 3.9.

3.5 Strut loads - Static analysis

Like the foils, the struts experience several loads in different directions. A schematic overview of the loads is presented first (Figure 3.11).

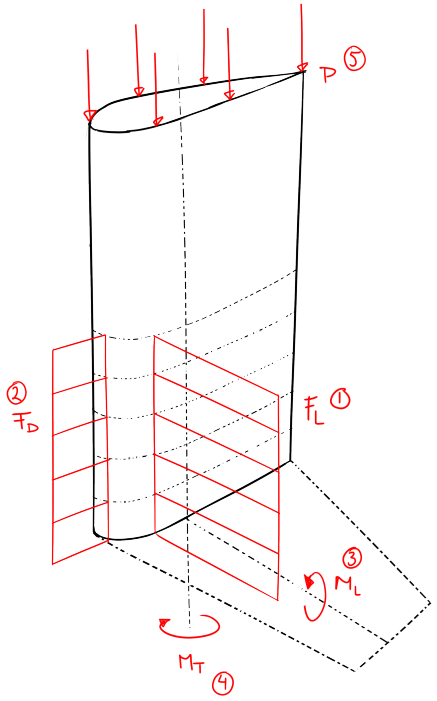

Figure 3.11: Drag, lift and moments caused by hydrofoil on strut

3.5.1 Bending loads

Similar to the foils, the struts generate lift. The methods of determining the bending stress are similar, with some minor additional considerations.

Bending caused by lift generated by the strut itself

During (un)coordinated turning, the struts will experience a relative angle of attack caused by sideslip. This angle of attack leads to the generation of lift by the strut (load number 1 in Figure 3.11). The angle should not exceed 5° [10], as this may lead to ventilation. In extreme cases, the ventilation may creep all the way down to the lifting surface of the foils, diminishing the lifting capacity and causing the vessel to come down. In ventilation of the struts, loss of centrifugal force will lead to a significantly larger turning radius. The lift during the turn will lead to bending in the struts. For the determination of the magnitude of the lift distribution on the struts, an angle of attack of 5° is used, as this would be the worst case. For each foil shape, this corresponds to a specific lift coefficient, C_L (equation 3.6), used to calculate the lift force generated by that strut profile. As in initial estimate, a C_L of 0.5 is used, as this is not an uncommon value for simple symmetric foils at 5° angle of attack [29].

Similar to calculations done for the hydrofoils, the lift is considered as a partial trapezoidal distributed load over the submerged section of the strut.
With the distributed lift load only acting on the submerged section of the struts, the bending moment, transverse load and deflection of the considered pressure points are determined using the same

equations as before (Equations of appendix A.2.1), with only the unloaded out-of-water section being added to the distance *a* in each calculation (similar to the *a* in Figure 3.7a).

Bending due to drag load

While moving through the water at maximum velocity, the struts will experience drag (load number 2 in Figure 3.11). The drag coefficient is known for a given hydrofoil shape, Reynolds number and velocity. The drag load is assumed to be evenly distributed over the submerged length of the strut. The drag will not be the most critical load case as the bending happens over the strong axis of the strut.
The equations for the maximum moment and deflection are identical to moment and deflection caused by lift on the foil, namely equations in appendix section A.2.1.
The worst case scenario for the effect of drag on the strut is during turning, when the strut may generate lateral lift and additional lift induced drag occurs.

Bending caused by foil generating lift

As the hydrofoil generates lift, a bending moment is applied to strut at the connection point. This is modelled as a pure moment applied to the free end of a cantilever beam. This additional moment is added to the bending moment caused by the strut lift (load number 3 in Figure 3.11). The displacement and slope of a beam under pure bending are added to the respective values caused by the lift on the strut, in cases where this is relevant (asymmetric designs). Displacement and slope of a pure moment are described by [33]:

$$\delta = -\frac{M_0 x^2}{2EI} \tag{3.19}$$

$$\theta = -\frac{M_0 x}{EI} \tag{3.20}$$

This does not apply for symmetric T-shaped foils. Due to their symmetry, the bending moment of one side cancels the bending moment of the other side, leading to zero pure bending moment added to the strut.

Torsion in the strut

With the exception of T-shaped foils, the drag on the hydrofoil will lead to a torque being applied to the strut (load number 4 in Figure 3.11). The magnitude of this torque is the maximum value of the bending moment caused by the distributed drag load on the foil, occurring at the root.
Additional torque is applied by the lifting load of the strut. Similar to the foil, the lift is applied at the hydrodynamic center which is usually forward of the centroid of the foil, leading to a pitching moment.
Twisting of the strut is unwanted, as it will lead to an aft rotation of the lifting surface, changing the lifting properties of the hydrofoil as the orientation of the foil in the free stream changes.
The torsion shear stress on the strut and the twisting angle are calculated using equations 3.15 and 3.16, respectively.
Asymmetric hydrofoil arrangements lead to higher torque on the struts, making an increase in size of the struts a necessity. As a result, weight and drag increase.

3.5.2 Axial loads

The most critical load for the struts is the compression caused by the weight of the vessel. During foilborne operation, the entire weight of the ship is supported by the struts. The axial loads due to

compression are added to the axial loads arising from the bending moment. As the struts are not designed for the purpose of generating lift, the compressive stress is expected to be (magnitudes) higher than the axial bending stress caused by the limited amount of lift.

3.5.3 Buckling

Buckling is an important consideration when designing structural elements under high compressive load. Column buckling applies to structural members that have a high length compared to their cross-sectional area. The loads on the struts need to be checked against the maximum allowed buckling load.

Buckling limit

In the case of the struts, the cross-sectional area is relatively large due to the long chord length, but it does have low bending inertia in one direction compared to the other due to the high level of asymmetry.
A column can be classified as short (where usually the material yield stress is exceeded before buckling can occur) based on the ratio between its length and its lowest radius of gyration. If this ratio is below 45, the column can be considered short.

For shorter columns, pure Euler buckling will lead to unrealistically high buckling loads. To adjust for this, a Johnson parabola is used to describe the buckling load for short columns. The buckling limit is governed by the following equations [33, 36]:

$$\sigma_{crit,E} = \frac{P_{crit}}{A} = \frac{\pi^2 EI}{(kL)^2 A} = \frac{\pi^2 E}{\lambda_c^2} \tag{3.21}$$

$$\sigma_{crit,J} = \sigma_{yield} - \frac{1}{E}\left(\frac{\sigma_{yield}}{2\pi}^2\right) \cdot \lambda_c^2 \tag{3.22}$$

$$\lambda_c = \frac{kL}{\sqrt{\frac{I}{A}}} \tag{3.23}$$

With A the cross-sectional area, k the effective length factor, I the area moment of inertia in the weakest (buckling) direction and λ_c the slenderness ratio of the column.

Eccentricity

The load applied to the struts is not a simple axial/compressive load. In reality, at the very least the attached foil exerts a bending moment on the free end of the struts (for non-T-foils). Additionally, asymmetric loads due to control surface deflection lead to an eccentric load. This can be represented as a compressive load applied off-center at a distance e to the neutral line of a column, shown in Figure 3.12b, where c is the distance of the column neutral line to the outer edge.
The added bending moment causes additional axial stresses caused by bending. The column immediately starts to deflect, as opposed to by the sudden deflection upon buckling in the case of centered loads.
The stress in a column under eccentric axial loading is given by [33]:

$$\sigma_{max} = \frac{P}{A}\left[1 + \frac{ec}{k^2} sec\left(\frac{L}{2k}\sqrt{\frac{P}{EA}}\right)\right] \tag{3.24}$$

When considering the worst-case scenario, the struts are generating lift due to sideslip. This lift is oriented perpendicular to the compressive load and will cause deflection similar to the effect of

eccentric loading. More importantly, as the load acts on the free end of the cantilever beam, high axial stress is added to the root as a result of the bending moment. The total stress for buckling is then a combination of the eccentric compressive load and the bending stress at the root. This maximum stress has to stay below the buckling limit defined by Euler and Johnson as defined by equations 3.21.

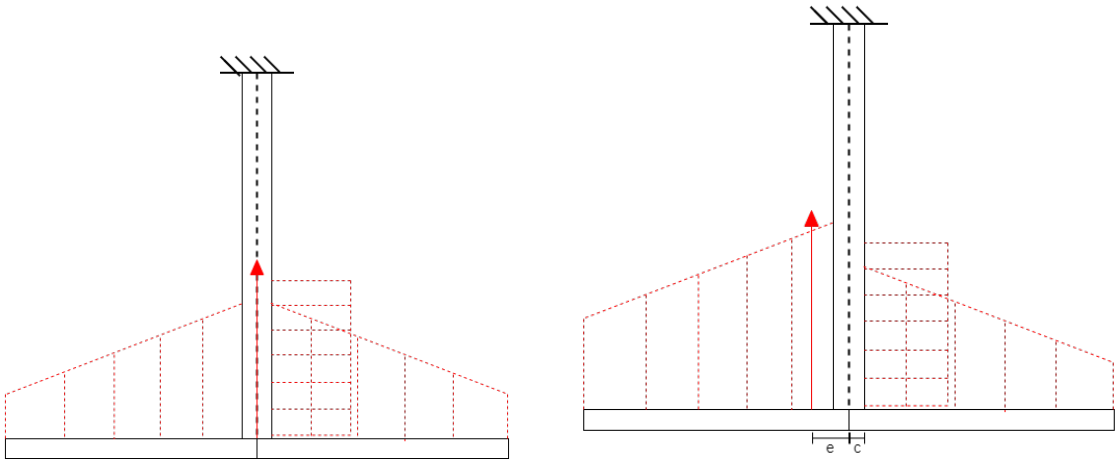

(a) No eccentricity, symmetric load (b) Eccentricity due to asymmetry

Figure 3.12: Eccentricity leading to buckling of strut

It should be noted that if there is an asymmetric lift distribution on a T-foil, the situation of Figure 3.12a does not hold and an eccentric load will be present there as well, Figure 3.12b. This will very significantly impact the design of a single strut system. Asymmetric loads on a T-foil are taken into account by considering deflection of a trailing edge flap on one side (section 3.7). The eccentricity is also the limiting factor for using L-foils, as the eccentricity is very large for a one-sided foil.

Off-center loading for U-foil: simple portal frame

When considering the clamped foil of the U-foil configuration, equation 3.24 does not apply. Using the secant formula will vastly over-estimate the moment, leading to an over-engineered strut. Instead, the U-foil will be considered as a simple portal frame consisting of three rigidly connected elements (Figure 3.13). The load is simplified to a linearly decreasing load.

The moments added to the root of the struts, M_A and M_B, are given by [33, 37]

$$M_A = M_C \frac{1}{(\frac{I_f}{I_s})(\frac{L_s}{L_f})} = -L^2 \left(\frac{w_1}{20} + \frac{w_2}{30}\right) \frac{1}{(\frac{I_f}{I_s})(\frac{L_s}{L_f})} \tag{3.25}$$

$$M_B = M_D \frac{1}{(\frac{I_f}{I_s})(\frac{L_s}{L_f})} = -L^2 \left(\frac{w_1}{30} + \frac{w_2}{20}\right) \frac{1}{(\frac{I_f}{I_s})(\frac{L_s}{L_f})} \tag{3.26}$$

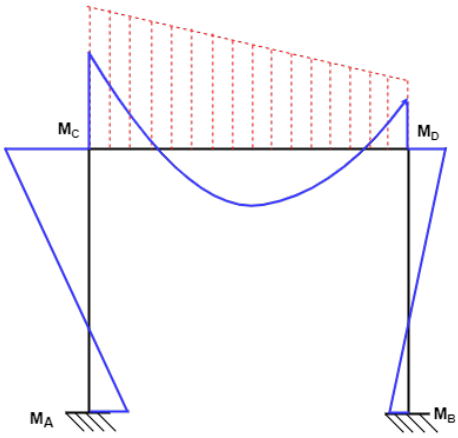

Figure 3.13: Moment in simple portal frame consisting of rigid beams, under linearly decreasing distributed load

The axial stress added by these moments is calculated using equation 3.11 and added to the compressive stress.

3.6 Transverse support ribs

The skins of the hydrofoil can be considered as plates with fixed edges. With a pressure load acting on its surface, the plate will experience stress along the edges and in the center (assuming a uniform pressure load on the plate). The plate will deform under the load. This deflection will influence the outer shape of the hydrofoil, possibly changing its hydrodynamic properties. The magnitudes of the stress and deflection can be influenced by changing the ratio between the length and width of the fixed plate, with the length *a* being the size in the spanwise direction and the width *b* being the distance between the spars (as the plate between the spars is the most critically loaded section). The stress and deflection are given by [35]

$$\sigma_{center} = \frac{\beta_2 q b^2}{t^2} \tag{3.27}$$

$$\delta_{max} = \frac{\alpha_p q b^4}{E t^3} \tag{3.28}$$

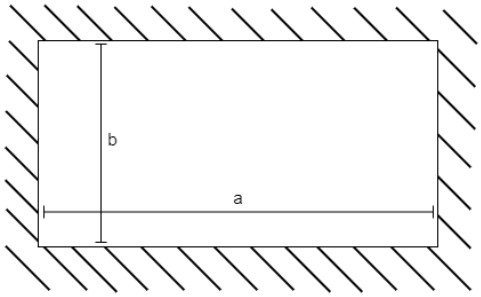

Figure 3.14: Fixed flat plate

The values of β_2 and α follow from tables in literature [35]. q Is the value of the pressure load while *a* and *b* are the geometric values shown in Figure 3.14. A limit for the deflection of the fixed plate can be set, to prevent surface deformation. Similarly, a limit for the stress caused by plate deformation is chosen, for instance, as an estimate, the magnitude of the plate stress can be set

at an additional 15% of the total longitudinal stress. With this limit, a value for β_2 and α can be determined, which in turn can be interpolated to a value for the ratio of $\frac{a}{b}$. This value then gives the value of *a*, which is the necessary spacing between the transverse ribs.

3.7 Trailing edge devices

In order to change the amount of lift a foil generates at a given speed, the hydrodynamic shape needs to be altered. Usually, this is done by means of flaps on the trailing edge (Figure 3.15) that can rotate up or down. Using flaps, the amount of lift generated can suddenly be increased dramatically. This allows for acceleration to foiling-speeds while not generating a lot of lift (leading to lower lift-induced drag) and then taking off when the higher speeds necessary for foiling are reached.
Having moving trailing edge devices has a consequence for the structural strength of the foils and struts. As the flaps are a hinged part, they can no longer be considered as a load bearing part of the structure. Adding a flap or rudder will reduce the effective structural size, leading to higher stresses in the remaining part. The trailing edge flaps and rudders are assumed to run along the entire length of the foils and struts. The diminished stiffness of the structure can then be approximated by disregarding the area of the flaps when calculating the moment of inertia of the cross-section (Figure 3.6).
Adding a trailing edge device will also influence the loads generated by the structure. Deflection of a flap will change the total lift and foil pitching moment of the foil.

Figure 3.15: Trailing edge devices (flaps) on Jetfoil front foil [38]

3.8 Dynamics

When considering a lifting surface with loads that can quickly change in magnitude or direction, a dynamic analysis is an important part of the design. A well-known phenomenon in wing design is aeroelasticity (or in this case, hydroelasticity). Besides static elasticity effects, a coupling of torsional- and bending vibrations can lead to dynamic instability known as flutter. In aircraft wing design, this flutter can quickly lead to catastrophic failure of the structure. However, in hydrofoil design, flutter is not an issue. The higher ratio of the mass of the fluid (water) to the mass of the structure prevents the occurrence of flutter [10].
A proper vibration analysis should be done of the entire vessel including the hydrofoils at a later design stage. Vibrations from the propulsion system will be transferred to the hydrofoil structure, which may have an adverse effect on the structural integrity and fatigue life. This is outside the scope of this research and should be considered at a later design phase.

3.9 Laminate structures

One of the simplifications done so far is that the material is isotropic and that its properties are uniform throughout the structure. This is obviously not the case when considering composite materials. To come to a more realistic material model, CLT is implemented. This allows to take advantage of the unique properties of composite laminate materials and determine the stresses in the structure. Using CLT, the equivalent moduli of a laminate can be determined, which can be used in the beam deflection calculations [39]. The structure is checked for failure using Tsai-Hill. Safety factors for composite laminate structures in shipbuilding are calculated and applied.

3.9.1 Introduction Classical Laminate Theory

CLT is used to determine whether the material fails under the given load. While global stresses may seem low enough to prevent failure, local stresses in the individual plies of a laminate may exceed the material limit.
A brief overview of the steps needed in CLT to go from global loads to local stresses is presented.
The first step is to determine the lamina stiffness matrix, denoted by [C]. The lamina stiffness matrix relates the stress to the strain, as $\{\sigma\} = [\mathrm{C}]\{\epsilon\}$. As the local coordinate system of the fiber material does not necessarily align with the coordinate system of the layer, the stress can be rotated using (the inverse of) a rotation matrix [T] (which includes the angles of the fiber with the layer coordinate system), resulting in the layer coordinate system stress $\{\sigma^*\}= [\mathrm{T}]^{-1}\{\sigma\}$. Similarly, strains can be rotated as well, with the the addition of a Reuter matrix, [R]. Tranformation of strains is then given by $\{\epsilon^*\} = [R][T]^{-1}[R]^{-1}\{\epsilon\}$. Since $\{\sigma\} = [\mathrm{C}]\{\epsilon\}$, the layer stress can now be related to layer strain as follows:

$$\{\sigma^*\} = [T]^{-1}[C][R][T][R]^{-1}\{\epsilon^*\} \tag{3.29}$$

which condenses to:

$$\{\sigma^*\} = [C^*]\{\epsilon^*\} \tag{3.30}$$

This rotated stiffness matrix $[C^*]$ can now be used to relate the strains in the layer coordinate system to the stress in the layer coordinate system.
Using the $[C^*]$-matrix, the deformation resulting from applied loads can be determined for a laminate consisting of several layers. This results in the **ABD**-matrix, relating strains (and by extension, stress) to the loads. In situations where the load is known and the deformation is not, the inverse of the ABD-matrix is used, the **abd**-matrix. This matrix is the core tool of CLT:

$$\begin{Bmatrix} \epsilon_x^0 \\ \epsilon_y^0 \\ \epsilon_{xy}^0 \\ \kappa_x \\ \kappa_y \\ \kappa_{xy} \end{Bmatrix} = \begin{bmatrix} a_{11} & a_{12} & a_{16} & b_{11} & b_{12} & b_{16} \\ a_{21} & a_{22} & a_{26} & b_{21} & b_{22} & b_{26} \\ a_{61} & a_{62} & a_{66} & b_{61} & b_{62} & b_{66} \\ b_{11} & b_{12} & b_{16} & d_{11} & d_{12} & d_{16} \\ b_{21} & b_{22} & b_{26} & d_{21} & d_{22} & d_{26} \\ b_{61} & b_{62} & b_{66} & d_{61} & d_{62} & d_{66} \end{bmatrix} \begin{Bmatrix} N_x \\ N_y \\ N_{xy} \\ M_x \\ M_y \\ M_{xy} \end{Bmatrix} \tag{3.31}$$

3.9.2 Stiffness

Previously, in section 3.4.1, the area moment of inertia of the hydrofoil and its torsion box has been determined. Together with the modulus of elasticity, the moment of inertia can be used to determine the deflection of a beam under a load. This is under the assumption that the material is homogeneous and isotropic. By definition, for composite laminates, this is not the case. As the fiber lay-up is different for the shear webbing and the outer skin, so are their respective equivalent moduli. The modulus of a laminate is also different for each loading direction.

To use the laminate properties in the analytical expressions, replacement stiffnesses need to be found, for bending ($\widehat{EI}_{yy}$, $\widehat{EI}_{zz}$), tension ($\widehat{EA}$) and for torsion ($\widehat{GI_T}$) [40].

3.9.3 Torsional stiffness of torsion box

The torsional stiffness of a composite closed section beam such as the torsion box is used to determine the angle of twist (section 3.4.2). The replacement torsional stiffness of the hollow beam, $\widehat{GI_T}$, is given by:

$$\widehat{GI_T} = \frac{2(a-t_1)^2(b-t_2)^2}{a_{66,skin}(a-t_1) + a_{66,web}(b-t_2)} \tag{3.32}$$

where the values of *a* and *b* are the width of the flange and web respectively, analogue to the values used to determine the St. Venant constant for isotropic beams in Figure 3.9.

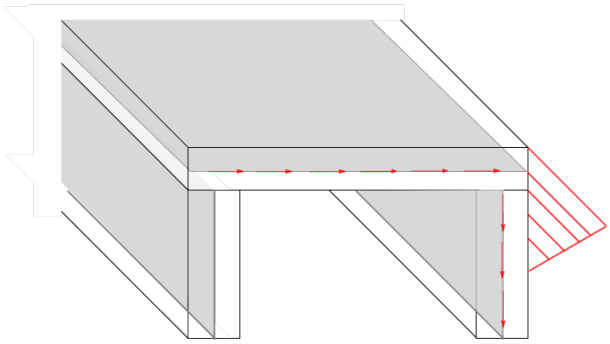

Figure 3.16: Upper part of torsion box (lower skin missing), including the shear webbing and top foil skin. Midplanes of each plate are shown in grey

3.9.4 Bending stiffness of hydrofoil skin

The replacement bending stiffness of the hydrofoil skin can be determined with composite beam theory. The plates that form the outer skin are not flat, which is normally the case for laminate theory. To determine the bending stiffness of this hydrofoil beam, the theory for displacements of arbitrary cross-section beams is applied. There is an important condition for this theory to be valid, which leads to some limitations on the laminate properties: there can be no tension-bending-torsion coupling present in the beams [40]. There are three situations in which this is true:

1. The layup of the laminate is **orthotropic** and **unsymmetrical**, the cross-section **arbitrary**
2. The layup of the laminate is **orthotropic** and **symmetrical**, the cross-section **arbitrary**
3. The layup is **arbitrary**, the cross-section is **symmetric** with the loads applied in the symmetry plane

The third condition is valid for the symmetric struts. From the other two cases follows that for this theory to be valid, the lay up has to be orthotropic. This means that in the ABD-matrix of the laminate, the values of $A_{16} = A_{26}{=}D_{16}{=}D_{26}$ as well as all the values in the B-matrix are zero. If the orthotropy condition is met, the replacement stiffness of the arbitrary cross-section is described by (variables in Figure 3.17):

$$\widehat{EI}_{yy} = \int_S (\frac{1}{a_{11}} z^2 + \frac{1}{d_{11}} cos^2\alpha) d\eta \tag{3.33}$$

$$\widehat{EI}_{zz} = \int_S (\frac{1}{a_{11}} y^2 + \frac{1}{d_{11}} sin^2\alpha) d\eta \tag{3.34}$$

The tensile stiffness is similarly given by

$$\widehat{EA} = \int_S (\frac{1}{a_{11}}) d\eta \tag{3.35}$$

A laminate is orthotropic only if all fibers are aligned with the principal axes of the laminate, severely limiting the lay-up choices. This is not very suitable for a real application. To check whether this formulation can still be used with any measure of accuracy, the replacement stiffness is compared to the value found when multiplying the engineering constant E_x (extracted from the *abd*-matrix, $E_x = \frac{1}{a_{11}t}$) with the value for the inertia used previously to determine the isotropic bending stiffness. The difference between these two approaches is found to be less than 1% when applying non-orthotropic lay-ups. With this deviation in mind, the theory is deemed still useful for the initial desig-

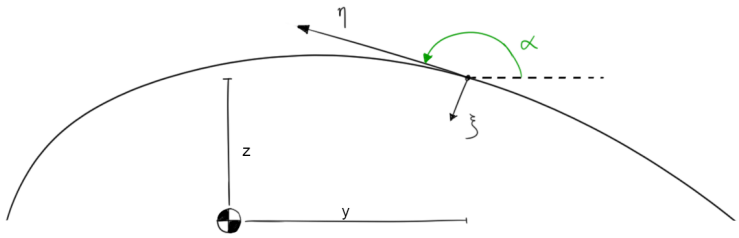

Figure 3.17: Composite beam with arbitrary cross-section

3.9.5 Loads on composite plates

The input to CLT are the loads present on the edges of each plate. These loads are determined from the stresses found in section 3.4.1. Two separate load vectors are needed to describe the stresses in the laminates. First, the load vector of the foil skin is given.
The main stresses in the foil skin are the axial stress and the torsional shear stress. The axial stress can be represented as the sum of stresses caused by a normal load, N_x, and a bending moment, M_x (Figure 3.18 [40]). The torsional shear stress can be represented by a shear load, N_{xy}. The value of N_{xy} is found by multiplying the skin torsion shear stress of equation 3.15 by the plate thickness, yielding the shear load per meter.
The value of N_x and M_x are found by taking the stress at the outer laminate edge and the inner laminate edge (Figure 3.18). Assuming a symmetrical layup, the value of stress resulting from M_x is zero at the midplane, which gives the value of N_x. The value of M_x itself is found by taking the difference between the midplane stress (only N_x) and the top edge stress ($N_x + M_x$). The moment can be derived from this by applying equation 3.11.

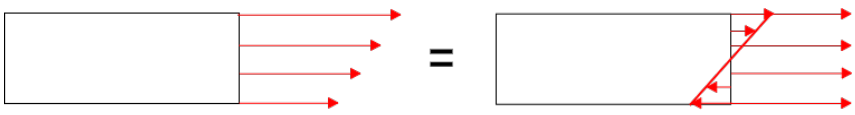

Figure 3.18: Equivalent load and moment of a linearly varying axial load on laminate

Additionally, the drag causes a bending moment along the other axis of the plate. This leads to compression and tension of which the values do not vary between the plies, acting perpendicular to the stack. The stress caused by the drag can then be added to N_x and M_x, and the highest value (worst-case) will be considered. This value is taken as a constant value along the entire width of the

plate (dashed blue line in Figure 3.19a).

The plies of the shear webs are perpendicular to the bending stress caused by the lift. This means that the stress varies along the edge of a ply, but not between plies, similar to the drag on the skin. The worst axial stress occurs at the top and bottom edge of the shear web, where it connects to the foil outer skin. In CLT, this worst-case stress is taken as a uniform axial stress along the entire edge, leading to a uniform worst-case axial load N_x (Figure 3.19b, red dashed line).

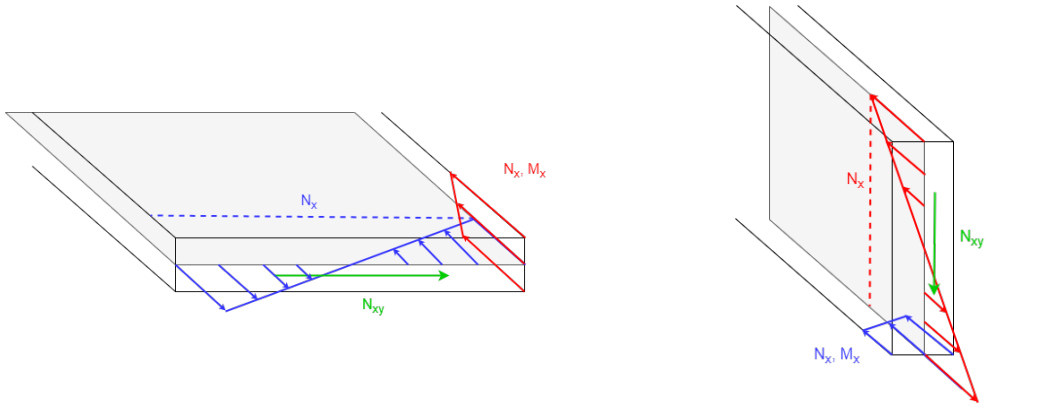

(a) Loads on foil skin laminate

(b) Loads on shear web laminate

Figure 3.19: Loads on laminates

The main load acting on the web is the shear. Using the total combined shear stress (section 3.4.3) multiplied by the web plate thickness, the shear load N_{xy} is found.
The load vector applied to each of the laminates of the skin and the shear webs are then, respectively:

$$\begin{Bmatrix} N \\ M \end{Bmatrix}_{skin} = \begin{Bmatrix} N_x \\ 0 \\ N_{xy} \\ M_x \\ 0 \\ 0 \end{Bmatrix} \qquad \begin{Bmatrix} N \\ M \end{Bmatrix}_{web} = \begin{Bmatrix} N_x \\ 0 \\ N_{xy} \\ M_x \\ 0 \\ 0 \end{Bmatrix} \tag{3.36}$$

3.9.6 Lay-up

The lay-ups of the laminate skin and webs differ. The laminate skin lay-up of the struts also differs from that of the foil due to the added compression. To determine an effective lay-up, their individual loads must be considered.
To prevent unwanted coupling between extensional and bending loads, a symmetrical lay-up is preferential. A non-symmetrical lay-up can lead to warping during the curing stage, changing the shape of the foil and leading to internal residual stresses. [41]. No optimization on the stacking sequence is done, but general practices from composite aircraft design [42] are taken into account. All lay-ups should include at least reinforcement in the three main directions ($0/90/\pm45$).

Foil skin layup

The skin of the foil has to deal with significant bending. As a result, high tensile and compressive loads are present. To minimize deflection, it is preferred to have very stiff material as far away from the neutral axis as possible. This is achieved by making the outer layers of the laminate align with the highest loads. For the foil, the outer layers need to align with the N_x load. This corresponds to

[0°] layers.
As a unidirectional beam would be very stiff against a single bending direction but very torsionally weak, just 0° layers are not sufficient. To counter the (torsional) shear, ±45° layers need to be added. As the axial loads are significantly higher, the [0°]-layers will make up the largest fraction of the laminate. The initial lay-up for the foil skin is chosen to be:

$$\mathbf{[0_2/90/45/\text{-}45]}_{2s}$$

Foil shear web layup

For the spars, the most critical load is the (torsional) shear load. This is best taken up by ±45° layers. Just shear layers will not have the desired result, as the shear web is still subject to bending (albeit less than the skin). The extensional/compressive load caused by the lift is uniform across the width of the shear web (as stated in section 3.9.5). The load caused by the drag linearly varies with the distance to the centroid. The shear web is also responsible for maintaining the separation between the top and bottom skin, leading to the addition of some 90° layers. The 45°/-45° layers are positioned at the outside of the laminate [42]. The initial lay-up for the shear webs is chosen as [43]:

$$\mathbf{[45/\text{-}45/45/\text{-}45/0/90]}_{2s}$$

Strut skin layup

The loads on the strut differ from those on the foil. The addition of the compression caused by the weight of the ship means that the focus will be on longitudinal reinforcement even more. The layup for the strut skin is chosen to be

$$\mathbf{[0_3/90/45/\text{-}45]}_{2s}$$

Strut shear web layup

The strut webs have a similar function to the foil webs. In reality, the strut webs will also be subjected to compression. For the simplified analytical model, all compressive loads are assumed to be carried by the strut skin. The initial strut web lay-up is decided to be identical to the foil web lay-up,

$$\mathbf{[45/\text{-}45/45/\text{-}45/0/90]}_{2s}$$

3.9.7 Buckling of composite beams

Analogue to the response of a composite beam under loading, composite beams behave very similar to isotropic beams in terms of buckling conditions. The equations of section 3.5.3 can simply be adjusted to calculate the composite beam buckling limit by using $\widehat{EI}$ where normally *EI* is used [40]. The equation for the critical load then becomes:

$$P_{crit} = \frac{\pi^2 \widehat{EI}_{yy}}{(kL)^2} \tag{3.37}$$

Only $\widehat{EI}_{yy}$ is considered for the critical load. This is the bending stiffness in the weak direction, which is orders of magnitude smaller than the bending stiffness over the strong axis (drag). The strut will buckle long before the loads for this strong direction are reached.
Where applicable, the eccentric stress for a composite beam can be calculated by replacing *EA* by $\widehat{EA}$ in equation 3.24.

3.9.8 Failure

Composite laminate structures show different failure modes than traditional metallic structures. In this section, the different types of failure are discussed [42, 44].

Matrix failure

As the matrix and the fiber reinforcement have very different properties, the matrix may crack under certain loading conditions. Tension in the matrix is a combination of both the mechanical loading as well as (production-induced) thermal stresses. The thermal expansion coefficients of the matrix are much higher than those of the reinforcement. This means that during cooling, the matrix material will shrink more than the fiber, leading to internal stresses and possible warping of the part. These internal stresses lower the loading capacity of the matrix, leading to cracking under mechanical loading.

First ply failure

The first ply failure is the stress at which the limit strength of a lamina in the laminate is exceeded. According to the criteria set by BV on shipbuilding [45], the first ply failure load has to be considered as the complete laminate failure load. First ply failure can be calculated using the maximum stress criterion:

$$-S_{1C} < \sigma_1 < S_{1T} \tag{3.38}$$

$$-S_{2C} < \sigma_2 < S_{2T} \tag{3.39}$$

$$S_6 > |\sigma_6| \tag{3.40}$$

Where the $S_{n,T}$ and $S_{n,C}$ mark the respective ply strength. The maximum stress criterion is incapable of considering the effect of transverse loading on longitudinal strength [44]. The hydrofoil will always experience multiple loads in different directions, so maximum stress is not suitable to determine laminate failure.
Ply failure can also be determined by quadratic maximum stress theories. This allows for the analysis of plates under multiaxial loading. The theory used is the Tsai-Hill theory, which predicts that a laminate will not fail if:

$$\frac{\sigma_1^2}{S_1^2} - \frac{\sigma_1\sigma_2}{S_1^2} + \frac{\sigma_2^2}{S_2^2} + \frac{\sigma_6^2}{S_6^2} < 1 \tag{3.41}$$

The values for the strengths S_1 and S_2 depend on whether the load is compression or tension. If σ_1 and σ_2 are < 0, the respective compressive strengths $S_{1,C}$ and $S_{2,C}$ should be used instead of $S_{1,T}$ and $S_{2,T}$ [42, 46].

Ultimate laminate failure

Single ply failure does not always immediately mean that the laminate itself has failed. In most cases, the rest of the plies still provide sufficient stiffness to carry the load [44]. Incremental increase of the load through an iterative process will lead to the redistribution of the loads over the laminae and ultimately the failure of the remaining plies. When the laminate is no longer able to withstand the load, the ultimate laminate failure has been reached. Due to certification standards, this cannot be applied to hydrofoils as a failure criterion.

Delamination/transverse failure

Delamination, or interlaminar failure, is a failure mechanism that frequently occurs in laminated composites. The root cause lies in the transverse (shear) stresses that can occur in a laminate.

Delamination is considered very difficult to predict. Whether delamination occurs depends on the total state of stress in the laminate, which is dependent on several variables such as stresses introduced in manufacturing or small defects, in addition to the load on the laminate [42]. Especially the external variables such as the presence of voids caused during production make it impossible to create a reliable prediction of delamination.

Fatigue

A common failure mechanism for metal structures is fatigue. Due to cyclic loading of a structure, the material can fail even if the loads were far below the ultimate strength of the material. This phenomenon has been documented extensively for metal and is an important consideration for the structural integrity throughout the lifetime of a structure, prescribing design choices for better fatigue life. However, for composite structures, this is not as straightforward or well-documented [47]. Fatigue behaviour is generally tested on coupons and rarely on entire structures. Combined with the fact that often, structures fail on delamination rather than failure of the fiber itself, modelling fatigue behaviour of composites is complex and beyond the scope of this research. More often than not, composites are considered resistant to fatigue and in many marine structures the fatigue is neglected [48].

3.9.9 Safety factors

An important aspect of design with composite materials is the use of safety factors. Safety factors are also applied in design with traditional isotropic materials. They are used to account for the variations in the loads (for instance, sudden gusts increasing the load on a structure) and the material strength (diminished strength due to local minor production defect) [49].
In the structural design of aircraft structures, a safety factor a 1.5 is a widely used and accepted value when considering metals. This is also assumed to be valid for the structural design of hydrofoils, as the design and loading conditions are very similar to aircraft structures. In the analytical model, the safety factor is applied to the yield strength of the chosen material.
Such a single safety factor value is harder to determine for composite structures. This is in part due to the wide variation in production processes, each with their respective chances of introducing defects such as voids. Besides that, composite materials exhibit very different failure modes from metallic structures, leading to the development of different methods to find an applicable safety factor. For shipbuilding, BV [45] has a set of guidelines to determine the composite material safety factors based on the composition of several partial safety factors. These are determined by evaluation of the production process, loading conditions and laminate type.
The following partial safety factors are taken into account for the determination of the total composite safety factor for marine applications:

1. C_v, Ageing factor of monolithic laminates and skins: 1.2
2. C_f, Fabrication factor for infusion and vacuum processes: 1.15
3. C_i, Load factor based on the prevalent loads (external sea pressures, local internal pressures): 1.0
4. C_R, Stress factor for tensile and compressive loads parallel to the fiber direction (woven, tri-UD): 2.1-2.4

The total safety factor (SF) for the minimum stress criterion is defined as:

$$SF = C_v C_F C_R C_i \tag{3.42}$$

This gives a safety factor of 2.898 for the composite structure. This safety factor will be applied to the strengths used to calculate whether or not first ply failure occurs (equation 3.41).

4 | Optimization tool

4.1 Introduction

The analytical expressions need to be applied in an iterative tool. An optimization function is created to describe the objective, constraints and inputs of the structural optimization tool. Additional input parameters necessary for the tool are presented, as well as a graphical overview of the iteration method. Some identified shortcomings of the tool are discussed briefly. A global overview of the steps taken in the tool are given in Figure A.1 in the appendix. The interface of the tool displaying the mandatory input variables is shown in appendix A.8.

4.2 Optimization function

Structural optimization is done from a volume minimization standpoint, as volume has a significant influence on the drag of the structure. The objective, constraint and input functions are given. The optimization problem can be described by:

$$min(V_f(t, c, \frac{t_f}{c}))) \tag{4.1}$$

The objective is to minimize volume V_f consisting of the cross-sectional area A and the sections of the span b that have a uniform cross-section. The value of A is found by integrating the thickness of the foil profile along the chord from the leading edge to the trailing edge.

$$O: \qquad V_f = A \cdot b = \int_{LE}^{TE} t \; dc \cdot b \tag{4.2}$$

The optimization is constrained by the failure of the material, expressed by the maximum stress σ_{max} allowed by the failure criterion under consideration (either the principal stress or the maximum ply stress).

$$C: \qquad = \sigma_{max} \tag{4.3}$$

The design input variables are the skin thickness t, chord length c and foil profile-thickness to chord ratio N $= \frac{t_f}{c}$:

$$I: \qquad = t \qquad \textit{for} \qquad 0 < t \leq \frac{1}{4}(t_f) \tag{4.4}$$

$$= c \qquad \textit{for} \qquad t_f(c + \Delta c)_N \leq t_f(c)_{(N+\Delta N)} \tag{4.5}$$

$$= N = \frac{t_f}{c} \tag{4.6}$$

The input variables are increased in the order they are presented, as they are ranked from least to most detrimental to the hydrodynamic performance. The thickness of the skin found in equation 4.4 is limited to a quarter of the total profile thickness. This prevents unreasonably thick skin or even solid profiles. Equation 4.5 limits the increase of the chord length to the point where the profile thickness t_f with chord c equals the profile thickness of a foil with a shorter (initial) chord length but a higher value for $\frac{t_f}{c}$. $\frac{t_f}{c}$ is not a direct input variable, but an important geometrical property of the hydrodynamic profile. As such, it strongly influences the bending stress and inertia of the foil as well as the total load on the structure.

4.3 Input parameters

Several properties need to be decided on to give the iterative tool a starting point. These properties mainly have to do with (intended) performance and ship lay-out.

4.3.1 Global ship layout

Based on the size of the vessel as well as stability criteria put down by BV [31], decisions must be made on the position and number of foils that are to be added to the ship. Longitudinal position affects front-aft stability and seakeeping while lateral position affects rolling stability and practical limitations such as docking capabilities (as the foils cannot extend beyond the side of the ship). Lateral stability also has certification requirements, to prevent capsizing under all conditions. Lateral positioning has no influence on the load balance in the structure and is not a required input.
The number of foils determines the distribution of the total load for each foil, but also influences the magnitude of the drag. This is in part an optimization problem, as more foils can mean smaller geometries leading to lower drag, while increasing the number of structural elements in the water, increasing the drag. A more advanced optimization routine or inclusion of CFD in the design is needed to properly take this into account.

4.3.2 Foil geometry

As the performance of the hydrofoiling vessel is largely dependent on the hydrodynamic performance of the foil, a suitable geometry needs to be chosen that is acceptable from both a structural and hydrodynamical point of view. The efficiency of a foil is strongly correlated with its aspect- and taper ratio (section 3.3.1).
Included in the performance-based decisions is the choice for the size of the trailing edge devices, as this determines the take-off performance and speed. Again, a compromise between performance and structural strength must be made. The trailing edge devices should be sufficiently large to create the required forces to lift the ship out of the water or roll the ship along its longitudinal axis. Exact sizing of control surfaces is beyond the scope of this report, so for the conceptual design assumptions on the size will be made, as discussed later in Chapter 6.

4.3.3 Strut length

The ride height of the vessel determines how significant waves can be smoothly navigated. Together with the submerged length, this determines the total length of the struts. The submerged strut length has to be equal or greater than the length of the chord at the root of the foil, as the foil needs to be at least one chord length below the water surface for lift to be constant [8].

4.3.4 Material choice

For both the metal and FRP design, a specific material has been chosen. This has been done after investigation of several candidate materials potentially suitable for this specific application. The comparison of the materials can be found in appendix A.3, which compares several properties of a selection of materials using charts taken from Granta Edupack. The materials have been compared, among other things, on their volume and cost per unit of stiffness as well as per unit of strength. For the metal concept, UNS S32750 super-duplex steel [50] has been selected. The FRP concept will be designed using Torayca M55J High-Modulus carbon fiber [51] in an epoxy matrix, at 50% fiber volume fraction. This is a realistically attainable fraction for many production processes.

4.3.5 Lay-up

The angles of the laminae in the laminate are a fixed parameter for the iterative tool. Letting the lay-up be a variable would create a multi-variable optimization problem, while at the same time the analytical expressions are not well-suited to optimize the lay-up. Due to the fundamentals of 2D beam theory, the optimal lay-up result would be unidirectional, as warping of the cross-section would not be taken into account when determining the deflection. For this reason, pre-determined (non-optimized) lay-ups are implemented in the code.

4.4 Optimization

Optimization of a hydrodynamic structure is a complex problem that is often solved in industry by applying computationally intensive methods (section 2.3). As the focus of this work is not purely on the optimization of a tool, a simple and straightforward optimization routine is proposed as a first step. The result from the proposed routine is by no means the true optimum as it is based on the simplified analytical model and optimizes for a single objective using only failure as the constraint.

4.4.1 Critical loads

In order to perform an initial optimization of the design, the critical loads and stresses have to be identified. The highest stresses in the structure occur in single strut foils. As discussed in section 3.5, the stress in the strut is a combination of the compression due to the weight of the vessel and the axial bending stress caused by lift on the strut.

4.4.2 Initial optimization of strut

Minimization of the amount of material used to create the foil structure starts at the struts.

1. With high compressive loads in the struts, the struts are the critical structural part in which failure is most likely to occur

2. Increasing the size or profile of the strut has an effect on the drag without any benefits to the performance. The strut layout can be altered, which has an influence on the foil design (by for instance changing it to a twin-strut U-foil instead of a single-strut T-foil). Dimensioning the strut first will prevent double work

There are several methods to increase the strength of the struts. Ideally, strength increasing measures have no adverse effect on the (hydrodynamic) performance of the system. Increasing hydrofoil skin thickness has the least influence on the hydrodynamic properties, especially when increasing the thickness only towards the inside of the structure. The positive effect of increasing the skin thickness is also very limited. Additionally, the outer skin thickness can only be increased so much until the profile becomes solid. When this is the case, the torsion box has also disappeared, which influences how well the strut can deal with the shear stresses.
The next step is to increase the size of the strut. This will proportionally increase both chord length and profile thickness, increasing the bending resistance and cross-sectional area capable of resisting the compression. The increase in size will allow for further increasing the skin thickness, creating more cross-sectional area.
The drawback is that the strut will generate more lift due to the longer chord length and greater profile thickness, while also experiencing more drag.
Finally, a different thickness-to-chord ratio can be chosen for the profile. Essentially, this means choosing a new hydrodynamic shape, leading to different performance. A thicker profile for the same chord length will increase the bending stiffness, the cross-sectional area (compressive stiffness) and

allows for further increase of the skin thickness. At the same time, it will lead to higher lift values at the same chord length (increasing the bending moment at the root) and more drag, damaging the performance.
The main objective is to keep the volume, weight, drag and lift as low as possible while remaining within safe margins for the strength of the structure. The steps of this initial optimization scheme are shown in the schematic of Figure 4.1. A similar scheme is followed for isotropic material, using principal stress and yield strength instead of Tsai-Hill failure criterion.

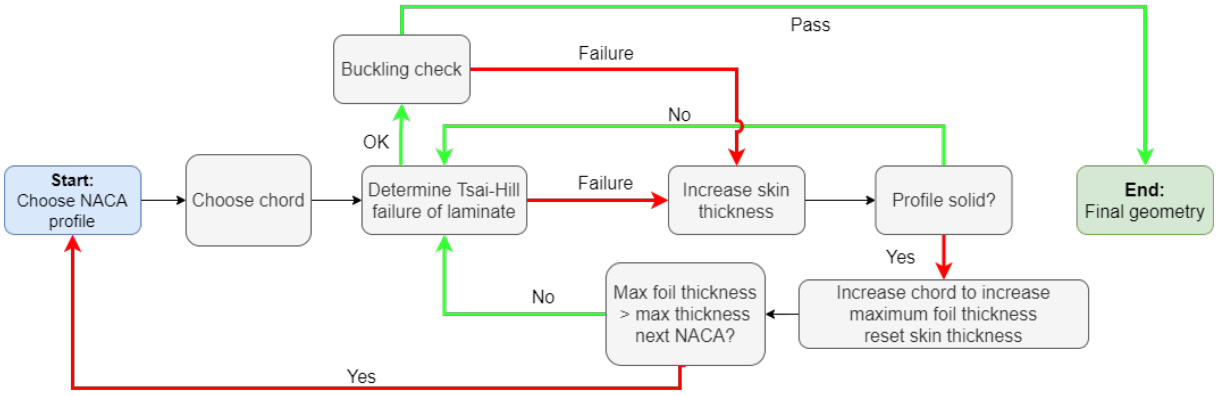

Figure 4.1: Flow schematic of geometry optimization

4.4.3 Optimization of foil

Optimizing the foil geometry for minimal strength is not as straightforward as optimization of the struts. The first step of optimization is identical: increasing the skin thickness of the foil to deal with the bending load. Because of the possible taper angle on the foil, the available height of the profile is limited at the tip. The skin thickness can be increased until the profile is solid at the tip.
The next step in optimization would be to increase the chord length to proportionally increase the profile height, again allowing for thicker skin.
As the chord and span of the foil are connected through the aspect- and taper ratios, changing one of either would immediately change the size of the foil, increasing its area and altering the hydrodynamical performance. This means that this optimization step can not be approached from just a structural point of view. This problem may come in to play when the performance requirements dictate that a very slender foil is necessary.

4.5 Limitations of analytical model

During development of the analytical tool, some shortcomings were identified that have a direct impact on the validation and subsequent application in the case study.

4.5.1 Overestimation of stress

When considering isotropic material, analysis of complex shapes is relatively straightforward. This is not the case for composite structures. As each section has different properties for different loading directions, it is more complicated to reach a single value for the stiffness and strength in any one direction. Because of this, the choice was made to separate each structure into two loaded elements: the skin and the torsion box. The torsion box is then assumed to not carry any of the axial stress in the structure, only the torsional stress. This makes sense from the bending stress point of view, as the spars do little to resist this stress as their inertia is low compared to the skin. Contrary to this, the spars could have a beneficial effect on the load capacity of the strut when considering the

compressive load from the weight of the vessel. This axial component is dependent only on the area of the cross-section, which the model now assumes only to consist of the foil skin. This means that the analysis underestimates the strength of the structure, leading to an over-engineered geometry. In reality, the load bearing area is larger, leading to lower axial stress in the skin than used currently.

4.5.2 Engineering judgement

The optimization scheme will keep calculating whether or not the laminates will fail for increasing sizes. At some point, it will reach a geometry that will not fail, but this may be an unrealistically large geometry. It is up to the designer to judge whether the design seems realistically usable or not. The design can be optimized again by adding an extra strut, but as this has implications for the performance, careful consideration should be taken before deciding on adding the struts.

5 | Validation

5.1 Introduction

The results from the analytical solutions found using MATLAB are to be verified numerically to be able to conclude on the accuracy of the tool. A model of the hydrofoil is built in Siemens NX, which can be exported to its FE suite. The FE model will be processed by Nastran, using a dedicated composite laminate function in NX to create composite structures. The properties of these laminates can be exported and checked against the results found in MATLAB.
Validation is done by building the simplest elements and testing them separately. This is to rule out any interference between parts, similarly to how the analytical model determines the loads and resulting stresses. The initial validation design is found by using a displacement of 45.000kg and a 40-60 front-aft weight balance for the foils as inputs to the analytical tool. All of the results are tabulated in appendix A.4.

5.2 Validation method

The initial analytical design can be validated using several methods. The lower cost option is to model the results in FE and compare the results to the estimation. A more involved method is to create a testable prototype of the analytical design. This requires additional testing of the material to determine the real properties and a definition of the production process by which the prototype is made, to include the effects of, among other things, bonding and voids. Clearly, FE is a more suitable validation solution for this early stage of the design process.

5.2.1 Model and mesh

The hydrofoil design will be imported to Siemens NX by means of a file containing XYZ-coordinates. A ruled zero thickness surface is created between the two cross-sectional profiles at the extremities of the foil. The model is meshed with 2D CQUADR-elements. These are improved plate elements well suited to model curved geometries [52]. Nastran documentation advises using CQUAD4 or CQUADR elements for relatively flat plates and to avoid triangular elements as much as possible. For tapered foils, complete avoidance of triangular elements is not possible. The element size is determined by a simple mesh sensitivity study, testing for 150, 100, 50, 25, 10 and 5mm elements until no more significant improvement of the results is found. Using the isotropic model of the tapered beam, the results stop improving noticeably beyond an element size of 10mm, so this value is selected for the mesh.

5.2.2 Pressure load

The analytical model is built on 2D theories. In 2D, the pressure (lift) is represented by a distributed load along the length of the foil. In reality, the pressure also has a distribution along the chord of the foil. Applying the pressure as a uniform load across the entire surface of the foil is an unrealistic representation of reality, as the trailing edge of the foil is loaded much less than the midsection and leading edge (Figure 5.1a).

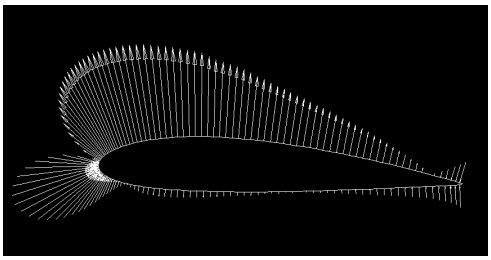

(a) Example pressure distribution over NACA 2414 foil, generated using XFOIL 6.99 [30]

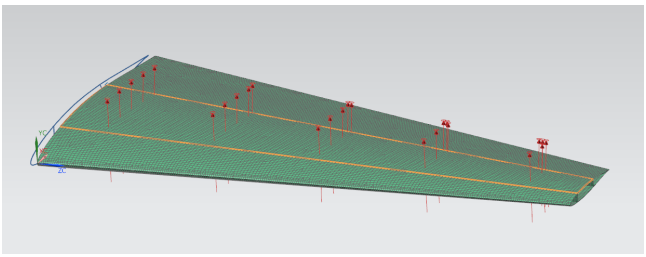

(b) Uniformly loaded section, between orange lines marking the internal spars

Figure 5.1: Simplification of pressure distribution over foil

Uniform pressure across the entire foil surface will lead to severe distortion of the foil due to twisting. Instead, as a simplification, an equivalent pressure load is applied to the area between the spars, seen in Figure 5.1b. While this is also a compromise, applying the load at the midsection will reduce the amount of (unrealistic) twisting in the foil.

5.2.3 Constraints

Although in reality this will never be truly the case, the separate elements are constrained by means of fixed boundary conditions. The real boundaries of the foils will not be fully fixed in all 6 degrees of freedom, as for instance the connection between the foil and the strut will allow for some rotation and translation. The fixed condition follows from the clamped cantilever beam assumption in the analytical model. Additionally, the U-foil boundary conditions are also modelled with simply supported boundary conditions, in line with the analytical model.

5.2.4 Additional considerations for composite simulations

Due to their orientation-dependent properties, some extra care needs to be taken when running a FE simulation for a laminate structure.

ABD-matrix

The most basic and fundamental check to be performed is comparing the ABD-matrix from MATLAB to the one generated by Nastran. The input for MATLAB is the micromechanical model of a ply obtained from U20MM [53]. Nastran requires the fiber and matrix material properties as an input and calculates properties using its own micromechanical model. Because of this slightly different starting point, small differences occur in the ABD-matrices between MATLAB and Nastran. The micromechanical model from NX is leading and copied to MATLAB as well to guarantee that the ABD-matrix is fully identical, removing the error entirely during validation.

Orientation of meshed elements

Elements in a FE mesh are assigned an orientation. Because of the directional properties of the material, it is critical to check that the orientation of the mesh elements all point in the same direction. As the material properties are applied at the element level, it is important that a local 0° angle is properly aligned with the global coordinate system so that angles between elements do not differ. The lay-up of the laminate is defined in the global coordinate system as well.
As some models may include non-rectangular elements, getting every single element to align perfectly will prove difficult, but the great majority of elements should be aligned for the best results.

5.3 Validation results

The results of the FE validation are split in two parts. Both isotropic and FRP structure validation results are discussed in this section.

5.3.1 Isotropic model

A CQUADR PSHELL 2D mesh to which the necessary thickness is added is used for the isotropic FE model. The results of the displacement in FE and MATLAB for isotropic material (AISI 310SS, standard available in NX, only for validation purposes) are given at the end of the tables in appendix A.4 for each situation. Isotropic designs were found to be within 3.4% error (where the FE results are higher than expected) at worst. Otherwise, FE outperformed the analytical estimations by up to 32.5%. The only exception is the fixed U-foil result, for which the FE deflection was found to be 75% higher. Inclusion of the spars in the model reduced this back to -2.1%.

5.3.2 Composite model

The FRP beams are modelled with the 2D CQUADR Laminate shells, applying material data from U20MM. As a fiber, "Torayca J300JB" is selected and combined with "General Epoxy" at a 70% fiber volume fraction, CCA material model [53].
FRP structure results varied more than the isotropic results. For some lay-ups poorly suited to deal with bending (consisting of mostly transverse reinforcement in a boxwing, $[0/90_5]_{2s}$), no reasonable solution is found as the foil still fails even when solid. This is a limit on the tool for some geometries/foil sizes, but as these lay-ups are not realistically usable, this is of no concern.
Laminates that were closer to quasi-isotropic (QI) lay-ups performed better than laminates consisting of mostly longitudinal reinforcement. For QI, FE results were 20% to 30% better than analytically calculated. However, for higher longitudinal content, the results were off by between 20% and, in the singular case of only longitudinal reinforcement, a staggering 2300%. Adding the spars to this reduced the high error to much lower values (a factor of 12 for the worst error) and lead most lay-ups to fall within an accepted 10% margin of error, or outperform the analytical model. All deflections are tabulated in appendix A.4. Further discussion and comparison of the results follows in section 5.4.

5.4 Discussion of validation results

In this section, the results and the possible reasons for deviations between the analytical and numerical models are discussed.

5.4.1 Isotropic results

The FE results for isotropic structures match the expected deflection results from the analytical tool well. All configurations are within a 10% error range or are outperformed by the FEM results, except for the U-foil with a fixed boundary condition. Figure 5.2 shows that the displacement of the clamped foil in FE is almost double the expected analytical result for this structure (13.86mm in FEM against 7.93mm for the tool). In Figure 5.2b can be seen that the deflection is not uniform along the chord: the trailing edge of the foil deflects 30% more than the leading edge (as can be clearly seen from the red area indicating the increased deflection).

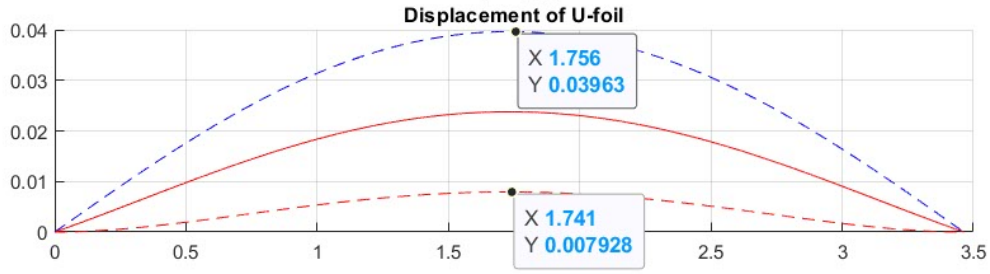

(a) Analytical deflection AISI 310SS U-foil: fixed 7.92mm, simply supported 39.63mm

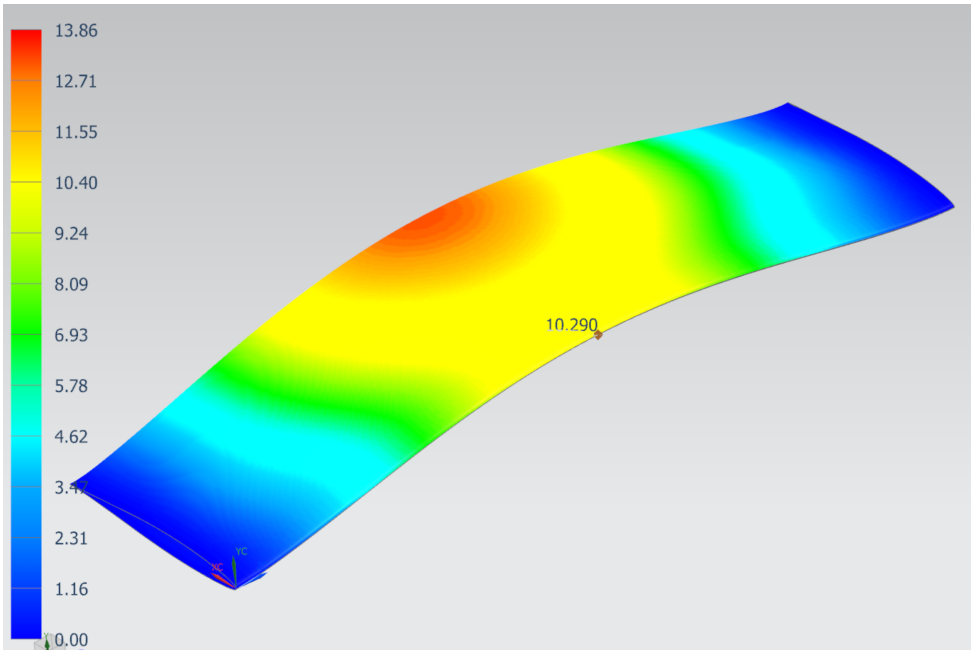

(b) FE deflection AISI 310SS fixed U-foil: 13.86mm

Figure 5.2: Difference in deflection results

When considering the simply supported condition for the same structure, the results closely match the expected deflection (40.96mm in FE against 39.63mm in MATLAB). The increased deflection on the trailing edge is still present, but at a much lesser magnitude than with the fixed condition.
To prevent warping, the simulation is done again after including the spars. Their contribution to the bending stiffness is limited, but the warping of the structure is significantly reduced (Figure 5.3) leading to better results, with FEM outperforming the tool.

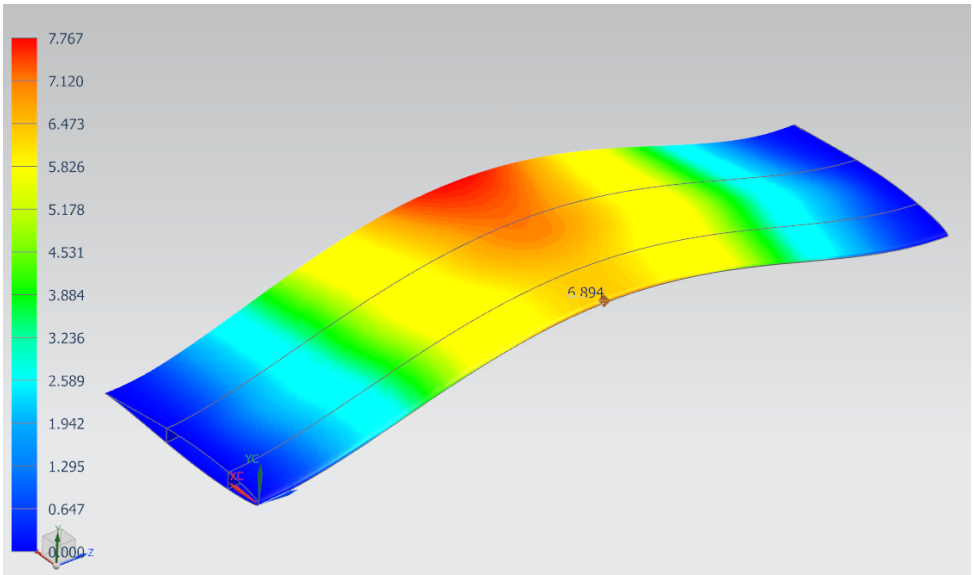

Figure 5.3: FEM deflection AISI 310SS fixed U-foil: 7.76mm

5.4.2 Composite results

Of the tested lay-ups, half of the resulting structures perform much worse in FE than expected. This is specifically the case for the combination of no taper and (relatively) low fractions of shear resistant reinforcement/high fractions of longitudinal reinforcement. The worst example of this is found in a purely longitudinal layup, which in the analytical model performs very well due to its high bending stiffness in the main bending direction, but in FEM performs poorly due to large distortions of the cross-section (Figure 5.4b). This leads to deflections up to four times larger than expected (270.77mm in FE against 77.78mm in the analytical model).

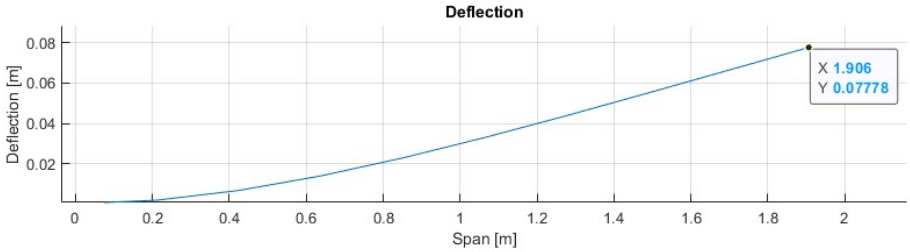

(a) Analytical result of $[0_6]$ cantilever box foil: 77.7mm

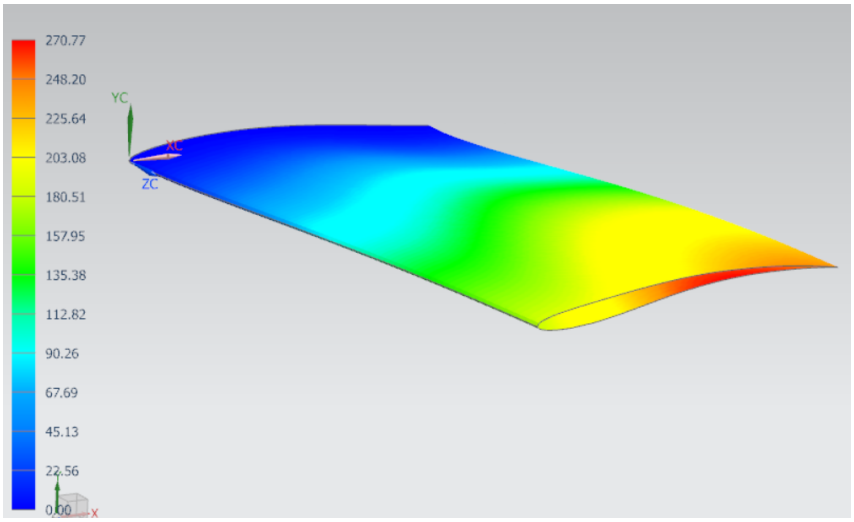

(b) FE deflection $[0_6]$ cantilever box foil: 270.77mm

Figure 5.4: Poor performance in FE of $[0_6]$ lay-up in untapered/boxwing foil

Including spars in the simulation reduces the distortion of the profile. Especially for composite laminate spars, the bending stiffness is barely increased as the [45/-45] lay-up does little to resist the bending of the foil. The relatively small area of the spars and their position close to the neutral line of the foil means that there is no noteworthy increase of the bending inertia. However, it has a large influence on the total deflection of the structure, as can be seen in Figure 5.5. This reduces the deflection error from 300% to within 10%.

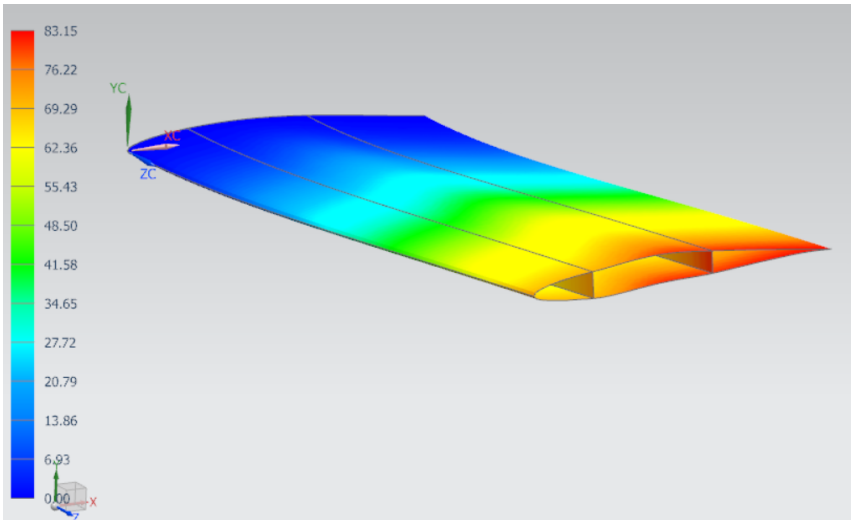

Figure 5.5: FE deflection $[0_6]$ cantilever box foil after adding [45/-45] spars: 83.15mm

The distortion and twisting is less pronounced in the tapered foils. The more the foil approximates a triangular shape, the less warping occurs and the more accurate the tool prediction is. Only the $[0_6]$ lay-up leads to very high error (193.9%) if no spars are included. Inclusion of spars reduces this error to 91.3% as warping still occurs. This is the only lay-up that retains the high error even after adding spars to a tapered foil.
The clamped FRP U-foils suffer from warping of the cross-section as well. The same distortion along the chord seen in Figure 5.2b is observed for FRP foils. This can again be reduced by adding the spars to the structure. In addition to the warping, the unsupported section between the spars deflects under the pressure load (Figure 5.6b), leading to a local deformation "ridge". This could potentially be solved by adding internal support or foil end plates. For validation purposes this is deemed not necessary, as increasing the complexity of the model will make comparing the results more difficult. Where a large local deformation is present, the leading edge deformation can be used as a good approximate of the global displacement. As can be seen when comparing the leading edge results to the analytical results of Figure 5.6a.

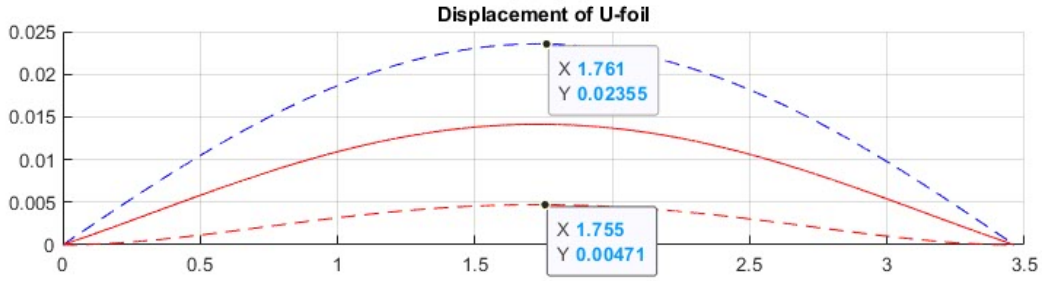

(a) MATLAB deflection of $[0_2/90/45/\text{-}45]_s$ clamped U-foil: 4.71mm

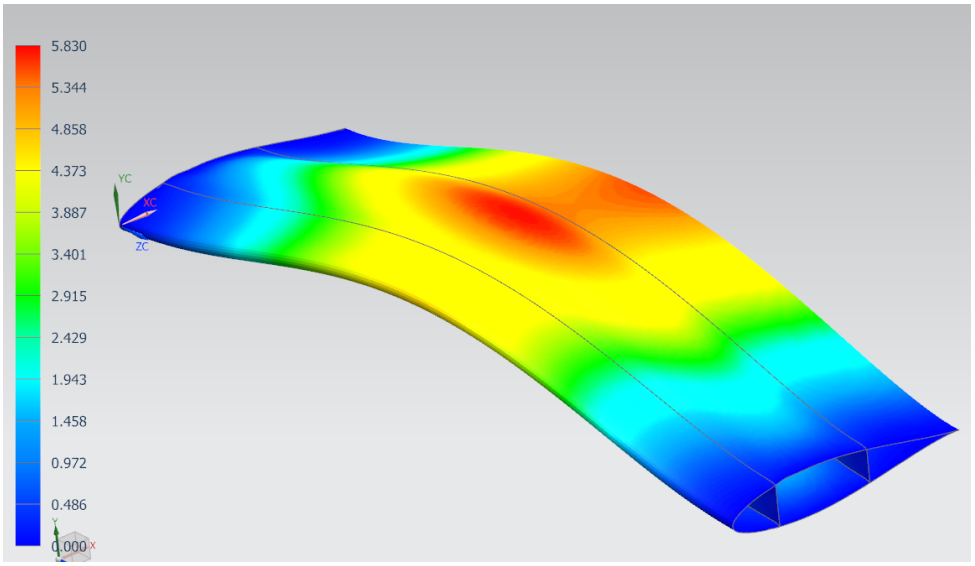

(b) FE deflection of $[0_2/90/45/\text{-}45]_s$ clamped U-foil after adding [45/-45] spars: 5.83mm, local deformation

Figure 5.6: Local deformation on U-foil

Stress and failure in FEM

A major difference between CLT and FE is the value of the maximum stress in the model. The analytical CLT based model does not take into account any stress concentrations. These can be caused either by the geometry or by the connections of the spar to the skin. It makes it difficult to verify failure of the material in FE. The stress results in FE are in the same order of magnitude as

predicted and often lower for skin-only models. For the majority of the results, the stresses in FE are lower, which is a positive indication for a conservative tool. Adding the spars improves deflection accuracy but the stress concentrations introduced by the line connection (Figure 5.7) make it difficult to quantitatively compare results.

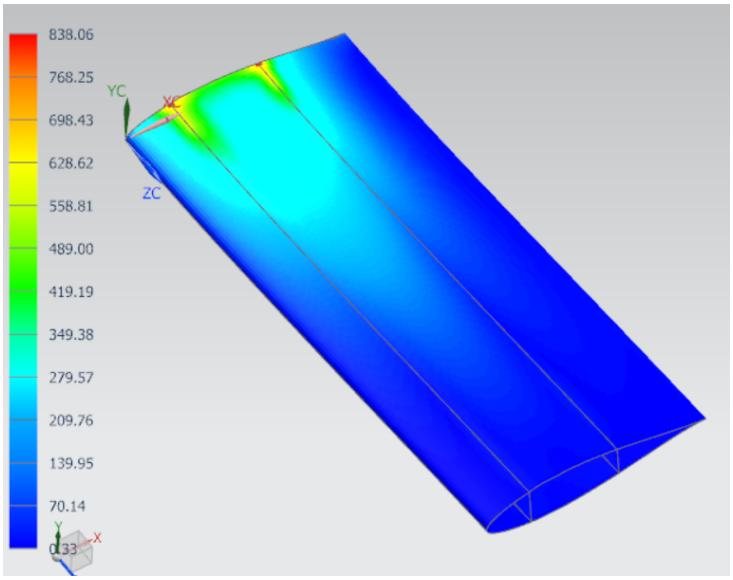

Figure 5.7: Stress concentrations at root (boundary condition) and spar connection line

Applicability

From the simulations of all the different foil types, profile sizes and lay-ups can be concluded that the analytical tool gives accurate and usable results for the preliminary design phase. Important lessons for the application of the tool to a case study are taken from this validation. The most important lesson is that the analytical tool will give conservative results as long as the spacing of the foil profile is maintained and the cross-section remains (relatively) unwarped. This is done by including the shear webbing in the model.
For composite structures, it was found to be critical to include reinforcement in all directions for the best results. High fractions of longitudinal reinforcement will lead to more distortion and poor results compared to the 2D estimations of the tool.

6 | Case Study

6.1 Introduction

The optimization tool is applied to two vessels for the Damen portfolio. Within the Design and Proposal department, particular interest is shown in two distinct use cases for hydrofoils: oceangoing fast ferries and small- to mid-sized fast crew suppliers. Both cases will give results in two very different weight classes. The knowledge gained from the validation is taken into account and a FE model of the entire 3D-structure is created. Stress concentrations make it impossible to compare local stresses to the analytical estimates but displacement values show promising accuracy, as long as internal support ribs are included to maintain proper skin spacing.

6.2 Case study vessels

The hydrofoil concept shows the most potential for high-speed transportation where comfort is of significant importance. Higher comfort at higher speed is one of the main objectives at the Damen Shipywards proposal group. Damen Shipyards has previously invested heavily towards this goal, implementing axe bows on fast crew suppliers bringing workers to offshore platforms. The potential fuel savings that could be achieved by the lower drag of a hydrofoil adds to strengthen the business case for hydrofoil vessels.

6.2.1 Crew Transfer proposal

An application for a smaller vessel is found in the Fast Crew Suppliers. These vessels come in a wide range of sizes, between 12 and 70 meters long. A mid-sized FCS is chosen as a suitable concept for hydrofoil application, shown in Figure 6.1. The FCS2206 is an aluminum monohull ship capable of carrying cargo and up to 42 passengers.

Property	Value
Beamwidth [m]	6
Length [m]	22
Displacement [t]	45
Draught [m]	1.5
Maximum speed [kn]	32

Figure 6.1: FCS 2206 [54] and properties

6.2.2 Fast ferry proposal

A heavier application is found in oceangoing fast ferries. The properties of a conceptual fast ferry are determined by taking the similar properties of an existing fast ferry in the Damen portfolio. The Damen Fast Ferry 4010 is chosen as a base for the design. The FF4010 is an aluminum twin-hull

(catamaran) type, mid sized vessel capable of transporting 450 passengers. The characteristics are shown in Figure 6.2:

Property	Value
Beamwidth [m]	10
Length [m]	40
Displacement [t]	175
Draught [m]	1.6
Maximum speed [kn]	36

Figure 6.2: DFFe 4010 [55] and properties

Fast Ferries in the Damen portfolio are typically catamaran ships. This means that loads are to be distributed over several smaller foils, as both hulls will likely have a foil at the front section of the ship. This could also possibly be two separate U-foils if loads prove too high for T-foils.
For the catamaran concept, only the rear foil is modelled. The rear foil in this case will likely be a tri-strut W-foil. It allows to demonstrate how the tool will deal with high-displacement vessels.

6.3 Results of analytical tool

The vessel properties of section 6.2 together with the values of table A.7 serve as an input for the optimization script to find an acceptable preliminary design. As the total 3D structure can not be modelled in MATLAB, a direct one-on-one quantitative comparison is not possible. Comparing the deflection results from MATLAB to the results of the total structure model can still give some relevant information on the usefulness and limits of the tool. The results from the application are found in appendix A.6, with the monohull front, monohull rear and catamaran rear structure in tables A.8, A.9 and A.10, respectively. Some of the main results are presented in this section. Stress values from FE are not practically usable due to stress concentrations in the 3D model. Transverse internal ribs have been added at the roots of the foils to prevent high levels of warping. As they have the same lay-up as the spars while being perpendicular to the beam, their direct contribution to the bending stiffness is negligible.

6.3.1 Isotropic results

When considering the front T-foil, the isotropic model still very closely follows the predictions from MATLAB. The found skin thicknesses are 10.8mm for the foil and 16.2mm for the strut. The deflection found in MATLAB for this structure is given in Figure 6.3a. Due to the lateral lift load on and the subsequent rotation of the strut, the absolute displacement on one side is higher than on the other. The total vertical displacement of the foils is more due to the shortening of the strut (caused by sideways deflection). The average displacement of two sides in the FE model (Figure 6.3b) gives an approximation of the deflection of the foil without the rotation. From the figure can be seen that MATLAB predicts 24.08mm while the average displacement from FE is 26.73mm. The analytical prediction is 9.9% lower than the FE result.

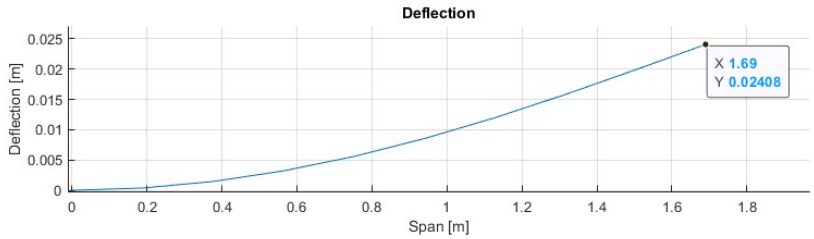

(a) Analytical deflection result metal front T-foil: 24.08mm

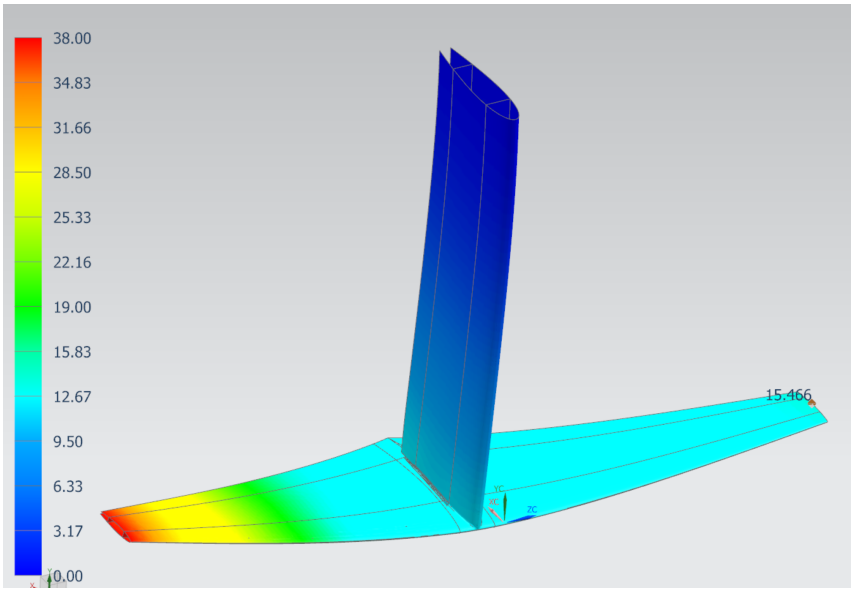

(b) FEM deflection results, average of 38mm and 15.46mm: 26.73mm

Figure 6.3: Front monohull isotropic results

When comparing the results of the aft U-foil, the displacement is highly accurate. The analytical model considers two boundary conditions, while in reality the boundary conditions would be somewhere between simply supported and fully fixed.

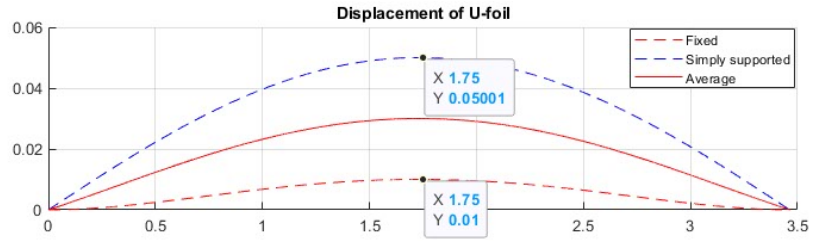

Figure 6.4: Analytical deflection result metal rear U-foil: 50.01mm (SS) and 10mm(F), average 30mm

The value from FE seen in Figure 6.5a lies between the two extremes predicted by MATLAB. The value of 17.81mm is closer to the 2D fixed boundary condition result. Very little geometrical distortion is seen in the FE model and there was no need to include transverse ribs in the structure to maintain proper spacing of the skins. The skin thicknesses are 13.5mm for both strut and foil.

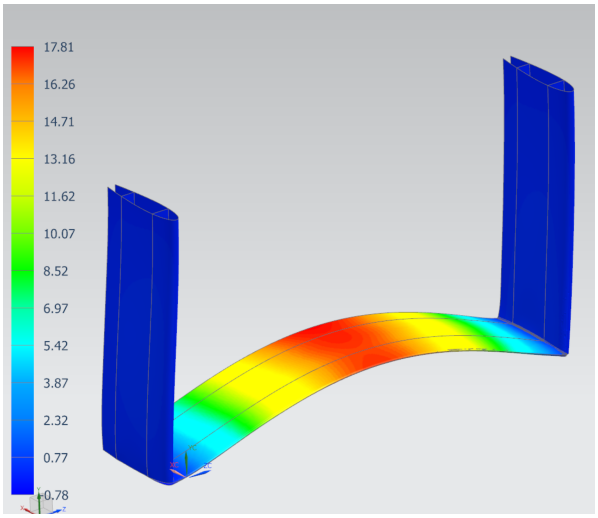

(a) FE deflection results metal U-foil: 17.81mm

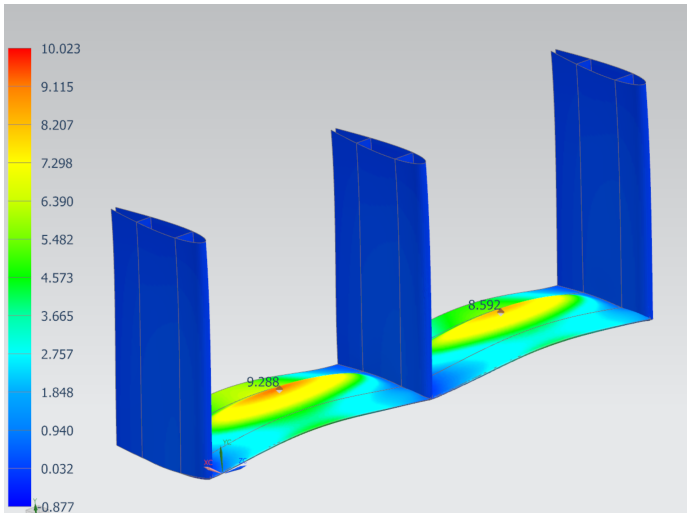

(b) FE deflection results metal W-foil: 9.29mm, LE 5.48mm

Figure 6.5: FE deflection results metal rear foils

For the ferry case study, only the rear foil is considered as this is a unique geometry with an extra strut. The analytical solution is shown in Figure 6.6. From the results can be seen that overall, for most sections of the W-foil, deflection is withing the 6 to 10mm range, which corresponds to the analytical estimations. However, the results for this analysis lean more towards the simply supported estimations. The midsections of the foils, between the spars where the load is defined, show significantly more deformation. As the structure is notably larger for W-foils, the unsupported area between the spars deflects on its own, adding to the total deflection, as seen in Figure 6.5b. The leading edge shows a more expected deformation pattern, with a displacement of 5.48mm. This is close to the average of 6.19mm of the simply supported (10.32mm) and fixed (2.06mm) analytical results. The difference with the analytical average is 11.47%.

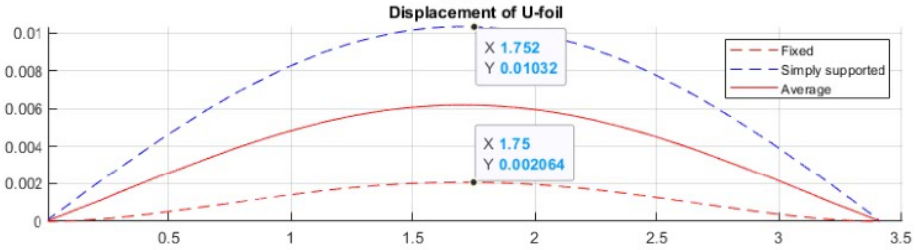

Figure 6.6: Analytical result metal W-foil: 10.32mm(SS), 2.06mm(F), average 6.19mm

6.3.2 FRP results

Similar to the validation models, the final structure composite model also shows severe warping for lay-ups containing higher fractions of longitudinal reinforcement. The warping is worsened as the root of the foils is no longer fixed, causing this point to be distorted the most. This problem is partially solved by including a single transverse rib a the root of the foils, ensuring proper spacing between the upper and lower skin of the foils. Despite these adverse effects, the results for the front foil match well. In Figure 6.7 can be seen that the difference between the 2D tool estimation of 74.93mm and the average FE deflection of 82.14mm is 8.76%.

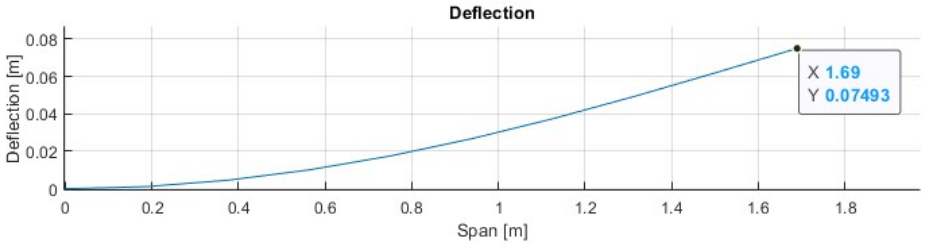

(a) Analytical deflection result FRP front T-foil: 74.93mm

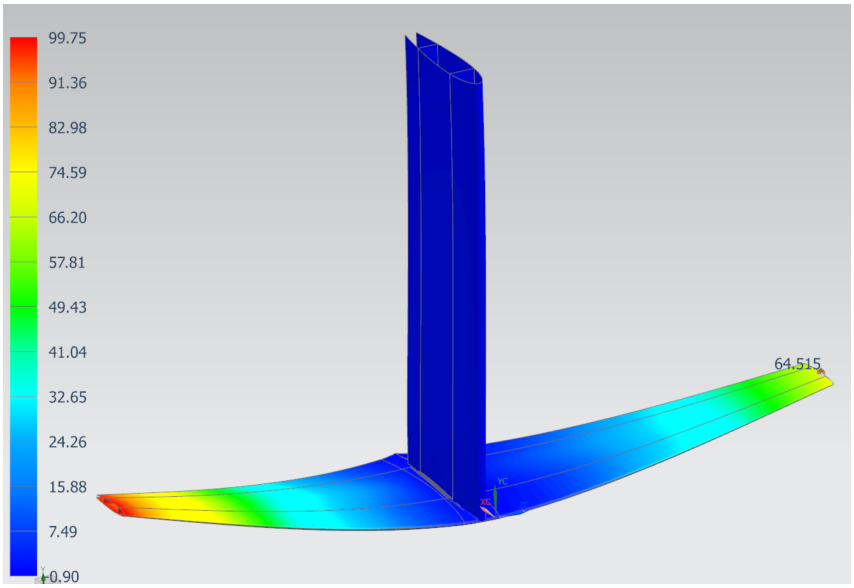

(b) FEM deflection results, average of 64.52mm and 99.75mm: 82.14mm

Figure 6.7: Front monohull FRP results

The analytical results for the rear FRP U-foil are shown in Figure 6.8.

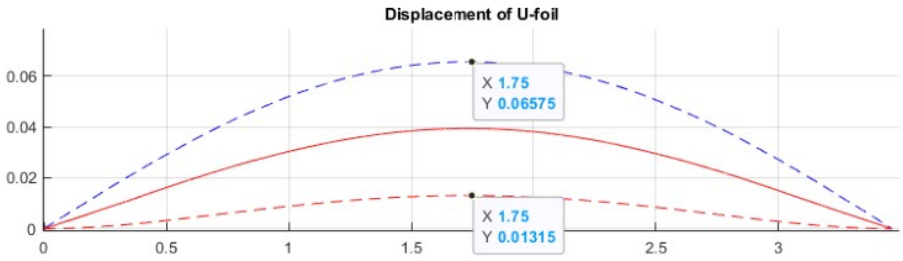

Figure 6.8: Analytical deflection result FRP rear U-foil: 65.75mm (SS) and 13.15mm(F), average 39.45mm

While the FEM results fall within the limits of the simply supported and fixed analytical outputs, they lean more towards the simply supported solution. With a FEM displacement of 47.24mm, the 2D solution is 19.8% smaller at 39.45mm.

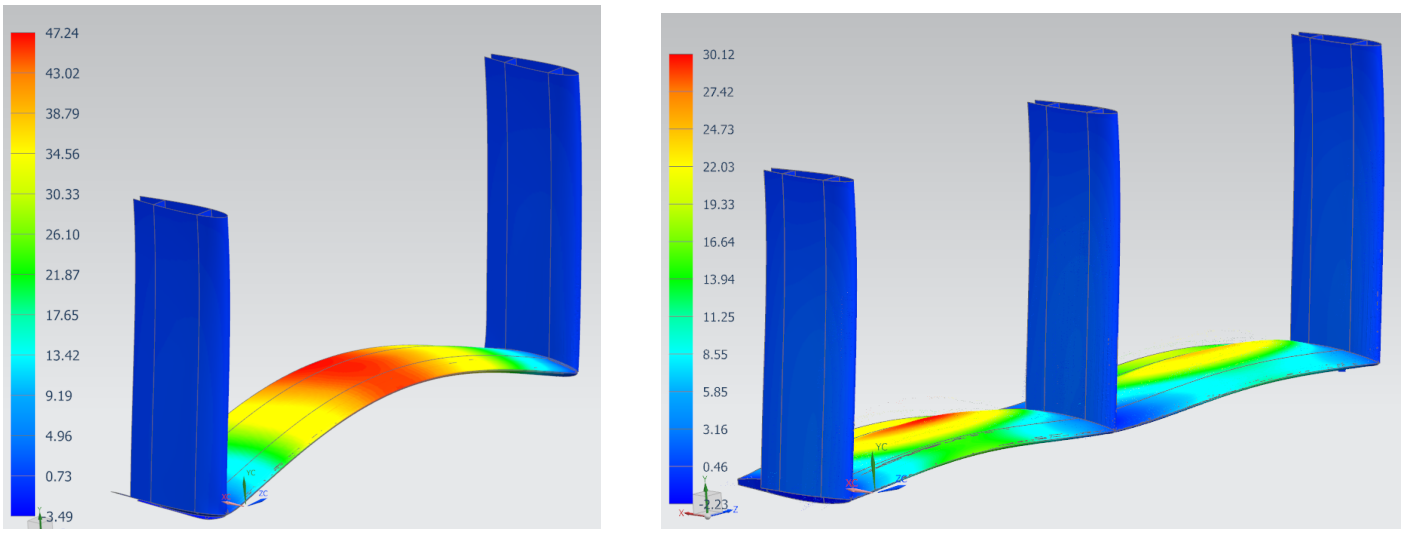

(a) FE deflection results: 47.24mm (b) FE deflection results: 30.12mm, LE 16.64mm

Figure 6.9: Rear monohull FRP results

Finally, the FRP W-foils are analyzed. Similar to the isotropic results, more deformation is seen on the plates between the spars. This effect is more pronounced for the FRP foils, as the total deflection tends to be more as well. The maximum displacement found in FE, seen in Figure 6.9b as 30.12mm, is larger than the maximum simply supported result found in Figure 6.10, 26.23mm. The difference is 14.8% to the simply supported value and 91.4% to the analyical average of 15.76mm. Looking at just the leading edge, and not taking into account the center plate deformation, the deflection is well within the analytical limits at 16.64mm, which is only 5.7% above the analytical average.

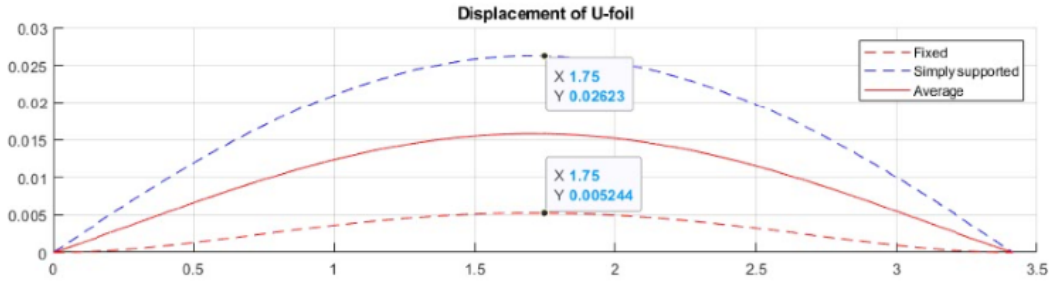

Figure 6.10: Analytical deflection result metal rear W-foil: 26.23mm(SS) and 5.24mm(F), average 15.76mm

7 | Discussion

7.1 Applicability of the tool

7.1.1 Accuracy in validation

From the validation of the tool using FE can be concluded that the tool does not always give perfect results. Due to the cumulative error of several assumptions in 2D analytical analysis, such as the tapered beam discretization, 3D finite element solutions do not always converge with the solutions from the tool. For reasons discussed previously in section 5.4, there are certain conditions for which the tool does not give reliable results. The caveat on using the tool is that the laminate must always contain reinforcement in both principal directions as well as for shear resistance. Beyond that, it is important to note that the numerical analysis of the structure including the spars almost always outperforms the analytical prediction. It is a positive note that the analytical tool is outperformed, as it means that the tool will provide a quick and conservative estimate. It does mean that at least for the deflection estimations, the tool may (significantly) exaggerate the displacement.
There is no hard limit on what would be considered an acceptably accurate solution. For this research, the limit was set at 10% error for the FE results. No strict requirements on the maximum error were put by Damen Shipyards.

7.1.2 Deflection

The tool iterates using the failure criteria to optimize the structure for minimal volume. Only considering whether or not the material anywhere in the structure might fail can lead to designs that work well on paper, but are unusable in reality. This is mainly because the structure may deflect too much for any practical application, without actually failing. This is especially the case for the composite structures, which tend to deflect more than their steel counterparts. For a lifting surface, deflection and twist can lead to a change in the loads, such as a loss of lift or increased drag. These hydro-structural interactions are too complex to include in the preliminary design tool. One way to deal with this limitation in a basic way, is to also include a deflection and/or twisting limit in the iteration loop. Further investigation would be needed to determine a suitable limit for the allowable deflection and consequent additional lift, but a comprehensive analysis of the hydro-structural interactions using CFD at a later stage would be most beneficial.
In itself, using the deflection as a measure for accuracy is not the optimal choice, as the design tool is more focused on failure than on deflection. Using the stress would be a better measure of the effectiveness of the tool, but this would require a much more detailed design and FE model to verify. The current simple initial design is not suitable for stress analysis using FE.

7.1.3 Stress

When looking at the resulting stresses in FE in the tables of appendix A.4 and the values of appendix A.6, immediately it can be seen that the resulting stresses are almost never in a similarly small error range as the deflection results. This is even more true for the case study results, as these models suffer from severe stress concentrations. The stress concentrations occur at the connections between the skins of strut/foil and the spar as well as around the connection of the foil to the strut. These effects can be mitigated by a more detailed design of the transition between parts. From a production-standpoint, this is vital as well, as sharp bends in FRP laminates are detrimental to their

strength. Possible design solutions are fillets and larger bonding areas, but these are design features that only come into play at a later design phase. However, some adjustments of the geometry is unlikely to lead to well matching stress results. Fundamentally, the 2D FRP result are based on a simplified model of the structure, as if it were a flat laminate plate. In reality, the structure is much more complex. The curvature may have an influence on how the stress is distributed (or concentrated) in the FE model. The stress results for the metal designs tend to be much closer.

7.1.4 Case study in FE

Overall, the total 3D structure in FE shows more displacement than the analytical estimation. Besides effects discussed in the section on validation (section 5.4), two additional effects are discussed here. Some deviations were to be expected, as the 3D FE model becomes increasingly complex and deviates more from the underlying 2D assumptions.

Boundary conditions

Taking the step from single 2D beams to a 3D structure consisting of several beams is bound to lead to some differences in results. The foils in the 3D structure model no longer have a fixed boundary condition at the root. This allows for distortion of the root cross-section as well as rotations at this point, which have a large effect on the free end of the beam. Especially for composite structures with more longitudinal reinforcement, the distortion of the root cross-section has a serious impact on the deformation.
To mitigate the effects on the total structure, transverse ribs can be added to the root of the foils. Adding transverse ribs can serve to maintain the proper cross-sectional geometry, leading to results much closer to the analytical estimations, despite not adding any bending inertia. The necessity of adding ribs did not show in the initial validation models as the unsupported plate length was much shorter, with fixed boundary conditions at the edges constraining any distortion of the cross-section. A comparison has been included in the appendix, showing the distortion in at the root of the foil (Figure A.6). These transverse ribs were added to all models, but their influence was mostly noticeable for T- and W-foils, as these suffered badly from root distortions.

Trailing edge device

A minor difference between the validation and the total model is the inclusion of the trailing edge lifting devices. As soon as the trailing edge is not a closed loop, FE will allow for separate distortion of the sections behind the torsion box (visible in Figure A.6). In MATLAB, the cross-section will remain constant even if the section is open at the rear. As this is not the case in FE, the rear section will contribute less to the total stiffness than calculated analytically.

7.2 Material

7.2.1 Structural dimensions

FRP structures have an advantage in production and design flexibility. As the laminae are inherently compliant before curing, curved surfaces can be created with relative ease. For the high weight application, the steel struts require thicknesses of 31.5mm to deal with the compressive loads. These are very thick steel plates, which would need to be fabricated in a slender hydrodynamic shape. This is much more difficult to achieve than with the compliant fibers (which require only a 21mm thick laminate in this particular case). As this research is not aimed at designing a real hydrofoil for a ship, this is not relevant for any conclusions on the effectiveness of the tool, but it is an important consideration for the application going forward.

7.2.2 Cost comparison

For both steel and composite structures, the volume is determined. In general, the steel structures have slightly smaller volume. The price per unit volume for the two materials considered is quite similar. From a material cost standpoint it makes little difference whether composites or steel is used, especially compared to the total cost of a ship. However, steel will weigh significantly more for the same volume and over its entire life-cycle, corrosion-related maintenance costs of steel may far exceed the small production cost-advantage of the material. These are just preliminary conclusions, as a proper comparison between the costs needs to take the total manufacturing costs into account.

7.3 Optimization

The tool applies only a simple optimization routine. Literature has shown much more advanced methods, but often these are computationally intensive and/or slow. As Damen Shipyards is looking for a fast design tool for initial conceptual design, these methods were deemed far too complex and intensive. The output of the tool could serve as a starting point for the design, which can then be further optimized in FE/CFD software using more advanced algorithms. Combining the tool with an advanced optimization algorithm could further improve the result.

7.3.1 Geometrical optimization

The analytical tool is a first step towards automated optimization of hydrofoil design. The tool follows a simple loop that goes from the smallest influence (increasing skin thickness) through medium influence (increasing chord) to the most influential (change hydrodynamic NACA profile) on bending stiffness and drag. This is a straightforward way to incrementally increase the strength of the structure up to the point where it just survives, but this is done only from a structural perspective. If no satisfactory results are found after increasing the chord length to the point where the foil thickness exceeds that of the next hydrodynamic profile thickness (section 4.2), the profile thickness will be increased. However, from a hydrodynamic point of view, it may be detrimental to performance to increase the NACA profile, as this will lead to more drag. There is a trade-off point between where a thinner profile with a longer chord generates more drag than a thicker profile with a shorter chord. This would be the best point to switch over, but in the current tool, this optimum point is not considered as hydrodynamic efficiency is not a priority. For proper optimization, the tool should be expanded to include this, but this requires either better integration of hydrodynamic profile data or a comprehensive CFD analysis of the design.

7.3.2 Lay-up/FRP optimization

One of the key strengths of using FRP as a structural material is the capability to tailor it to a specific loading condition. For the purpose of the initial design, lay-ups were chosen that would be better suited to the specific application than (quasi)isotropic material would be, based on 'best practices' in the aerospace industry. However, the laminate itself can also be optimized. This would add at least one extra variable to the optimization routine that would directly influence the other variables, increasing complexity. Improving the lay-up has to be done using FE, as the purely 2D analytical expressions in the tool are not suited for this. As the tool is based on 2D beam theory, the foil cross-section will remain constant even if the stiffness in the transverse direction would become zero. Clearly, this is an unrealistic representation of the behavior of FRP structures. Optimization with 3D structures in FE, taking into account (geometric) distortions, would give a much better result than using the tool.

8 | Conclusions and recommendations

8.1 Conclusion

This research aims to answer the question *'How can an optimization design tool be used to guide the development of a Fiber Reinforced Polymer hydrofoil?'*
The main research question can be answered by first considering subquestions, which are recalled here:

1. How can a fast preliminary design tool based on analytical expressions be developed?
   (a) What is the current state of the art?
   (b) What are the main loads on a hydrofoil?
   (c) How can the loads be translated to stresses in a laminate structure?
2. Can the analytical results from the optimization tool be verified?
3. Can the applicability of the tool be demonstrated in a case study?

From the initial investigation into existing hydrofoil structures, the fully submerged hydrofoils were identified as the most relevant type for the intended application, due to superior comfort and better seakeeping performance. Different configurations were considered, each with their own specific use case. These were included in the analytical tool to ensure its applicability for a wide range of vessels. The state of the art for optimization algorithms was investigated, but existing solutions were considered to be too computationally intensive and complex for the application in a fast preliminary design tool. Iterating over single variables in succession rather than (interdependent) multi-variable optimization was chosen as an acceptable solution for an initial design tool, acknowledging that more efficient optimization is possible at the cost of computational power and time.

The static hydrodynamic loads on the structure were identified and modelled in a parametric design tool using MATLAB. The loads on the structure during a turn with sideslip, including additional lift due to deflected trailing edge devices, were considered as the worst-case loading scenario. Buckling of the strut was found to be the critical factor in determining the size of the struts. Classical Laminate Theory was implemented to model the FRP structure, using Tsai-Hill as the failure theory, including safety factors calculated from shipbuilding classification rules for Carbon FRP. This allowed for evaluation of the stresses in the laminate. Optimization was applied to the size and thickness of the structure, but not to the lay-up of the laminates as the analytical model was not deemed suitable to perform this optimization. As the tool is based on 2D beam theory, fundamentally it is not capable of taking distortions of the cross-section into account. It would consider purely longitudinal UD reinforcement as optimal.

In order to ensure that the analytical solutions are a usable starting point for the design, the optimization tool was verified. Using Finite Elements (FE) was considered the most efficient, low-cost option. The 2D solutions were approximated in FE as closely as possible by initially verifying the different elements separately, by modelling the parts as cantilever or fixed beams. The deflection and maximum stress were used as the outputs to compare quantitatively. 3D effects were unavoidable in FE, leading to worse than expected performance for the numerical model due to distortion of

the cross-section not present in the design tool. For isotropic and quasi-isotropic structures, the FE deflection results did not exceed the 2D estimations by more than 10% for almost all cases except fixed U-foils. In most cases, FE results outperformed the analytical results, meaning that the tool gives a conservative design.
Foils with high fractions of longitudinal reinforcement displayed significant warping in FE leading to higher displacements, in some cases orders of magnitude higher than analytically calculated. Inclusion of the spars to maintain a more or less constant cross-section without adding much bending stiffness resulted in much more accurate results, in some cases reducing error by 91%. The validation led to limitations on the applicability of the tool, requiring reinforcement in the two principal directions as well as against shear deformation to be present for accurate results. While deflection results were accurate, stress results could not be matched one-to-one with the design tool both due to stress concentrations occurring at the connections of the structure in FE and simplifications of the structure in the analytical model.

Finally, the design tool was applied to two vessels with different weight classes as a case study. The resulting structural foil designs were modelled in FE in their entirety. The total deflection results of the structure were compared to what the design tool predicted on a component level. For steel designs, the FE deflection results for the monohull front and rear designs were 9.9% and 11.47% above the analytical values, respectively. For the FRP designs, this was 8.76% and 19.8%. For foils with more than one strut, the results were compared to the average, but the FE displacements were always smaller than the predicted simply supported deflections. For the high displacement FRP design, additional local deformation of unsupported plates was found as the cause for the increased deformation. Disregarding local deformation, the FE results were 5.7% higher than the analytical estimate. Iteratively generating the complete structural designs using the tool was done in a manner of minutes. In the FE analysis, the lack of boundary conditions at the root of the foil sections led to a newly identified requirement of transverse internal support ribs at the root to prevent distortion of the geometry, as well as the need for support ribs in the large unsupported sections of high displacement designs.

This leads to an overall conclusion that the optimization design tool can be used effectively to quickly create an initial hydrofoil structural design. With the limitations of beam theory and classical laminate theory in mind, it can be used to optimize the geometry of the structure iteratively for a given reinforcement stacking sequence. The tool allows for the fast estimation of size, hydrodynamic properties and deformation for both traditional isotropic materials as well as FRP structures, with minor deviations in displacement compared to numerical simulations. Stress results from the concept simulation could not be compared because of stress concentrations and the simplified definition of the analytical foil.

8.2 Recommendations

Based on the conclusions and the initial goals of the research, some recommendations for further refinement of the tool are made.

Optimization in the analytical tool was limited to geometric properties. This single-variable minimization is not true optimization, as the stacking sequence of the plies in the laminates was kept constant. Optimization of the lay-up for the specific loading conditions could further improve the results of the tool. This should be done in a 3D model, as the deformation of the foil cross-section has to be taken into consideration. Limiting the distortion of the foil shape is an important parameter as this directly influences the hydrodynamic performance (and the efficiency of the entire system with it). Further optimization could be achieved by including hydrodynamic foil shape optimization.

Optimization applied in industry shows potential to be combined with the fast analytical tool. The initial design can be quickly drafted, after which a computationally heavy optimization technique can be applied to refine the design.

The analytical model can be improved with better estimations of the load distribution. The hydrodynamic loads are currently based on the coefficients taken from 2D foil theory. Inclusion of 3D-effects in determining the loads will lead to a more realistic output. Spanwise pressure distributions of a given wing, taken from CFD simulations, can be implemented in the tool to give a better estimation of the local loads.

The FEM simulation of the foil can be improved by using a more realistic pressure distribution along the chord. Uniform pressure on the area between the spars is a direct translation of the 2D beam theory model, but in reality the load distribution will be non-uniform in the chordwise direction. Including this in the FE model will add the pitching moment and subsequent torsion shear stress to the foil. The analytical model does account for this extra stress, but this added load was not included in the FE model. It is recommended to use the pressure distribution for the chosen foil profile, that can be taken from XFOIL or CFD, in FE to accurately model the effects of twisting of the foils in the total structure.

Further improvement of the validation of the tool can be achieved through a FE model that is less hindered by stress concentrations. Validation of the stress-results is heavily influenced by stress concentrations occurring at the connection between the different elements. This makes it more difficult to compare the results with the analytical solution. Better verification can be done if a more detailed design is made and validated using FE, taking into account a better/more realistic geometry including fillets and larger connection surfaces between spars and skins. This allows for verification of failure behaviour using FE, which would be a second parameter to gauge the performance of the tool and improve confidence in the results.

Initial validation of the basic blocks of the tool using FE shows promising results in terms of accuracy of the tool. The next step would be to experimentally verify these results. This requires coupon testing of the intended material to get the best possible input for the tool, as well as a choice for the method of fabrication. Comparing the results of testing a physical prototype with the analytical estimations/FE results can help increase the confidence in the design procedure.

Bibliography

[1] "Jetfoil picture." [Online]. Available: http://atvyyc.net/wp-content/uploads/2020/04/turbojet-ferry.jpg

[2] "Damen FCS7011." [Online]. Available: https://res.cloudinary.com/damen-shipyards2/image/upload/v1633591608/DAMEN/News/2021/10/damen-revolutionary-fcs-7011-completes-sea-trials-and-heads-to-the-netherlands/fcs-7011-aqua-helix-preview.png

[3] "The U.S. Navy Has Unveiled A New Hydrofoil, Its First In Decades." [Online]. Available: https://www.thedrive.com/the-war-zone/27350/the-u-s-navy-has-unveiled-a-new-hydrofoil-its-first-in-decades

[4] V. Ruggiero and F. Morace, "Methodology to study the comfort implementation for a new generation of hydrofoils," *International Journal on Interactive Design and Manufacturing (IJIDeM)*, 2008. [Online]. Available: https://doi.org/10.1007/s12008-018-0511-7

[5] "AC75 - 36th America's Cup." [Online]. Available: https://www.americascup.com/the-technology

[6] "Passenger Ferry - Artemis Technologies." [Online]. Available: https://www.artemistechnologies.co.uk/projects/820-2/

[7] A. Phillips, A. W. Phillips, A. Nanayakkara, S. Russo, R. Cairns, and N. St John, "Mechanical response of a thick composite hydrofoil." [Online]. Available: https://www.researchgate.net/publication/282697189

[8] Y. Liang and A. Bliault, *High Performance Marine Vessels*. Springer, 2012.

[9] "Foilcat Ferry picture." [Online]. Available: https://www.turbojet.com.hk/en/vessel-information/foilcat.aspx

[10] O. Faltinsen, *Hydrodynamics of high-speed marine vehicles*. Cambridge university press, 2005.

[11] "International Hydrofoil Society, Newsletter 1," 1994.

[12] Unknown, "Advanced Marine Vehicles lecture notes, Hydrofoils."

[13] R. J. Johnston, "Hydrofoils," *Naval Engineers Journal*, vol. 97, no. 2, pp. 142–199, 1985.

[14] C. B. Mckesson, *The Practical Design of Advanced Marine Vehicles*, 2009.

[15] "Split front foils." [Online]. Available: http://www.yachtboutique.com/images/A-foil3.jpg

[16] "Jetfoil render." [Online]. Available: https://images.ctfassets.net/r57nqja17dif/5HMStS4l9SmsGj0jKKILSz/5b6585c0c74fd86e88523e645b5616e5/00.jpg?w=580&q=85

[17] J. P. Gudas, "Survey of hydrofoil materials," Naval Ship Research and Development Laboratory, Annapolis, Tech. Rep., 1969.

[18] R. A. Shenoi and J. F. Wellicome, *Composite Materials in Maritime Structures*. Cambridge University Press, 2008, vol. 1.

[19] "AC75 Swing arm." [Online]. Available: https://resources.stuff.co.nz/content/dam/images/4/y/p/x/9/7/image.related.StuffLandscapeSixteenByNine.710x400.21n89y.png/1608233112366.jpg?format=pjpg&optimize=medium

[20] X. Wang, B. Song, P. Wang, and C. Sun, "Hydrofoil optimization of underwater glider using Free-Form Deformation and surrogate-based optimization," *International Journal of Naval Architecture and Ocean Engineering*, vol. 10, no. 6, pp. 730–740, 11 2018.

[21] E. Lund, "Discrete Material and Thickness Optimization of laminated composite structures including failure criteria," *Structural and Multidisciplinary Optimization*, vol. 57, no. 6, pp. 2357–2375, 6 2018.

[22] C. Bach, R. Jebari, A. Viti, and R. Hewson, "Composite stacking sequence optimization for aeroelastically tailored forward-swept wings," *Structural and Multidisciplinary Optimization*, vol. 55, no. 1, pp. 105–119, 1 2017.

[23] H. Ouyang, L. J. Weber, and A. J. Odgaard, "Design optimization of a two-dimensional hydrofoil by applying a genetic algorithm Design optimization of a two-dimensional hydrofoil by applying a genetic algorithm," vol. 38, no. 5, pp. 529–540, 2006. [Online]. Available: https://www.tandfonline.com/action/journalInformation?journalCode=geno20

[24] P. W. Aung, O. Tatarnikov, and N. L. Aung, "Structural optimization of a light aircraft composite wing," in *IOP Conference Series: Materials Science and Engineering*, vol. 709, no. 4. Institute of Physics Publishing, 1 2020.

[25] J. Chen, Q. Wang, W. Z. Shen, X. Pang, S. Li, and X. Guo, "Structural optimization study of composite wind turbine blade," *Materials and Design*, vol. 46, pp. 247–255, 4 2013.

[26] O. M. Querin, M. Victoria, C. Alonso, R. Ansola, and P. Martí, *Toplogy Design Methods for Structural Optimization*. Elsevier, 2017.

[27] T. Xinxing, G. Wenjie, S. Chao, and L. Xiaoyong, "Topology optimization of compliant adaptive wing leading edge with composite materials," 2014. [Online]. Available: http://dx.doi.org/10.1016/j.cja.2014.10.015

[28] H. Sasaki, H. Igarashi, and I. Member, "Topology Optimization Accelerated by Deep Learning," 2015. [Online]. Available: http://www.ieee.org/publications_standards/publications/rights/index.html

[29] J. Anderson and M. Bowden, *Introduction to flight*, 2005.

[30] M. Drela and H. Youngren, "XFOIL," 2000.

[31] G. S. Lloyd, "Rules for Classification and Construction I Ship Technology 3 Special Craft 1 High Speed Craft," Tech. Rep., 2012. [Online]. Available: www.gl-group.com

[32] S. De Lannoy, "Section Modulus and Bending Inertia of Wings," Tech. Rep., 2013.

[33] A. Bedford and K. M. Liechti, "Mechanics of Materials," 2020. [Online]. Available: http://link.springer.com/10.1007/978-3-030-22082-2

[34] "Review of Circular Shafts," Cairo University, Tech. Rep.

[35] W. Young and R. Budynas, *Roark's Formulas for Stress and Strain*, 7th ed. McGraw-Hill, 2002.

[36] No, "CLASSIFICATION NOTES BUCKLING STRENGTH ANALYSIS OF BARS AND FRAMES, AND SPHERICAL SHELLS," 2004. [Online]. Available: http://exchange.dnv.com.

[37] M. E. Lemonis, "Fixed Beam Calculator." [Online]. Available: https://calcresource.com/statics-fixed-beam.html

[38] "maxresdefault.jpg (1280×720)." [Online]. Available: https://i.ytimg.com/vi/J-WxuJdI0lk/maxresdefault.jpg

[39] Y. M. Han, W. B. Gu, Y. H. Hu, P. Prombut, and C. Anakpotchanakul, "Deflection of Composite Cantilever Beams with a Constant I-Cross Section."

[40] L. P. Kollar and G. S. Springer, *Mechanics of composite structures*. Cambridge ;: Cambridge University Press,, 2003.

[41] M. P. O'Donnell and P. M. Weaver, "Reconsidering Laminate Non-Symmetry," vol. 22, p. 26.

[42] A. Baker, S. Dutton, and D. Kelly, *Composite Materials for Aircraft Structures - Second Edition*, 2004.

[43] P. M. Weaver, "Designing composite structures: lay-up selection."

[44] D. Zenkert and M. Battley, *Foundations of Fibre Composites*, 2nd ed., 2003.

[45] "BV 600-NR 2021-06," 2021.

[46] A. K. Kaw, *Mechanics of Composite Materials*, 2nd ed., 2006.

[47] M. D. Hayes and J. J. Lesko, "Failure Analysis and Fatigue Life Prediction of a Composite Structural Beam," 2003.

[48] N. R. Mandal, "2: Ship Construction and Welding," in *Naval Architecture, Marine Engineering, Shipbuilding and Shipping*. Springer. [Online]. Available: http://www.springer.com/series/10523

[49] M. Hobbs and M. L. Mcewen, "Working Load to Break Load: Safety Factors in Composite Yacht Structures."

[50] Smith Metal, "UNS S32750 Super Duplex Technical Datasheet."

[51] Torayca, "M55J Technical Data Sheet."

[52] Siemens, "Nastran Element Library Reference Contents."

[53] Composites Group, "U20MM," 2004.

[54] Damen, "FAST CREW SUPPLIER 2206 EXECUTIVE SUMMARY."

[55] ——, "Product Sheet DFFe 4010," Tech. Rep. [Online]. Available: www.damen.com

A Appendix

A.1 Analytical tool outline

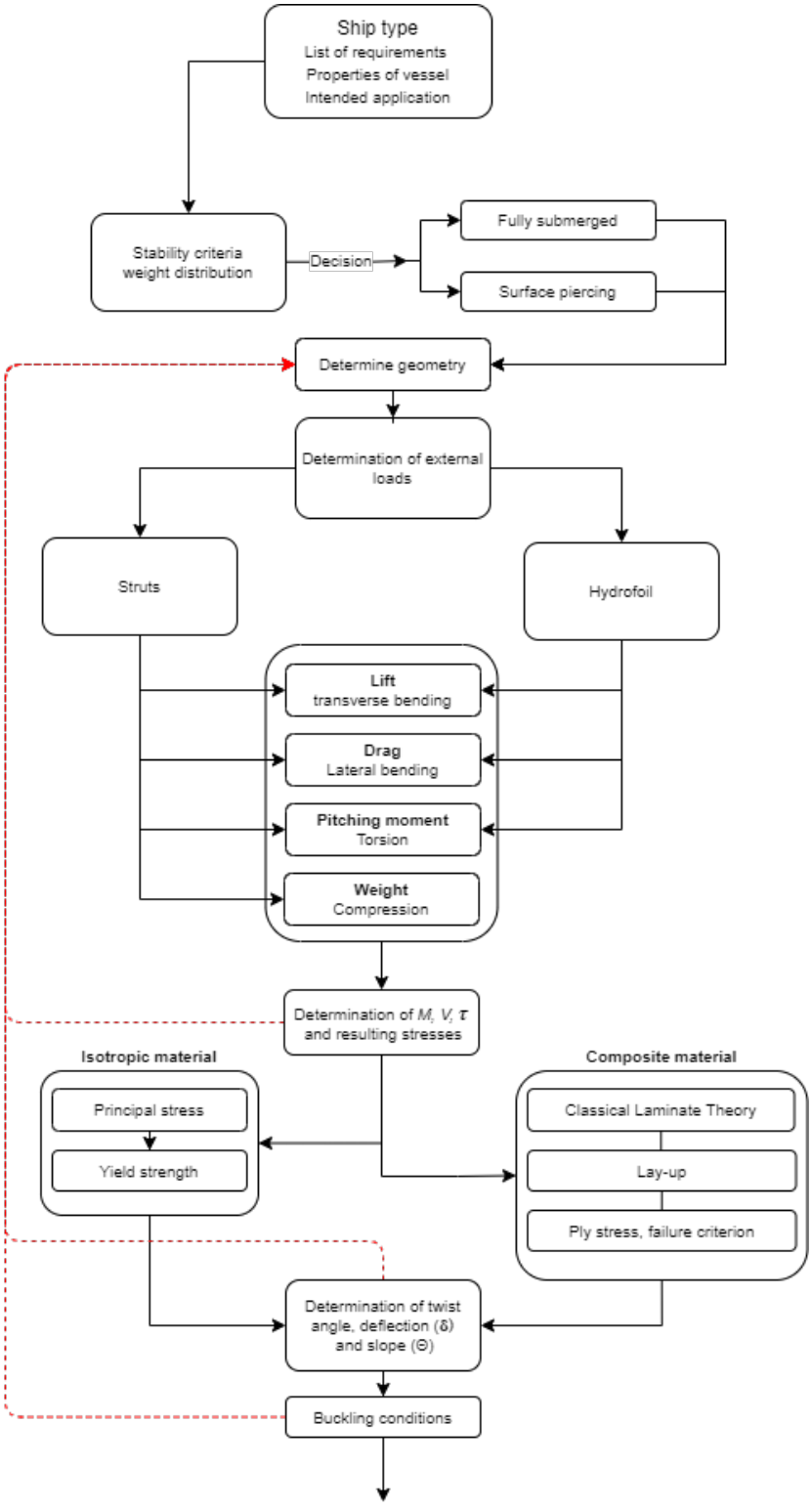

Figure A.1: Outline of steps

A.2 Analytical expressions

Analytical expressions [33, 37]. Meaning of symbols found in Figure 3.7a

A.2.1 Expression for prismatic cantilever beam under partial trapezoidal distributed load

$$R_A = L_w w_m \tag{A.1}$$

$$M_A = -\frac{2(3a + L_w)(L_w w_m) - L_w^2 w_2}{6} \tag{A.2}$$

$$\theta_A = 0 \tag{A.3}$$

$$\theta_B = \frac{-L_w((2a^2 + L_1^2)w_m + L_1 L_w w_2)}{12EI} \tag{A.4}$$

$$M_x = \begin{cases} R_A x + M_A & \text{for } x \leq a \\ R_A x + M_A - \frac{(2w_1 + (w_1 + \frac{(w_2 - w_1)}{L_w} \cdot (x-a)) \cdot (x-a)^2}{6} & \text{for } a < x < a + L_w \\ 0 & \text{for } x \geq a + L_w \end{cases} \tag{A.5}$$

The transverse shear load is given by:

$$V_x = \begin{cases} R_A & \text{for } x \leq a \\ R_A - \frac{(w_1 + (w_1 + \frac{(w_2 - w_1)}{L_w} \cdot (x-a)) \cdot (x-a)}{2} & \text{for } a < x < a + L_w \\ 0 & \text{for } x \geq a + L_w \end{cases} \tag{A.6}$$

The slope at any point x is given by:

$$\theta_x = \begin{cases} -\frac{R_A x^2}{2EI} + \frac{M_A x}{EI} & \text{for } x \leq a \\ -\frac{R_A x^2}{2EI} - \frac{M_A x}{EI} + \frac{(3w_1 + (w_1 + \frac{(w_2 - w_1)}{L_w} \cdot (x-a)) \cdot (x-a)^3}{24EI} & \text{for } a < x < a + L_w \\ -L_w \frac{(2a^2 + L_1^2)\frac{w_1 + w_2}{2} + (L + a - b)L_w w_2}{12EI} & \text{for } x \geq a + L_w \end{cases} \tag{A.7}$$

The deflection is given by:

$$\delta_x = \begin{cases} -\frac{R_A x^3}{6EI} - \frac{M_A x^2}{2EI} & \text{for } x \leq a \\ -\frac{R_A x^3}{6EI} - \frac{M_A x^2}{2EI} + \frac{(4w_1 + (w_1 + \frac{(w_2 - w_1)}{L_w} \cdot (x-a)) \cdot (x-a)^4}{120EI} & \text{for } a < x < a + L_w \\ -\frac{R_A (L-b)^3}{6EI} - \frac{M_A (L-b)^2}{2EI} + \frac{(4w_1 + w_2)L_w^4}{120EI} - \theta_B (x - (L-b)) & \text{for } x \geq a + L_w \end{cases} \tag{A.8}$$

A.2.2 Expressions for prismatic clamped beam under partial trapezoidal load

When considering two support struts, the foil is modelled as a clamped-clamped beam. The expression for the moment under a trapezoidal partial distributed load *w* is:

$$R_B = L_w w_m - \frac{L_w(ow_m + (p(w_2 - w_1))}{20L^3} \tag{A.9}$$

$$o = 10((L^2 + a^2)(L + a) + (a^2 + b^2)(a - b) - Lb(L + b) - a^3) \tag{A.10}$$

$$p = L_w(L(2L + a + b) - 3(a - b)^2 - 2ab) \tag{A.11}$$

$$R_A = L_w w_m - R_B \tag{A.12}$$

$$M_B = -\frac{L_w(qw_m + r(w_2 - w_1))}{120L^2} \tag{A.13}$$

$$q = 120ab(a + L_w) + 10L_w(6a^2 + 4LL_w - 3L_w^2) \tag{A.14}$$

$$r = 10LL_w^2 - 10L_w a(L - 3b) - 9L_w^3 \tag{A.15}$$

$$M_A = M_B + R_B L - aL_w w_m - \frac{(L_w^2(2w_2 + w_1))}{6} \tag{A.16}$$

$$\theta_A = \theta_B = 0 \tag{A.17}$$

$$M_x = \begin{cases} R_A x + M_A & \text{for } x \leq a \\ R_A x + M_A - \frac{(2w_1 + (w_1 + \frac{(w_2 - w_1)}{L_w} \cdot (x-a)) \cdot (x-a)^2}{6} & \text{for } a < x < a + L_w \\ M_B + R_B(L - x) & \text{for } x \geq a + L_w \end{cases} \tag{A.18}$$

The transverse shear is described by:

$$V_x = \begin{cases} R_A & \text{for } x \leq a \\ R_A - \frac{(w_1 + (w_1 + \frac{(w_2 - w_1)}{L_w} \cdot (x-a)) \cdot (x-a)}{2} & \text{for } a < x < a + L_w \\ -R_b & \text{for } x \geq a + L_w \end{cases} \tag{A.19}$$

The slope is given by

$$\theta_x = \begin{cases} -\frac{R_A x^2}{2EI} + \frac{M_A x}{EI} & \text{for } x \leq a \\ -\frac{R_A x^2}{2EI} - \frac{M_A x}{EI} + \frac{(3w_1 + (w_1 + \frac{(w_2 - w_1)}{L_w} \cdot (x-a)) \cdot (x-a)^3}{24EI} & \text{for } a < x < a + L_w \\ -\frac{R_B(L-x)^2}{2EI} - \frac{M_B(L-x)}{EI} & \text{for } x \geq a + L_w \end{cases} \tag{A.20}$$

$$\delta_x = \begin{cases} -\frac{R_A x^3}{6EI} - \frac{M_A x^2}{2EI} & \text{for } x \leq a \\ -\frac{R_A x^3}{6EI} - \frac{M_A x^2}{2EI} + \frac{(4w_1 + (w_1 + \frac{(w_2 - w_1)}{L_w} \cdot (x-a)) \cdot (x-a)^4}{120EI} & \text{for } a < x < a + L_w \\ -\frac{R_b(L-x)^3}{6EI} - \frac{M_B(L-x)^2}{2EI} & \text{for } x \geq a + L_w \end{cases} \tag{A.21}$$

A.2.3 Expressions for prismatic simply supported beam under partial trapezoidal load

Additionally, a simply supported beam is considered to prevent under-estimation of deflection:

$$R_A = L_w \frac{6w_m b + L_w(2w_1 + w_2)}{6L} \tag{A.22}$$

$$R_B = L_w \frac{6w_m(L-b) - L_w(2w_1 + w_2)}{6L} \tag{A.23}$$

$$M_A = M_B = 0 \tag{A.24}$$

$$\theta_A = -\frac{R_B L^2}{3EI} - \frac{L_w(sw_m + tw_2}{120EIL} \tag{A.25}$$

$$s = 20a^3 - 60a^2 L + 20L_w a(a-2L) + 10L_w^2(a-L) + 2L_w^3 \tag{A.26}$$

$$t = 10L_w a(a-2L) + 10L_w^2(a-L) + 3L_w^3 \tag{A.27}$$

$$\theta_B = \frac{R_B L^2}{6EI} - \frac{L_w(uw_m + vw_2)}{120EIL} \tag{A.28}$$

$$u = 20a^3 + 20L_w a^2 + 10Lw^2 a + 2L_w^3 \tag{A.29}$$

$$v = 10L_w a^2 + 10L_w^2 a + 3L_w^3 \tag{A.30}$$

$$M_x = \begin{cases} R_A x & \text{for } x \leq a \\ R_A x - \frac{(2w_1 + (w_1 + \frac{(w_2 - w_1)}{L_w} \cdot (x-a)) \cdot (x-a)^2}{6} & \text{for } a < x < a + L_w \\ R_B(L-x) & \text{for } x \geq a + L_w \end{cases} \tag{A.31}$$

The transverse shear is described by:

$$V_x = \begin{cases} R_A & \text{for } x \leq a \\ R_A - \frac{(w_1 + (w_1 + \frac{(w_2 - w_1)}{L_w} \cdot (x-a)) \cdot (x-a)}{2} & \text{for } a < x < a + L_w \\ -R_b & \text{for } x \geq a + L_w \end{cases} \tag{A.32}$$

The slope is given by

$$\theta_x = \begin{cases} \theta_A + \frac{R_A x^2}{2EI} & \text{for } x \leq a \\ \theta_A + \frac{R_A x^2}{2EI} - \frac{(3w_1 + (w_1 + \frac{(w_2 - w_1)}{L_w} \cdot (x-a)) \cdot (x-a)^3}{24EI} & \text{for } a < x < a + L_w \\ \theta_B - \frac{R_B(L-x)^2}{2EI} & \text{for } x \geq a + L_w \end{cases} \tag{A.33}$$

$$\delta_x = \begin{cases} -\frac{R_A x^3}{6EI} - \frac{M_A x^2}{2EI} & \text{for } x \leq a \\ -\frac{R_A x^3}{6EI} - \frac{M_A x^2}{2EI} + \frac{(4w_1 + (w_1 + \frac{(w_2 - w_1)}{L_w} \cdot (x-a)) \cdot (x-a)^4}{120EI} & \text{for } a < x < a + L_w \\ -\frac{R_b(L-x)^3}{6EI} - \frac{M_B(L-x)^2}{2EI} & \text{for } x \geq a + L_w \end{cases} \tag{A.34}$$

A.3 Material comparison using Granta Edupack

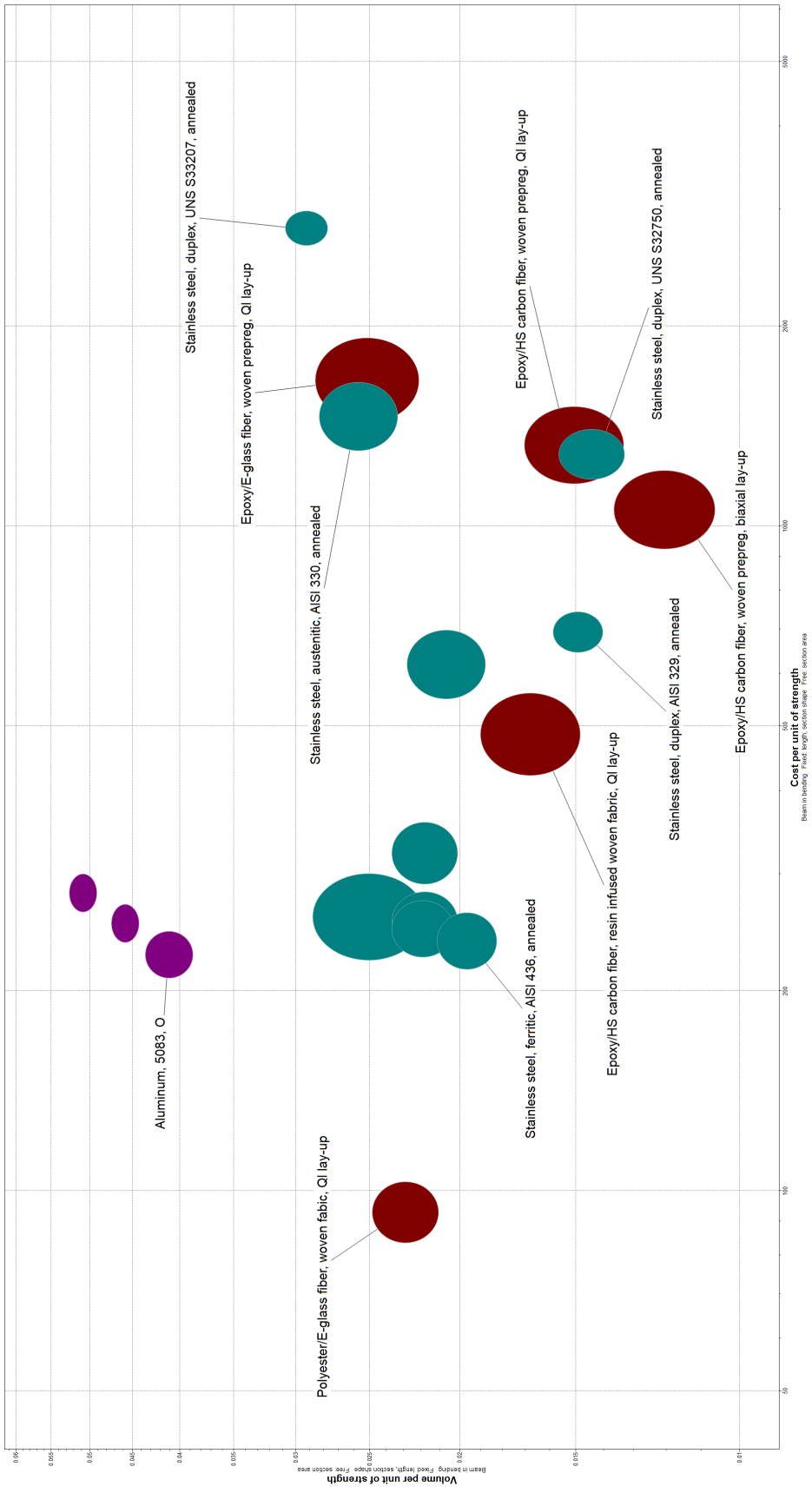

Figure A.2: Cost versus volume (per unit of strength)

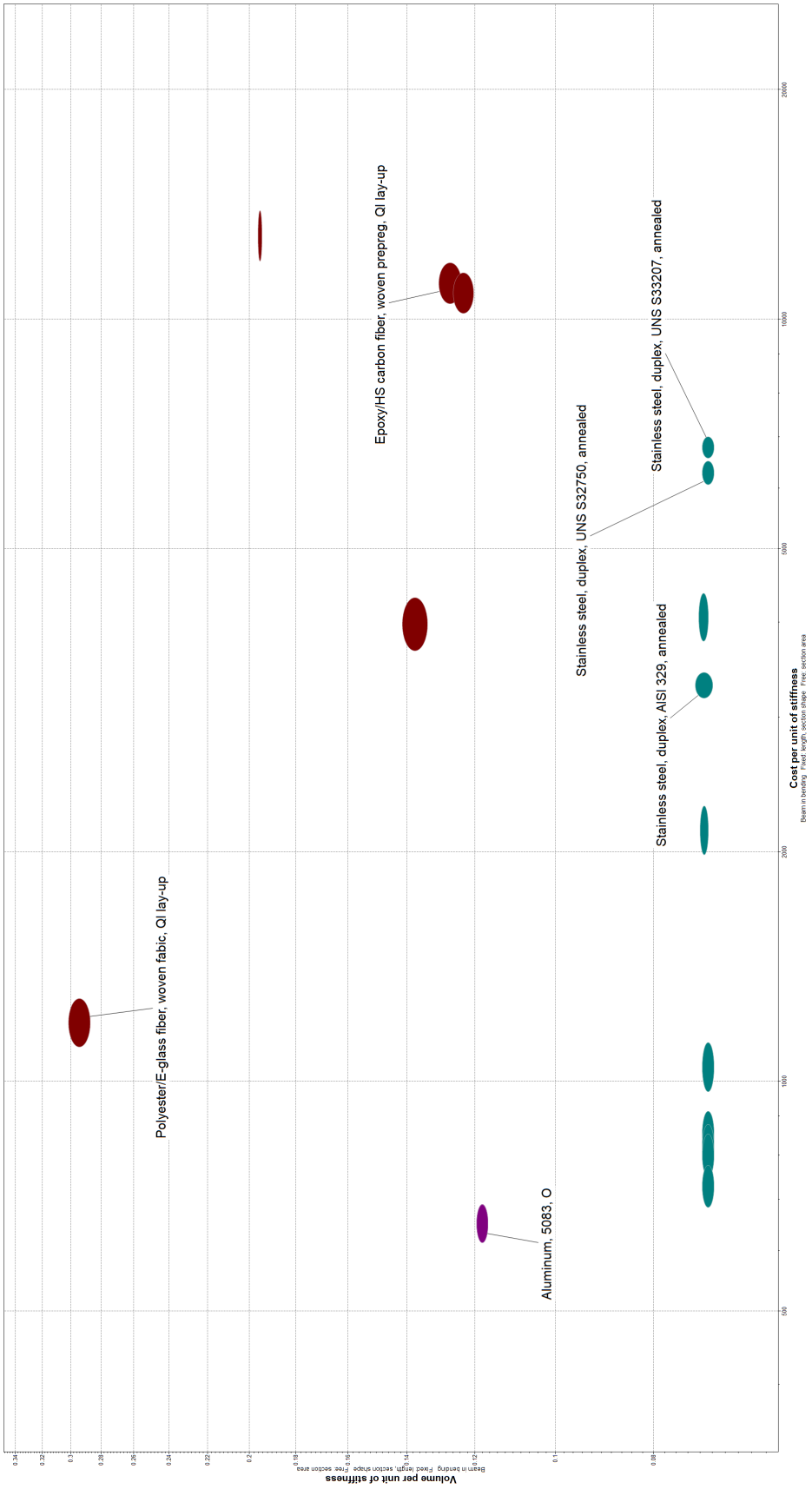

Figure A.3: Cost versus volume (per unit of stiffness)

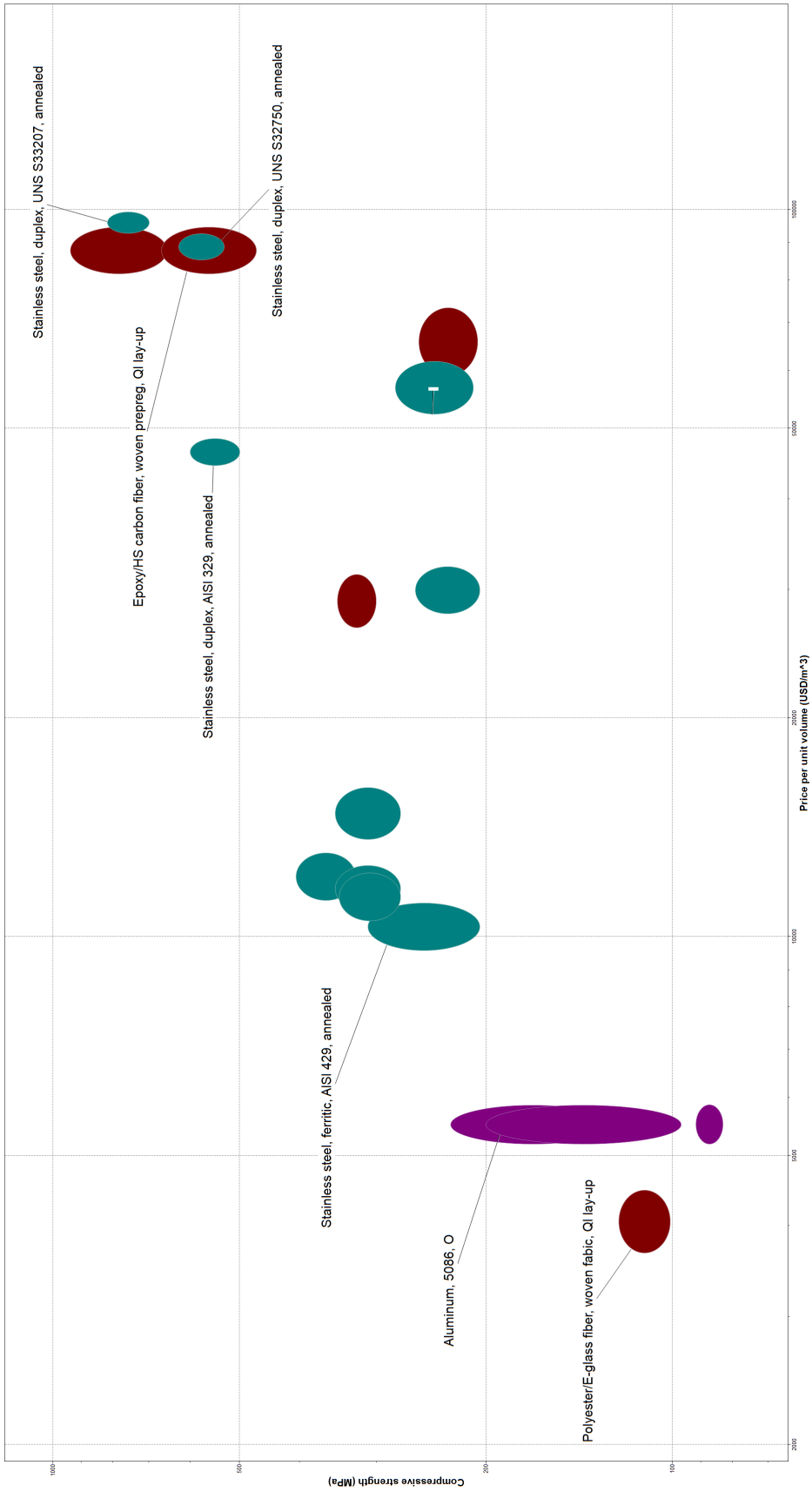

Figure A.4: Compressive strength versus cost

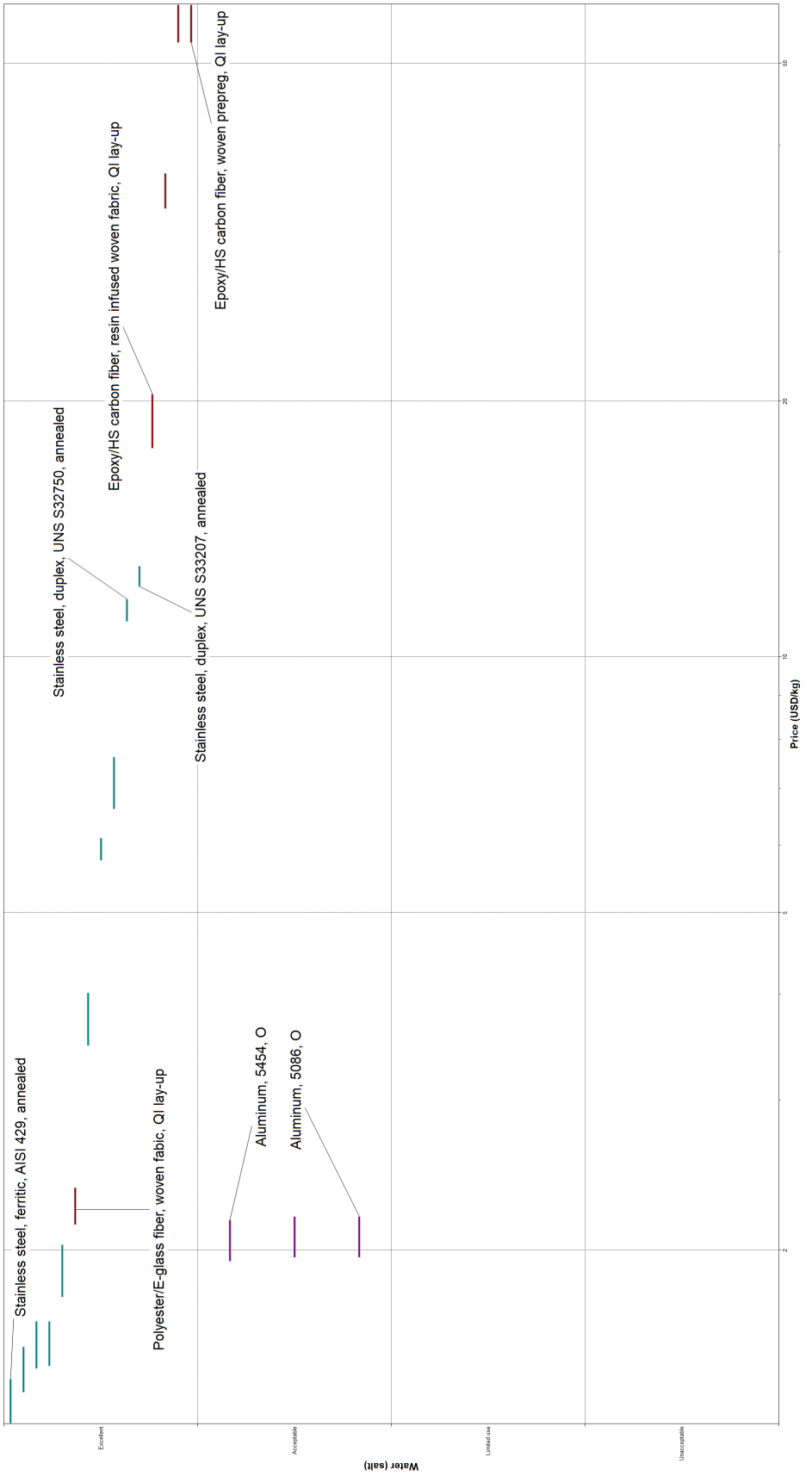

Figure A.5: Durability and cost

A.4 Validation of analytical tool

A.4.1 Validation of boxwing

No spars, 45.000kg displacement, single front T-foil, chord 762mm

NACA	t_{skin}	t_{web}	lay-up	δ_{NX}	$\delta_{NX,LE}$	δ_{ML}	$\Delta\%$	σ_{ML} [MPa]	σ_{NX} [MPa]
63218	22.5	22.5	$[0/90/45/\text{-}45]_{2s}$	19.82	18.17	24.8	-20.1/-26.7	267.3	156.05
63212	13.5	22.5	$[0/45/\text{-}45]_{2s}$	68.4	57.02	82.2	-16.8/-30.6	570.5	374.44
63218	13.5	18	$[45/\text{-}45]_{2s}$	119.9	119.9	160.4	-25.2	152.8	591.84
			$[0/90_5]_{2s}$						
63218	18	22.5	$[0/90]_{3s}$	41.66	31.5	20.3	104.9/55.1	215.1	317.18
63209	9	22.5	$[0_6]_s$	270.77	173.8	77.7	248.5/123.7	440.2	1031.22
63218	13.5	18	$[0_2/90/45/\text{-}45]_s$	35.04	31.4	26.3	33.2/19.4	271.2	286.7
63218	13.5	22.5	$[0_3/90/45/\text{-}45]_s$	36.78	32.9	22.41	64.1/46.8	233.7	293.18
63212	13.5	13.5	ISOTROPIC	22.66	22.54	26.71	-15.2/-15.6	301.5	315.71

Table A.1: Deflection and stress of front boxwing T-foil

Including spars, 45.000kg displacement, single front T-foil, chord 762mm

Additional simulation of warping foils, including shear webbing as internal structure.

NACA	t_{skin}	t_{web}	lay-up	δ_{NX}	$\delta_{NX,LE}$	δ_{ML}	$\Delta\%$	σ_{ML} [MPa]	σ_{NX} [MPa]
63218	22.5	22.5	$[0/90/45/\text{-}45]_{2s}$	16.79	16.38	24.8	-32.3/-33.9	267.3	345.09
63212	13.5	22.5	$[0/45/\text{-}45]_{2s}$	54.55	53.33	82.2	-33.6/-35.1	570.5	652.64
63218	13.5	18	$[45/\text{-}45]_{2s}$	85.37	84.34	160.4	-46.7/-47.4	152.8	1384.4
			$[0/90_5]_{2s}$						
63218	18	22.5	$[0/90]_{3s}$	18.57	17.02	20.3	-8.5/-16.2	215.1	339.81
63209	9	22.5	$[0_6]_s$	83.15	72.14	77.7	7/-7.2	440.2	567.45
63218	13.5	18	$[0_2/90/45/\text{-}45]_s$	27.64	27.15	26.3	5.1/3.2	271.2	417.8
63218	13.5	22.5	$[0_3/90/45/\text{-}45]_s$	28.17	27.51	22.41	25.7/22.8	233.7	405.98
63212	13.5	13.5	ISOTROPIC	18.83	18.03	26.71	-29.5/-32.5	301.5	306.01

Table A.2: Deflection and stress of front boxwing T-foil including spars

A.4.2 Validation of tapered wing

No spars, 45.000kg displacement, single front T-foil, root chord 1014mm

NACA	t_{skin}	t_{web}	lay-up	δ_{NX}	$\delta_{NX,LE}$	δ_{ML}	$\Delta\%$	σ_{ML} [MPa]	σ_{NX} [MPa]
63212	18	22.5	$[0/90/45/\text{-}45]_{2s}$	21.26	21.02	26.11	-18.6/-19.5	228.3	141.97
63209	6.75	15.75	$[0/45/\text{-}45]_{2s}$	103.13	96.5	87.2	18.3/10.6	453.3	375.79
63209	15.75	24.75	$[45/\text{-}45]_{2s}$	169.5	158.2	239.3	-29.2/-33.9	163.1	263.1
63218	20.25	18	$[0/90_5]_{2s}$	18.51	15.42	16.73	10.6/-7.8	225.9	136.25
63209	20.25	27	$[0/90]_{3s}$	38.74	27.75	31.6	22.6/-12.1	231.8	118.95
63209	6.75	15.75	$[0_6]_s$	100.8	76.5	34.3	193.9/123	196.4	729.99
63209	18	24.75	$[0_2/90/45/\text{-}45]_s$	28.57	28.57	35.83	-20.3	236.1	123.64
63209	13.5	22.5	$[0_3/90/45/\text{-}45]_s$	34.96	34.16	36.26	-3.5/-5.8	243.9	153.29
63209	9	9	ISOTROPIC	23.44	23.44	22.68	3.4	370.7	345.38

Table A.3: Deflection and stress of front tapered wing T-foil

Including spars, 45.000kg displacement, single front T-foil, root chord 1014mm

NACA	t_{skin}	t_{web}	lay-up	δ_{NX}	$\delta_{NX,LE}$	δ_{ML}	$\Delta\%$	σ_{ML} [MPa]	σ_{NX} [MPa]
63212	18	22.5	$[0/90/45/\text{-}45]_{2s}$	19.75	19.45	26.11	-24.4/-25.5	228.3	187.48
63209	6.75	15.75	$[0/45/\text{-}45]_{2s}$	84.33	84.06	87.2	-3.3/-3.6	453.3	574.73
63209	15.75	24.75	$[45/\text{-}45]_{2s}$	116.05	112.74	239.3	-51.5/-52.9	163.1	564.32
63218	20.25	18	$[0/90_5]_{2s}$	15.94	14.81	16.73	-4.7/ -11.5	225.9	210.2
63209	20.25	27	$[0/90]_{3s}$	29.88	26.09	31.6	-5.4/-17.4	231.8	198.47
63209	6.75	15.75	$[0_6]_s$	62.19	51.977	34.3	81.3/51.5	196.4	404.0
63209	18	24.75	$[0_2/90/45/\text{-}45]_s$	26.6	25.91	35.83	-25.7/-27.7	236.1	158.54
63209	13.5	22.5	$[0_3/90/45/\text{-}45]_s$	32.09	29.54	36.26	-11.5/-18.5	243.9	194.47
63209	9	9	ISOTROPIC	21.4	21.21	22.68	-5.6/-6.4	370.7	258.47

Table A.4: Deflection and stress of front tapered wing T-foil

A.4.3 Validation of U-foil

No spars, 45.000kg displacement, single aft U-foil, root chord 989.76mm

NACA	t_{skin}	t_{web}	lay-up	δ_{NX}	$\delta_{NX,LE}$	δ_{ML}	$\Delta\%$	σ_{ML} [MPa]	σ_{NX} [MPa]
63218	22.5	27	$[0/90/45/\text{-}45]_{2s}$	7.47 20.83	5.18 18.9	4.3 21.52	73.7/20.5 -3.2/-12.1	259.1	124.13 159.31
63209	18	31.5	$[0/45/\text{-}45]_{2s}$	27.95 88.19	19.26 79.04	21.4 107.1	30.6/-10 -17.7/-26.2	654.4	261.03 455.09
63212	27	36	$[45/\text{-}45]_{2s}$	22.18 140.17	18.52 132.41	45.09 225.5	-50.8/-58.9 -37.8/-41.3	159.8	131.54 382.96
			$[0/90]_s$						
63218	18	22.5	$[0/90]_{3s}$	31.23 50.96	19.85 37.02	3.52 17.63	787.2/463.9 189.1/109.9	217.5	381.41 150.21
63209	9	22.5	$[0_6]_s$	325.9 479.75	109.16 219.7	13.45 67.26	2323.1/708.6 613.2/226.7	445.1	1239.33 1018.48
63218	13.5	18	$[0_2/90/45/\text{-}45]_s$	17.71 35.54	7.18 25.94	4.71 23.55	276/52.4 50.9/10.1	280.1	211.69 230.44
63212	27	36	$[0_3/90/45/\text{-}45]_s$	11.66 29.00	8.39 25.25	6.22 31.11	87.5/34.9 -6.7/-18.9	265.1	154.02 100.71
63209	9	9	ISOTROPIC	13.86 40.96	10.29 36.64	7.92 39.63	75/29.9 3.4/-7.5	315.4	325.05 719.53

Table A.5: Deflection and stress of aft U-foil, excluding spars

Including spars, 45.000kg displacement, single aft U-foil, root chord 989.76mm

NACA	t_{skin}	t_{web}	lay-up	δ_{NX}	$\delta_{NX,LE}$	δ_{ML}	$\Delta\%$	σ_{ML} [MPa]	σ_{NX} [MPa]
63218	22.5	27	$[0/90/45/\text{-}45]_{2s}$	4.17 16.92	3.47 16.18	4.3 21.52	-3.1/-19.3 -21.4/-24.8	259.1	414.51 559.35
63209	18	31.5	$[0/45/\text{-}45]_{2s}$	15.20 72.7	13.93 66.19	21.4 107.1	-28.9/-34.9 -32.1/-38.2	654.4	223.49 316.85
			$[0/90]_{\text{-}}$						
63218	18	22.5	$[0/90]_{3s}$	6.76 18.97	4.59 16.114	3.52 17.63	92.1/30.4 7.6/-8.6	217.5	570.12 674.18
63209	9	22.5	$[0_6]_s$	39.39 93.62	22.98 73.95	13.45 67.26	192.9/70.9 39.2/9.9	445.1	574.78 436.86
63218	13.5	18	$[0_2/90/45/\text{-}45]_s$	5.83 21.46	4.37 20.34	4.71 23.55	23.8/-7.2 -8.8/-13.6	280.1	515.77 230.44
63212	27	36	$[0_3/90/45/\text{-}45]_s$	2.73 9.54	2.05 8.74	6.22 31.11	-56.1/-67.1 -69.3/-71.9	265.1	365.73 530.12
63209	9	9	ISOTROPIC	7.76 32.97	6.89 30.22	7.92 39.63	-2.1/-13 -16.8/-23.7	315.4	278.41 256.5

Table A.6: Deflection and stress of aft U-foil, including spars

A.5 Case study input parameters

Inputs		
Parameter	Catamaran	Monohull
Displacement [kg]	175000	45000
Distribution front-aft [%]	40-60	
Number of front foils	2 T-foils	1 T-foil
Number of aft foils	1 W-foil	1 U-foil
Strut length [m]	3	2
Size flap foil [%/chord]	10	20
Size rudder strut [%/chord]	20	
Aspect Ratio	3.5	2.5
Taper Ratio	3	
Width torsion box [%/chord]	40	
Position torsion box [%/chord from LE]	20	
Starting NACA foil	63209	
Starting NACA strut	0015	
Material parameter	Value	
Isotropic: **UNS32750 Super-Duplex** [50]		
E modulus [GPa]	200	
Yield strength [MPa]	530	
Tensile strength [MPa]	730	
Shear modulus[GPa]	77	
Safety factor	1.5	
Fiber: **Torayca M55J HM Carbon** [51]		
Fiber volume fraction	0.5	
Fiber E [GPa]	325	
Fiber G [GPa]	7	
Fiber ν_{12}	0.28	
Matrix: **U20MM General Epoxy** [53]		
Matrix volume fraction	0.5	
Matrix E [GPa]	3.2	
Matrix G [GPa]	1.2	
Matrix ν_{12}	0.36	
Ply mechanics Nastran NX		
E_1 [GPa]	164	
E_2 [GPa]	4.3	
G_{12} [GPa]	1.59	
ν_{12}	0.325	

Table A.7: Properties of and input for conceptual designs

A.6 Results

A.6.1 Monohull concept: Front

Steel UNS S32750

	Strut	Foil
Chord root	0.81128	1.0141
Length	2	1.6899
Skin thickness	0.0162	0.0108
Web thickness	0.0099	0.0108
Max principal	2.8961e+08	3.6552e+08
Max axial stress (buckling)	3.2479e+08	0
Submerged Length	1.0141	1.6899
Drag	1115.9	2592
Total lift of T	82240	2.0133e+05
Foil profile	0.15	0.09
Volume	0.041511	0.018922

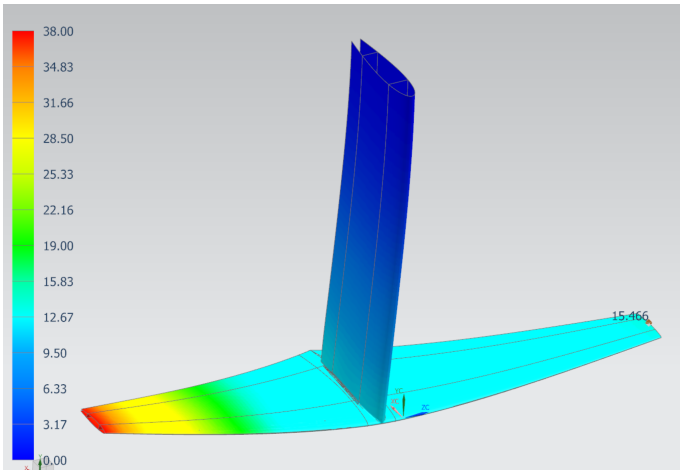

Configuration front

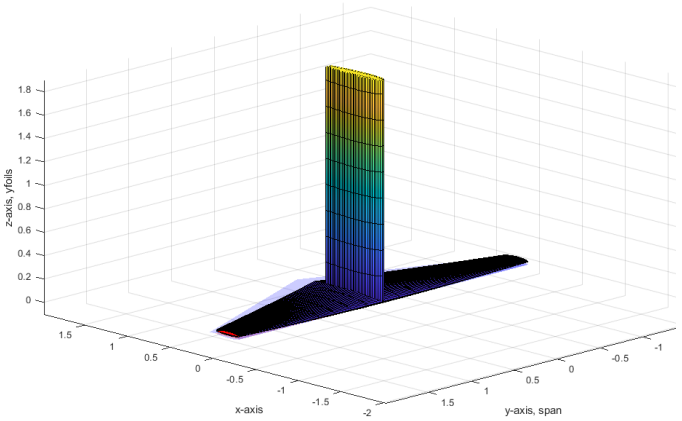

Composites Torayca HM M55J Carbon laminate

	Strut	Foil
Chord root	0.81128	1.0141
Length	2	1.6899
Skin thickness	0.0252	0.0081
Web thickness	0.0243	0.0162
Max principal	NaN	NaN
Max axial stress (buckling)	2.5123e+08	0
Submerged Length	1.0141	1.6899
Drag	1115.9	2592
Total lift of T	82240	2.0133e+05
Foil profile	0.15	0.09
Volume	0.064348	0.014422

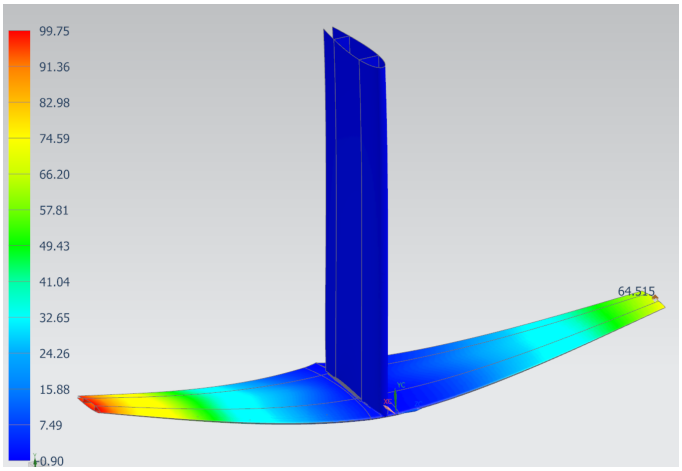

Configuration front

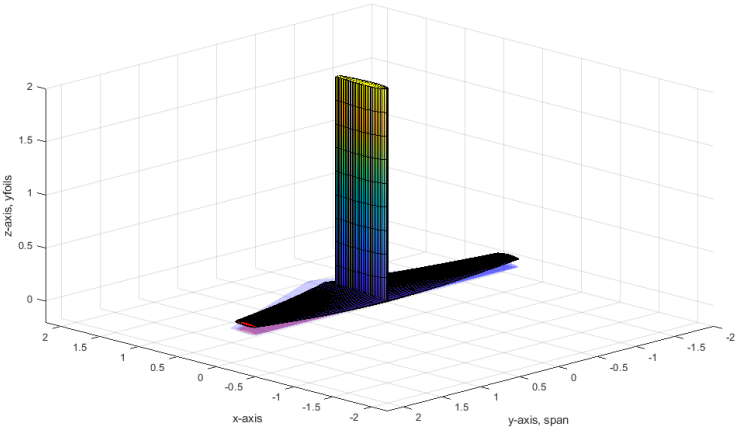

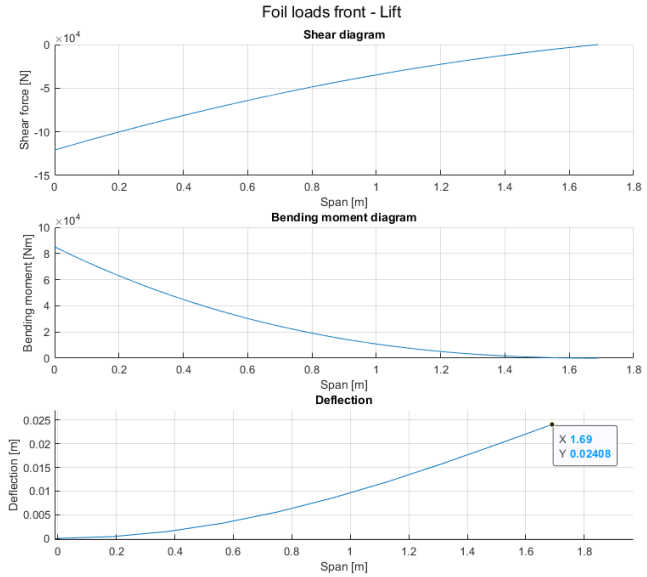
Foil loads front - Lift
Shear diagram
Shear force [N]
Span [m]
Bending moment diagram
Bending moment [Nm]
Span [m]
Deflection
Deflection [m]
X 1.69
Y 0.02408
Span [m]

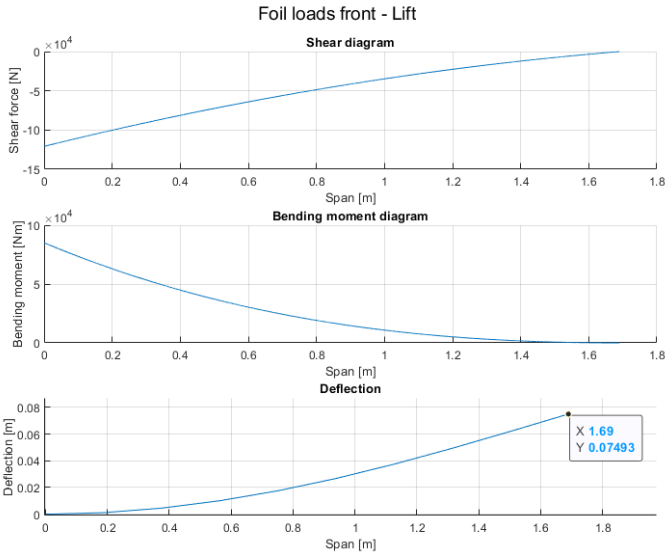
Foil loads front - Lift
Shear diagram
Shear force [N]
Span [m]
Bending moment diagram
Bending moment [Nm]
Span [m]
Deflection
Deflection [m]
X 1.69
Y 0.07493
Span [m]

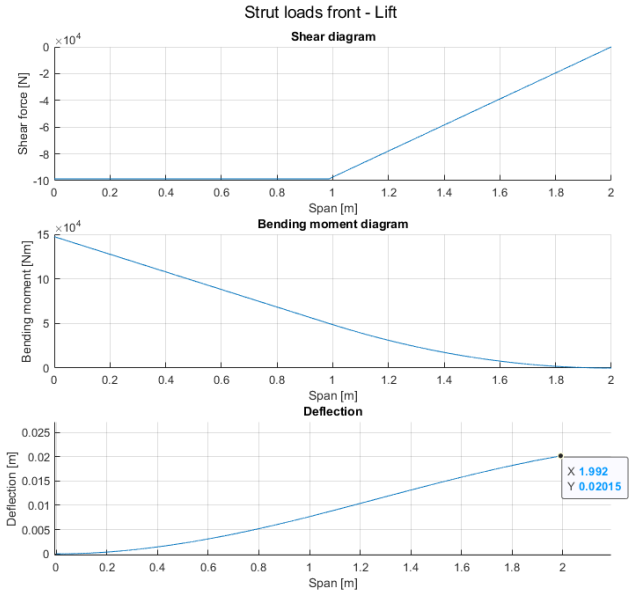
Strut loads front - Lift
Shear diagram
Shear force [N]
Span [m]
Bending moment diagram
Bending moment [Nm]
Span [m]
Deflection
Deflection [m]
X 1.992
Y 0.02015
Span [m]

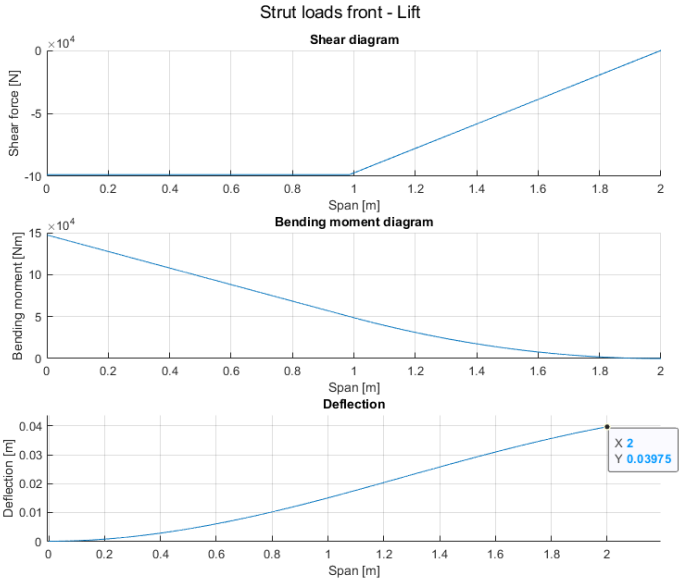
Strut loads front - Lift
Shear diagram
Shear force [N]
Span [m]
Bending moment diagram
Bending moment [Nm]
Span [m]
Deflection
Deflection [m]
X 2
Y 0.03975
Span [m]

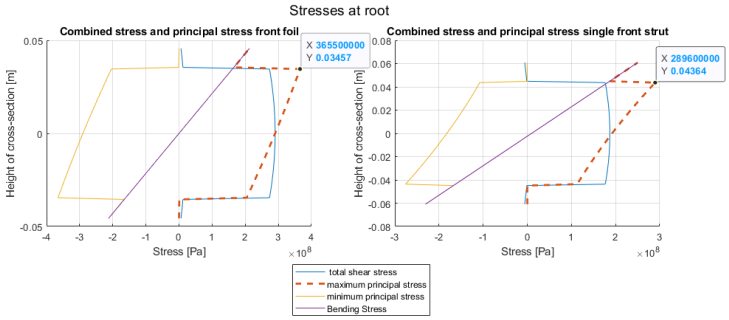
Stresses at root
Combined stress and principal stress front foil
X 365500000
Y 0.03457
Height of cross-section [m]
Stress [Pa]
Combined stress and principal stress single front strut
X 289600000
Y 0.04364
Height of cross-section [m]
Stress [Pa]
total shear stress
maximum principal stress
minimum principal stress
Bending Stress

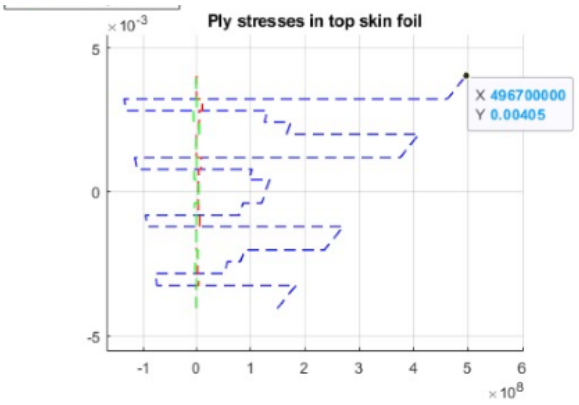
Ply stresses in top skin foil
X 496700000
Y 0.00405

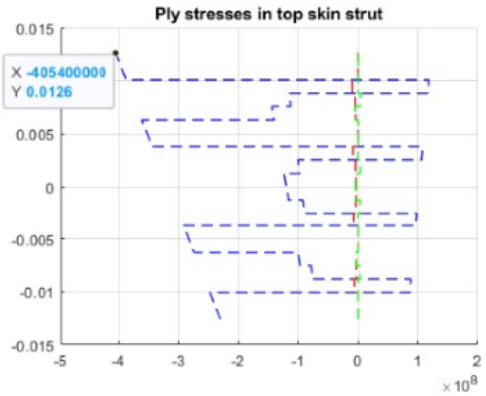
Ply stresses in top skin strut
X -405400000
Y 0.0126

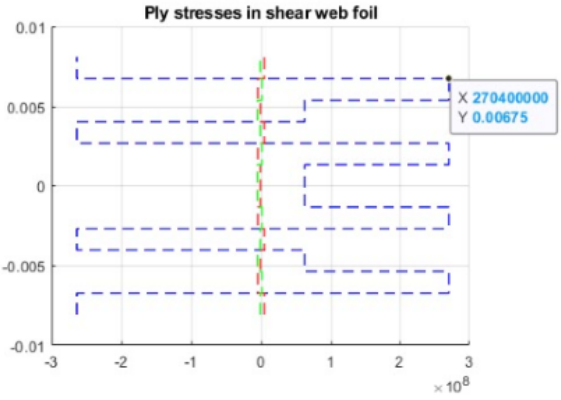
Ply stresses in shear web foil
X 270400000
Y 0.00675

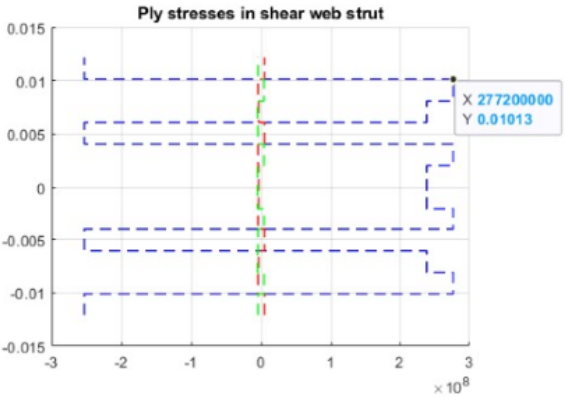
Ply stresses in shear web strut
X 277200000
Y 0.01013

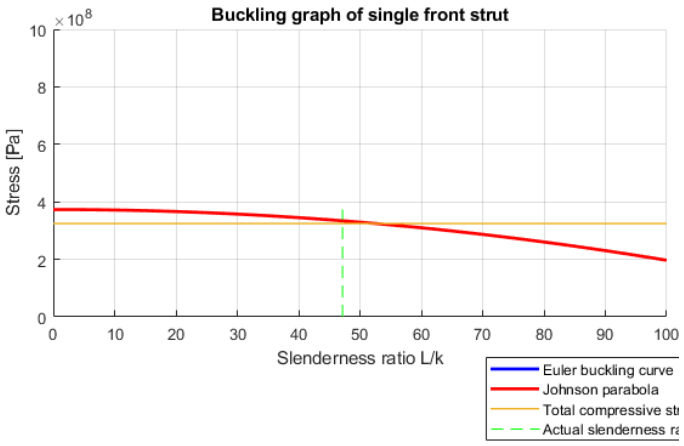

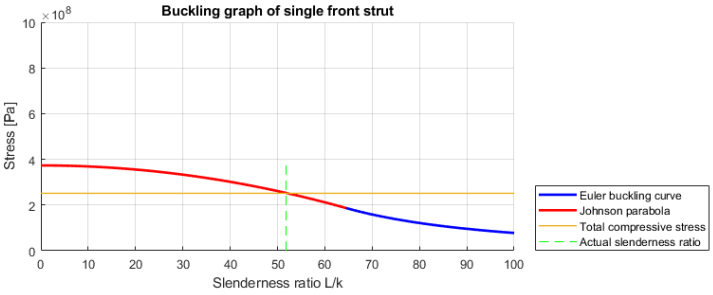

Table A.8: Comparison between results final concept for front foil, metal and composite

A.6.2 Monohull concept: Rear

Steel UNS S32750

	Strut	Foil
Chord root	0.98976	0.98976
Length	2	3.4632
Skin thickness	0.0135	0.0135
Web thickness	0.007875	0.0135
Max principal	3.0987e+08	3.6654e+08
Max axial stress (buckling)	3.4217e+08	0
Submerged Length	0.98976	3.4632
Drag (total)	2657.5	3888.3
Total lift	97924	3.0202e+05
Foil profile	0.15	0.09
Volume (total)	0.084598	0.071889

Composites Torayca HM M55J Carbon laminate

	Strut	Foil
Chord root	0.98976	0.98976
Length	2	3.4632
Skin thickness	0.01575	0.014625
Web thickness	0.018	0.02475
Max principal	NaN	NaN
Max axial stress (buckling)	3.0242e+08	0
Submerged Length	0.98976	3.4632
Drag (total)	2657.5	3586.9
Total lift	97924	3.0835e+05
Foil profile	0.15	0.12
Volume (total)	0.098596	0.07891

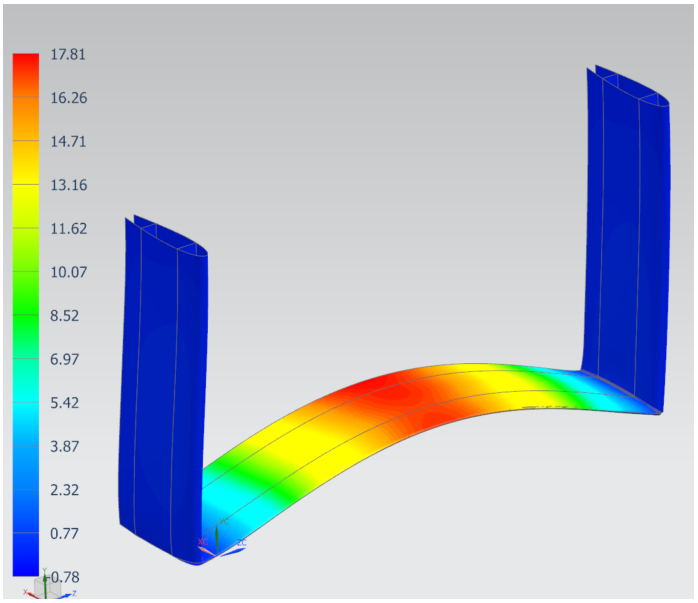

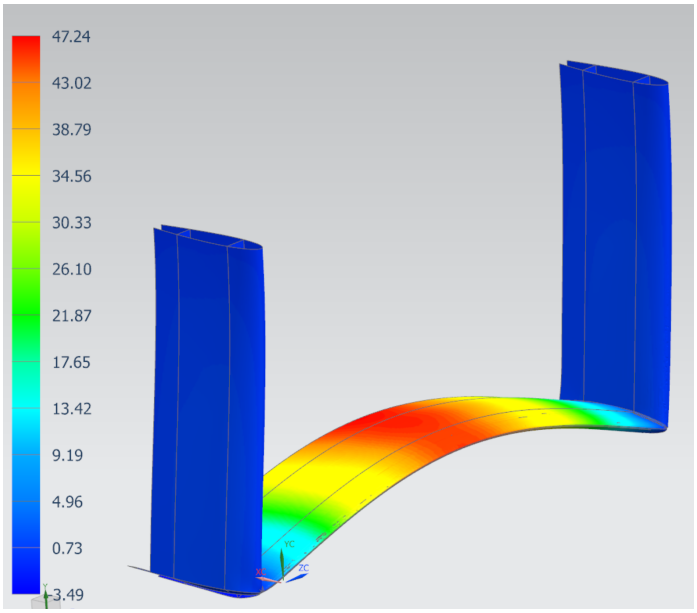

Configuration of AFT foil

Configuration of AFT foil

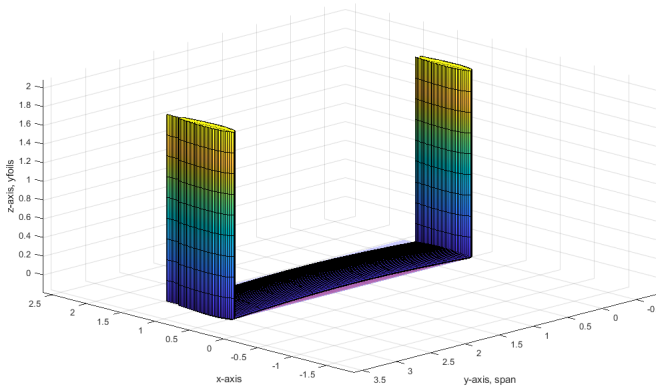

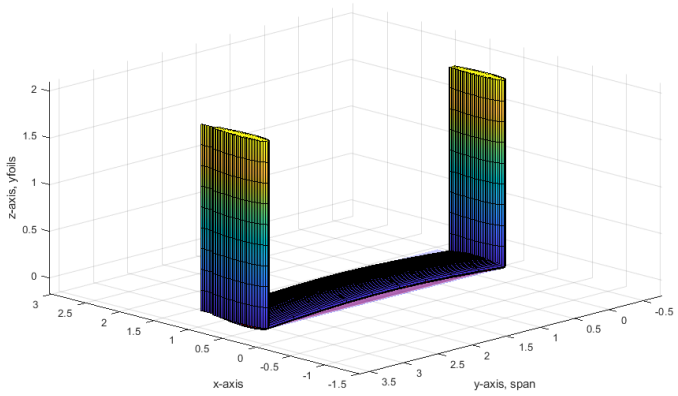

Foil loads rear - Lift

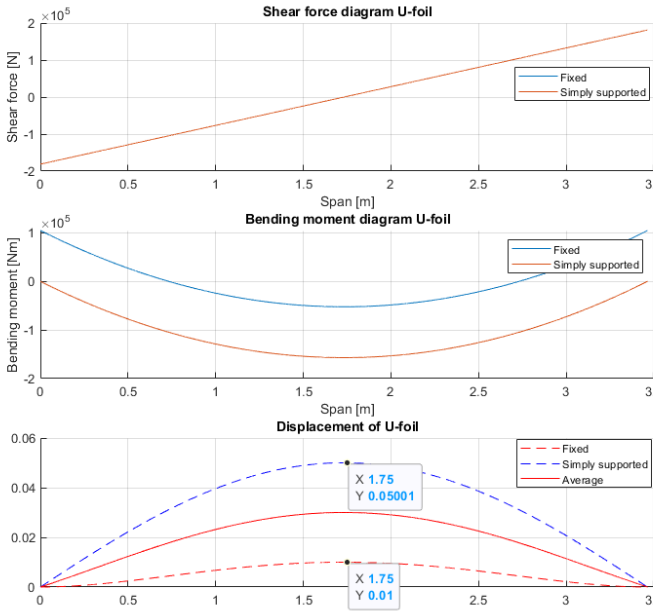

Foil loads rear - Lift

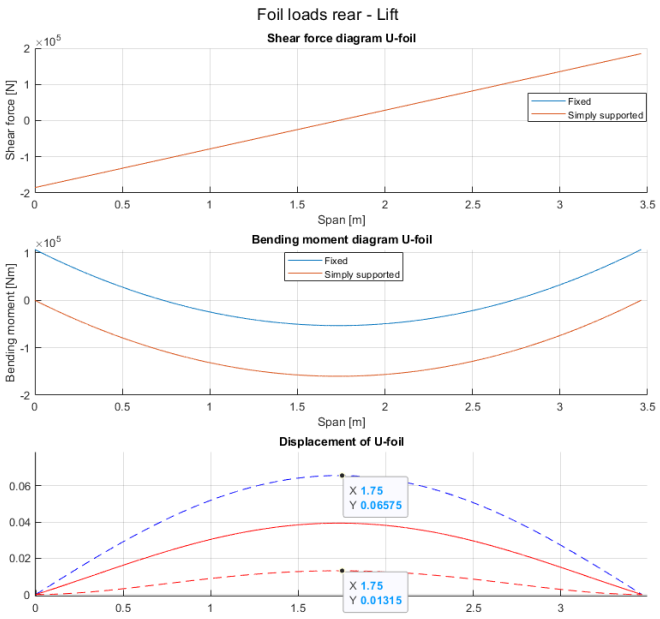

Strut loads rear - lift

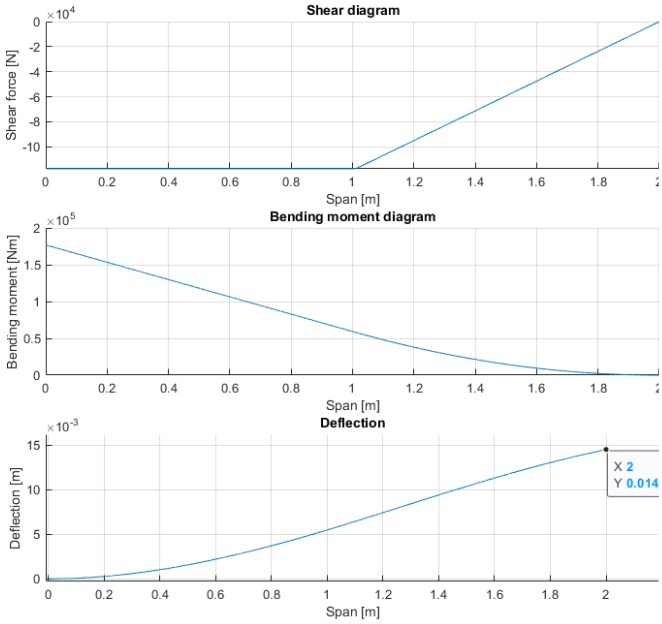

Strut loads rear - lift

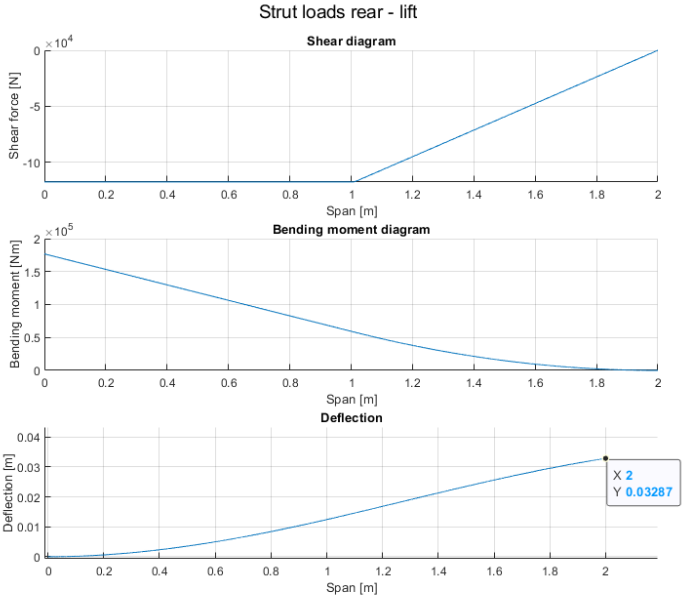

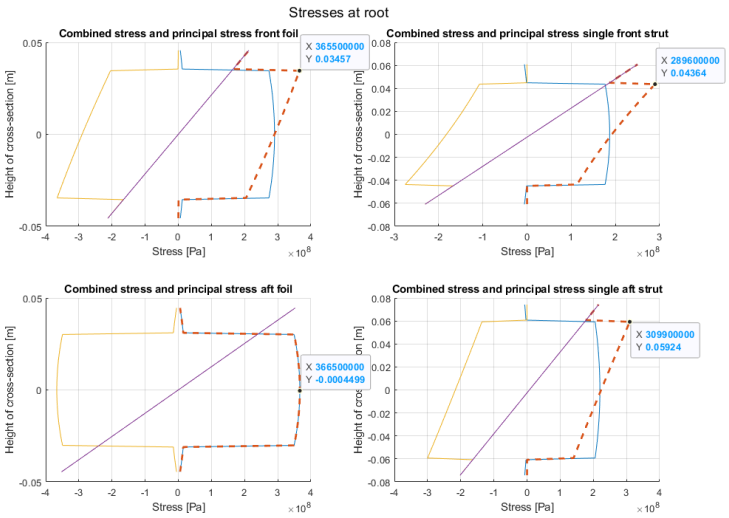
Stresses at root
Combined stress and principal stress front foil
X 365500000
Y 0.03457
Combined stress and principal stress single front strut
X 289600000
Y 0.04364
Combined stress and principal stress aft foil
X 366500000
Y -0.0004499
Combined stress and principal stress single aft strut
X 309900000
Y 0.05924
Height of cross-section [m]
Stress [Pa]


Ply stresses in top skin foil
X 524800000
Y 0.007312


Ply stresses in top skin strut
X -412400000
Y 0.007875

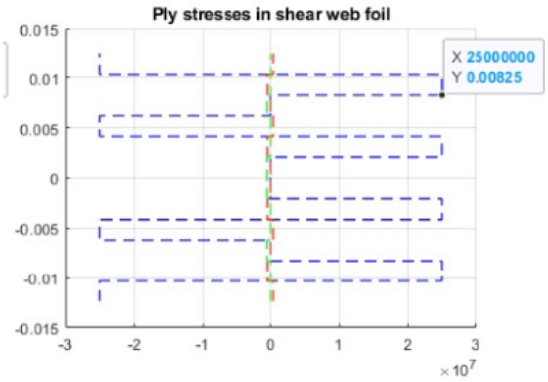
Ply stresses in shear web foil
X 25000000
Y 0.00825

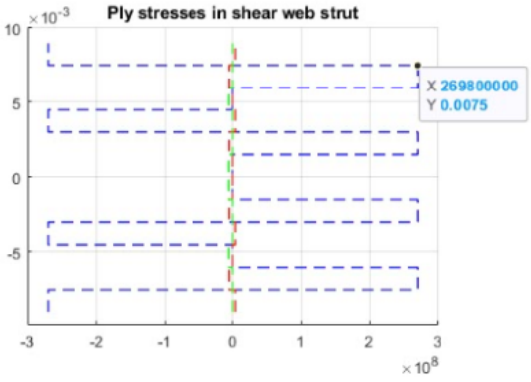
Ply stresses in shear web strut
X 269800000
Y 0.0075

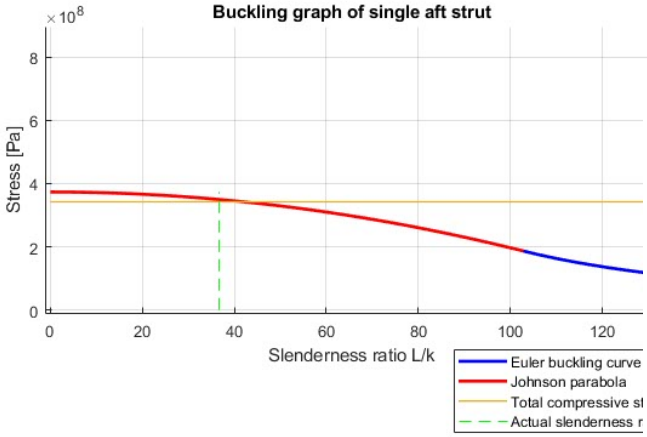

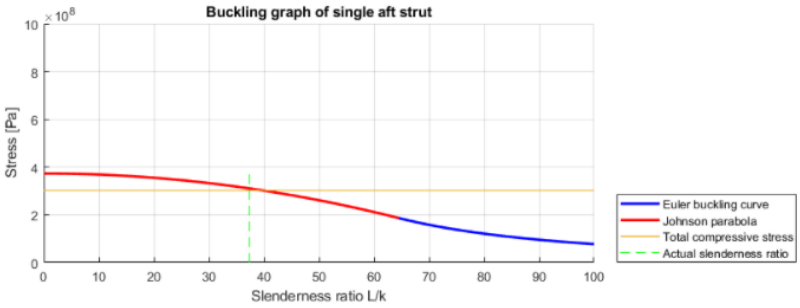

Table A.9: Comparison between results final concept for rear U-foil, metal and CFRP

A.6.3 Catamaran concept: Rear

Steel UNS S32750

	Strut	Foil
Chord root	1.9516	1.9516
Length	3	3.4151
Skin thickness	0.0315	0.0105
Web thickness	0.0315	0.0105
Max principal	3.7246e+08	3.5065e+08
Max axial stress (buckling)	1.449e+08	0
Submerged Length	1.9516	3.4151
Drag (total)	15499	15121
Total lift	3.8073e+05	1.1745e+06
Foil profile	0.15	0.09
Volume (total)	0.9877	0.24343

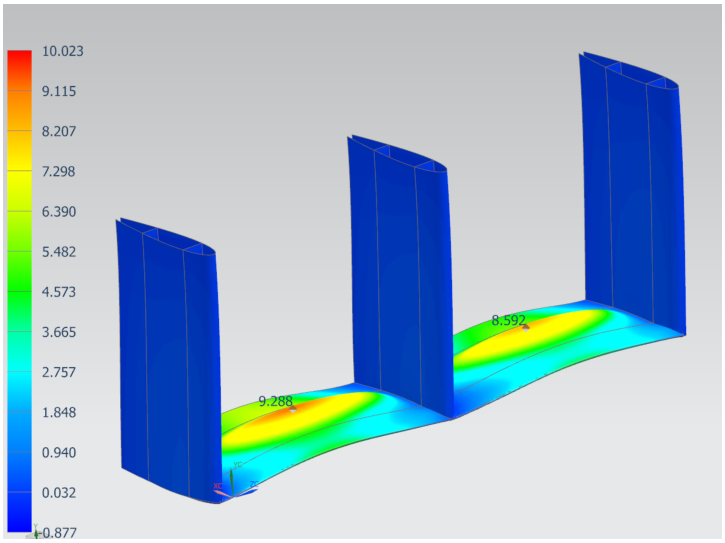

Composites Torayca HM M55J Carbon laminate

	Strut	Foil
Chord root	1.4637	1.9516
Length	3	3.4151
Skin thickness	0.021	0.0105
Web thickness	0.028	0.021
Max principal	NaN	NaN
Max axial stress (buckling)	2.8419e+08	0
Submerged Length	1.9516	3.4151
Drag (total)	11624	15121
Total lift	2.8555e+05	1.1745e+06
Foil profile	0.15	0.09
Volume (total)	0.49418	0.24343

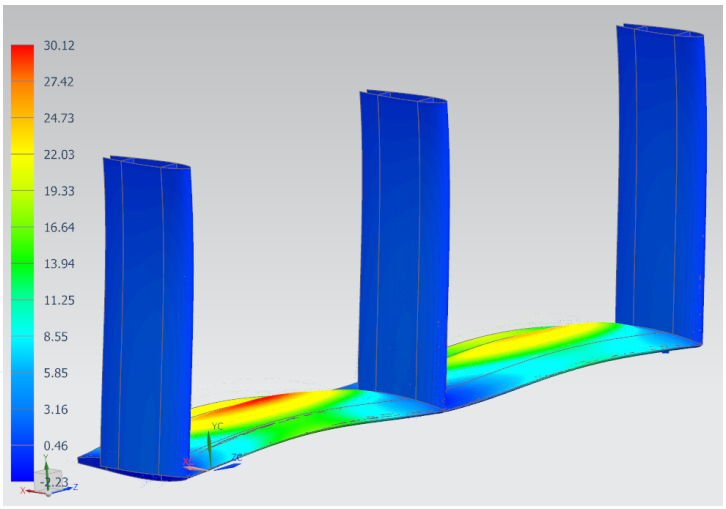

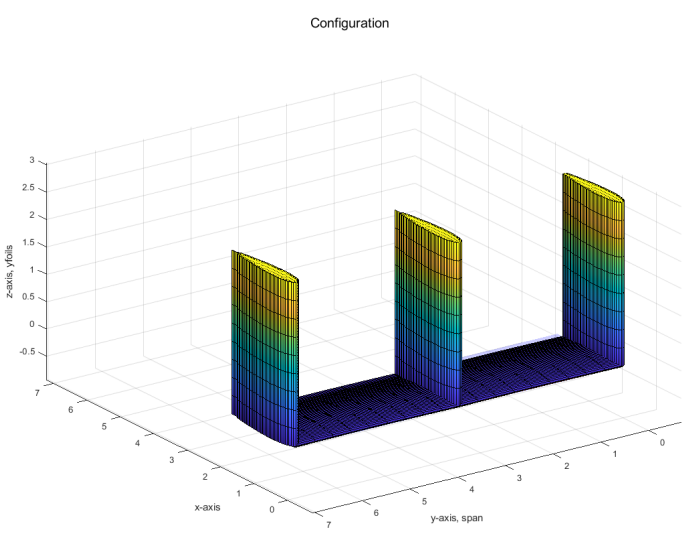

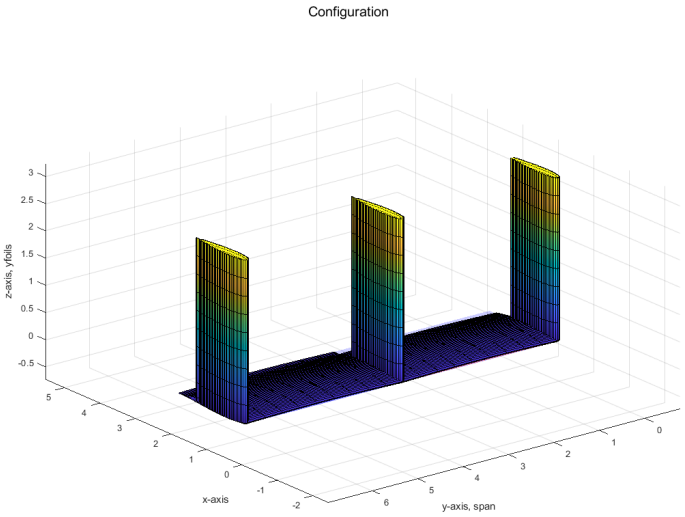

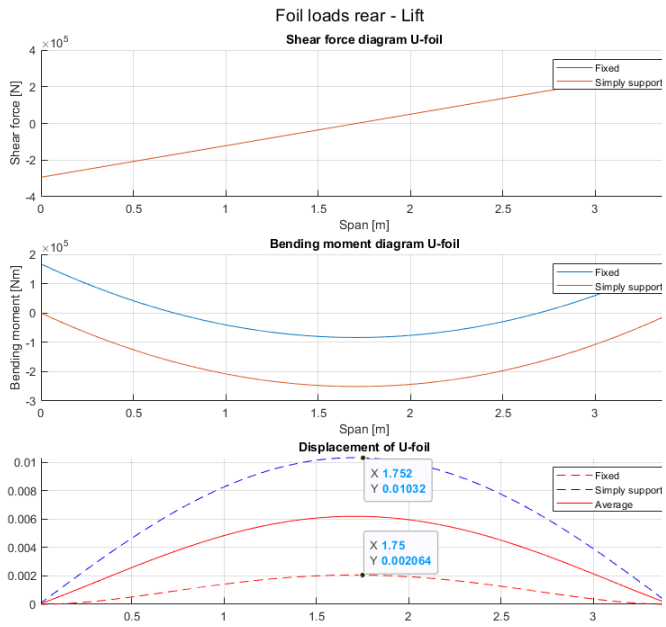

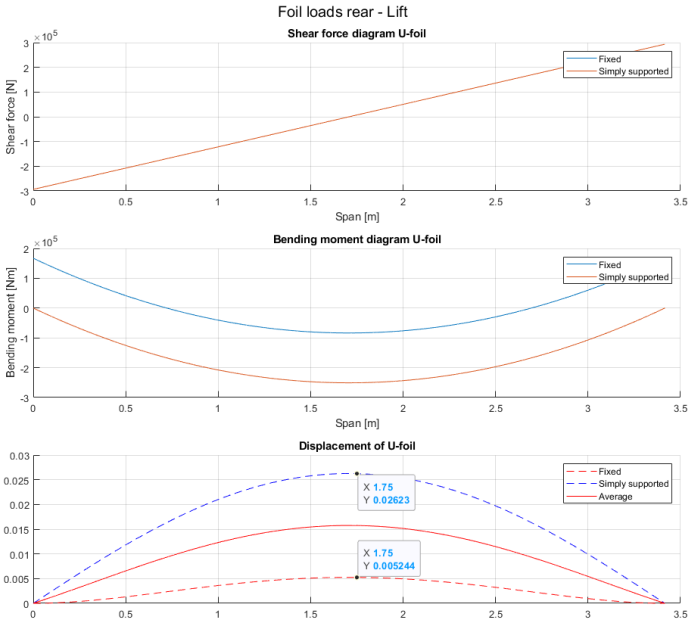

Table A.10: Comparison between results final concept for rear W-foil on Catamaran, metal and CFRP

A.7 Deformation due to lack of boundary condition

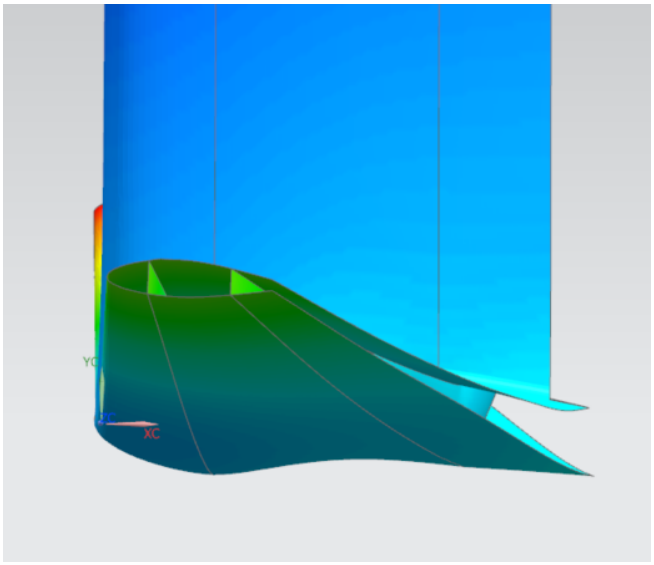

(a) T-foil without internal transverse ribs at root: large distortion, lower overall stiffness

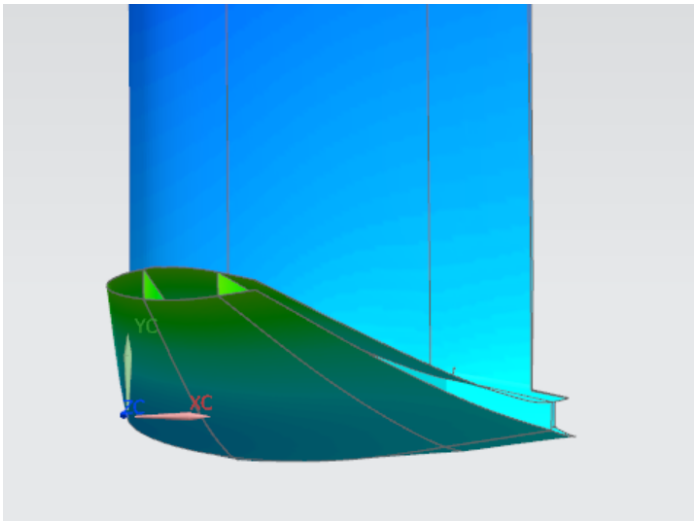

(b) Addition of internal ribs at root, reduced distortion and increased stiffness

Figure A.6: Effect of internal ribs at root on distortion, sideview

A.8 Interface of tool

Shown below is the graphic user interface (GUI) of the developed tool, showing the mandatory input fields to design the hydrofoil and strut(s).

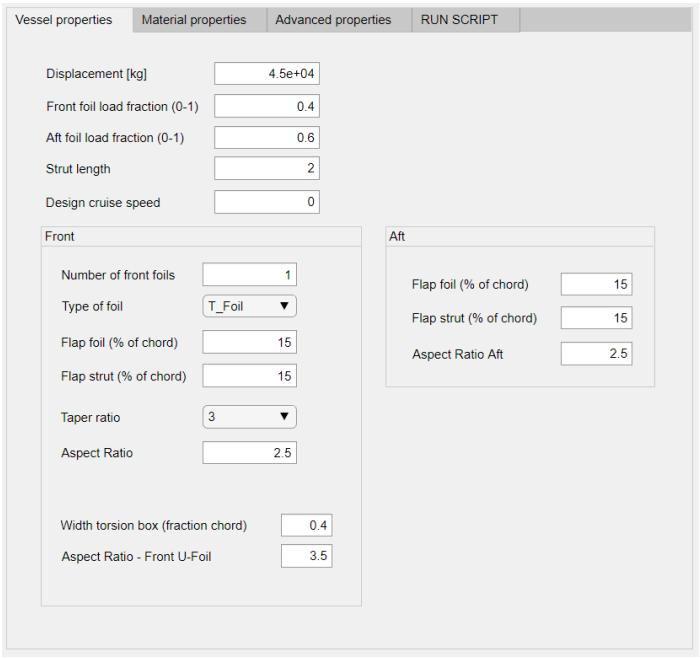

(a) Vessel input variables

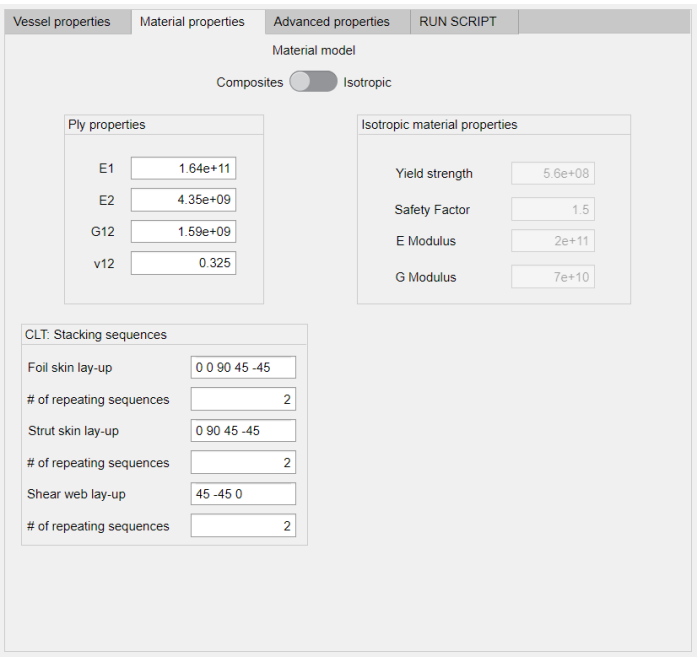

(b) Material input variables

Figure A.7: Tool GUI input screens